UNIVERSIDADE ESTADUAL DE CAMPINAS

INSTITUTO DE FÍSICA GLEB WATAGHIN

GIÁCOMO BIZINOTO FERREIRA BOSCO

Photoluminescence of Tb^{3+} in a-Si_3N_4:H prepared by reactive RF-Sputtering and ECR PECVD

Fotoluminescência de Tb^{3+} em a-Si_3N_4:H preparado por RF-Sputtering reativo e ECR PECVD

CAMPINAS

2017

GIÁCOMO BIZINOTO FERREIRA BOSCO

Photoluminescence of Tb^{3+} in a-Si_3N_4:H prepared by reactive RF-Sputtering and ECR PECVD

Fotoluminescência de Tb^{3+} em a-Si_3N_4:H preparado por RF-Sputtering reativo e ECR PECVD

Tese apresentada ao Instituto de Física "Gleb Wataghin" da Universidade Estadual de Campinas como parte das atividades para obtenção do título de Doutor em Ciências.

Thesis presented to the "*Gleb Wataghin*" Physics Institute of the University of Campinas in partial fulfillment of the requirements for the degree of Doctor of Sciences.

Supervisor: Prof. Dr. Leandro Russovski Tessler

ESTE EXEMPLAR CORRESPONDE À VERSÃO FINAL DA TESE DEFENDIDA PELO ALUNO GIÁCOMO BIZINOTO FERREIRA BOSCO E ORIENTADA PELO PROF. DR. LEANDRO RUSSOVSKI TESSLER.

CAMPINAS

2017

Agência(s) de fomento e nº(s) de processo(s): CNPq, 142174/2012-2; CAPES, 010308/2014-08
ORCID: http://orcid.org/0000-0002-5154-8610

Ficha catalográfica
Universidade Estadual de Campinas
Biblioteca do Instituto de Física Gleb Wataghin
Lucimeire de Oliveira Silva da Rocha - CRB 8/9174

Bosco, Giácomo Bizinoto Ferreira, 1987-
B651p Photoluminescence of Tb3+ in a-Si3N4:H prepared by reactive RF-Sputtering and ECR PECVD / Giácomo Bizinoto Ferreira Bosco. – Campinas, SP : [s.n.], 2017.

Orientador: Leandro Russovski Tessler.
Tese (doutorado) – Universidade Estadual de Campinas, Instituto de Física Gleb Wataghin.

1. Fotoluminescência. 2. Térbio. 3. Nitreto de silício. 4. Semicondutores amorfos. I. Tessler, Leandro Russovski,1961-. II. Universidade Estadual de Campinas. Instituto de Física Gleb Wataghin. III. Título.

Informações para Biblioteca Digital

Título em outro idioma: Fotoluminescência de Tb3+ em a-Si3N4:H preparado por RFSputtering reativo e ECR PECVD **Palavras-chave em inglês:**
Photoluminescence
Terbium
Silicon nitride
Amorphous semiconductors
Área de concentração: Física
Titulação: Doutor em Ciências
Banca examinadora:
Leandro Russovski Tessler [Orientador]
Gustavo Silva Wiederhecker
Francisco das Chagas Marques
Peter Mascher
Euclydes Marega Júnior
Data de defesa: 07-04-2017
Programa de Pós-Graduação: Física

MEMBROS DA COMISSÃO JULGADORA DA TESE DE DOUTORADO DE **GIÁCOMO BIZINOTO FERREIRA BOSCO – RA: 061109** APRESENTADA E APROVADA AO INSTITUTO DE FÍSICA “GLEB WATAGHIN”, DA UNIVERSIDADE ESTADUAL DE CAMPINAS, EM 07/04/2017.

COMISSÃO JULGADORA:

- Prof. Dr. Leandro Russovski Tessler – (Orientador) – DFA/IFGW/UNICAMP
- Prof. Dr. Gustavo Silva Wiederhecker – DFA/IFGW/UNICAMP
- Prof. Dr. Francisco das Chagas Marques – DFA/IFGW/UNICAMP
- Prof. Dr. Peter Mascher – McMaster University
- Prof. Dr. Euclydes Marega Júnior – IFSC/USP

A Ata de Defesa, assinada pelos membros da Comissão Examinadora, consta no processo de vida acadêmica do aluno.

CAMPINAS
2017

Dedico este trabalho a meus pais, Geraldo Bosco e Maria Aparecida Ferreira, minha irmã, Gisele Bizinoto e à minha querida Gabriela Ricci.

Acknowledgments

There would be no possible way of presenting this thesis without the effort of many people who participated in these intense, rich, and fruitful years necessary for the conclusion of this research project. People from very different backgrounds who directly and indirectly contributed with this research; helping in the sample fabrication and characterization analysis processes or by giving very important feedback and discussions or even with the sometimes-necessary emotional support.

First, I would like to thank my mother, Maria Aparecida Ferreira, my father, Geraldo Bosco, and my sister, Gisele Bizinoto. Thank you for all your cheering, guidance, and support over the course of my life. Gabriela Ricci, my love, you deserve a special thank you for not only your emotional support but with all your help, even late at night, with all the presentation previews you had to listen to and comment about.

I would like to thank my supervisor, Leandro R. Tessler, for all the opportunities offered and for all these years of partnership and guidance.

In Brazil, I would like to thank past and present members of the *Laboratório de Pesquisas Fotovoltaicas* from *Departamento de Física Aplicada*, my colleagues: Gustavo Viana, Rafael Merlo, Sílvia Cucatti, Diego Scoca, Diego Oliveira, André Garcia Primo, Vinícius Antunes and Douglas Soares. Thank you for always being present for very valuable discussions and help throughout all these years in Campinas. I would like to thank Carlos Lenz César for accompanying this work since the very beginning and all the valuable feedback and important commentaries given.

I am immensely grateful to Peter Mascher, for opening the doors to new possibilities and opportunities at the Centre for Emerging Device Technologies (CEDT) and at the Department of Engineering Physics at McMaster University, in Canada. I would also like to thank past and present members of Peter Mascher's research group with whom I shared a very exciting year of work: Zahra Khatami, Austin Brown, Pankhul Dingra, Patrick Wilson, Dan Frisina, and Bomi Lee. A special thank you goes to Zahra, who intensily participated in this research and helped me a lot in my very first days of research in Canada. I am also very grateful to the assistance and training provided by Jacek Wojcik in the growth and characterization of the thin films grown in CEDT. Not only that, in fact I am also very grateful to all the adventures and discoveries made possible by you, making this year a very special one.

Thanks to Jack Hendriks and Lyudmilla Goncharova from the Tandetron Laboratory at Western University; Tiago Fiorini and Marcos Rodrigues from the *Laboratório de Materiais e Feixes Iônicos* (LAMFI) at University of São Paulo for their help with Rutherford backscattering spectrometry (RBS) experiments conducted respectively at Canada and Brazil. Kevin Boyd and Andrew Knights with their support in the Fourier transform infrared spectroscopy (FTIR) measurements. To the *Laboratório Nacional de Luz Síncrotron* (LNLS) for the technical support in the X-ray absorption spectroscopy (XAS) measurements. I am also very grateful to Gianluigi Botton and Brian Langelier from the Canadian Centre for Electron Microscopy (CCEM) at McMaster University for offering the possibility of characterization with Atom Probe Tomography (APT).

Finally, I would like to thank the financial support given by *Conselho Nacional de Desenvolvimento Científico e Tecnológico* (CNPq) and *Coordenação de Aperfeiçoamento de Pessoal de Nível Superior* (CAPES); Natural Sciences and Engineering Research Council of Canada (NSERC).

Resumo

Este trabalho fornece caracterização ótica e estrutural de filmes finos compostos por nitreto de silício amorfo hidrogenado dopado com térbio (a-SiN_x:H<Tb>) – crescidos por deposição química a vapor assistida por plasma gerado através de ressonância ciclotrônica de elétrons (ECR PECVD) e por pulverização catódica reativa em radiofrequência (*reactive* RF-*Sputtering*) – com o propósito de avançar a investigação em fabricação de novos materiais e dos mecanismos da emissão de luz de íons de Tb quando diluídos em materiais baseados em silício. A fotoluminescência (PL) atribuída aos filmes de a-SiN_x:H<Tb> foi investigada em termos das condições de deposição e correlacionadas com suas propriedades estruturais e de recozimento pós-deposição. Entre as propriedades caracterizadas estão: estequiometria, taxa de deposição, índice de refração, coeficiente de extinção, *bandgap* ótico E_{04}, concentração de térbio e vizinhança química presente ao redor de íons Tb^{3+}. Concentrações de Tb da ordem de 1.8 at.% ou $1.4\times10^{21}\ at/cm^3$ foram obtidas em amostras crescidas por *Sputtering* enquanto que concentrações de 14.0 at.%, ou da ordem $10^{22}\ at/cm^3$, puderam ser obtidas em amostras crescidas por ECR PECVD. Em *Sputtering*, a incorporação de Tb varia linearmente com a área recoberta por pastilhas de Tb_4O_7 em pó, enquanto que em PECVD, a incorporação de Tb é inversamente proporcional e pode ser ajustada sensivelmente pelo fluxo de gás SiH_4.

Forte emissão de luz, atribuída às transições eletrônicas em Tb^{3+} (PL do Tb), foi obtida em filmes não-recozidos que possuíam *bandgap* estequiométrico ($E_{04} = 4.7 \pm 0.4$ eV and $x = 1.5 \pm 0.2$). Espectros de PL do Tb não mostraram mudanças significativas no formato e na posição dos picos de emissão devido a alterações na temperatura de recozimento, nas condições de deposição ou entre amostras crescidas por diferentes técnicas de deposição. Entretanto, esses parâmetros influenciaram fortemente a intensidade da PL do Tb.

Estudos da estrutura fina de absorção de raios-X (XAFS) em filmes crescidos por *sputtering* mostraram a estabilidade da vizinhança química ao redor dos íons Tb^{3+} mesmo em altas temperaturas (1100ºC). Investigações por sonda atômica tomográfica (APT) não encontraram formação de nanoclusters envolvendo ou não Tb, mesmo após recozimentos em altas temperaturas. Isso sugere que a excitação de Tb^{3+} deve ocorrer

através da própria matriz hospedeira amorfa e não por mudanças no campo cristalino e, portanto, na força de oscilador das transições eletrônicas do Tb^{3+}.

Caracterização da densidade de ligações Si-H por espectroscopia infravermelha a transformada de Fourier (FTIR) em filmes recozidos em diferentes temperaturas foi relacionada com a intensidade da PL do Tb. Ela mostra que um decréscimo na densidade das ligações Si-H, que está relacionada a um aumento na concentração de ligações pendentes de Si (Si-dbs), resulta em filmes com maior intensidade na PL do Tb. Portanto, isso sugere que a excitação de Tb^{3+} parece acontecer através de transições envolvendo Si-dbs e estados estendidos, o que é consistente com o modelo de excitação Auger por defeitos (DRAE).

Abstract

This work offers optical and structural characterization of terbium (Tb) doped hydrogenated amorphous silicon nitride thin films (a-SiN_x:H<Tb>) grown by electron cyclotron resonance plasma-enhanced chemical vapor deposition (ECR PECVD) and reactive RF-Sputtering with the purpose of advancing the investigation in fabrication of novel materials and the mechanisms of light emission of Tb ions when embedded in Si-based materials. Photoluminescence (PL) of a-SiN_x:H<Tb> films were investigated and correlated with the deposition conditions, structural properties, and post-deposition thermal treatments (isochronal annealing under flow of N_2). Among the characterized properties are: film stoichiometry, deposition rate, refractive index, extinction coefficient, optical bandgap, terbium concentration, and the chemical neighborhood around Tb ions. Tb concentrations of about 1.8 at.% or $1.4\times10^{21}\ at/cm^3$ have been achieved in Sputtering system while concentrations of 14.0 at.%, or about $10^{22}\ at/cm^3$, could be achieved in ECR PECVD samples. In Sputtering, Tb incorporation varies linearly with the covered area of the Si target by Tb_4O_7 powder pellets, while in PECVD, Tb incorporation is inversely proportional to and can be sensitively adjusted through SiH_4 gas flow.

Bright PL attributed to Tb^{3+} electronic transitions (Tb PL) were obtained in as-deposited films with stoichiometric bandgaps ($E_{04} = 4.7 \pm 0.4$ eV and $x = 1.5 \pm 0.2$). The Tb PL spectra did not show any significant change in shape and in PL peak positions due to alterations in annealing temperature, deposition conditions or due to the used deposition method. However, these parameters strongly affected Tb PL intensity.

Studies of X-ray absorption fine structure (XAFS) in Sputtering grown films show the stability of the chemical neighborhood around Tb^{3+} under annealing conditions even after thermal treatments at temperatures as high as 1100ºC. Atom probe tomography (APT) investigation also found no formation of nanoclusters of any type (involving Tb ions or not) after high temperature annealing treatments suggesting that Tb^{3+} excitation should come from the amorphous host matrix itself and not by changes in crystal field and thus in oscillator strength of Tb^{3+} electronic transitions.

Fourier transform infrared spectroscopy (FTIR) characterization of Si-H bond density in films treated at different annealing temperatures were correlated with Tb PL

intensity. It shows that a decrease in Si-H bond density, related to increase in Si dangling bonds (Si-dbs) concentration, results in greater Tb PL intensity. Thus, it suggests that excitation of Tb^{3+} happens through transitions involving silicon dangling bonds and extended states, consistent with the defect related Auger excitation model (DRAE).

Table of Contents

1 Introduction

Silicon microelectronics, based on complimentary metal-oxide semiconductor technology (CMOS), has had a fundamental role in the revolution that has taken place in the last decades which is now present in almost every aspect of everyone's life. The constant need for higher data rates is pushing silicon microelectronics to its fundamental limitations imposed by resistive-capacitive delays that come from downscaling and the constant increase in interconnects lengths. To extend the lifetime of the existing silicon architecture, the use of light, instead of electrons, seems to be the solution to further increase data rates while avoiding those limitations. It would be ideal that this solution could also adhere to CMOS fabrication standards. Being silicon the second most abundant element in Earth's crust, this solution could be cost-effective. It also has a good potential for large scale implementation because it could take advantage of the already existing microelectronic fabrication facilities. This is the promise given by what is known as "silicon photonics".

Almost all photonics building blocks for an integrated silicon photonics circuit have been proved experimentally in the last decades: silicon based optical waveguides [1]–[4], tunable optical filters [5]–[9], fast switches [10]–[13], optical modulators [14]–[16], photodetectors [17]–[19], and even the development of first Si-based CMOS photonic chips [20]. The component that is still missing is an efficient, monolithic silicon-based light source which requires convenient pumping mechanisms [21], [22].

In the visible light region, solid-state lighting and displays applications would take great advantage of low cost silicon based light-emitting devices (LEDs). Most optical components are still made from III–V-based compounds such as indium phosphide (InP) or gallium arsenide (GaAs) [23] which can be considered exotic in the sense that they are costly and require fabrication processes of difficult integration with CMOS infrastructure.

One of the fundamental issues for Si light emission is that crystalline bulk Si (c-Si) is an indirect bandgap semiconductor. This implies that phonons always mediate radiative transitions, a very inefficient process. In the so far best-case scenario, the electrical-to-optical conversion in bulk Si systems is as low as 1% [24]. Several strategies and routes have been proposed and explored over the years in the pursuit of overcoming this intrinsic limitation.

Among them are porous silicon [25]–[29], silicon nanowires [30]–[33], silicon quantum dots [34]–[37], and rare earth doping in amorphous silicon based alloys [21], [38]–[43].

Rare earth trivalent ions when embedded in insulating solids have intense and narrow intra-4*f* transitions whose precise energies depend very weakly on the host choice and represent a signature of each element. Some ions, like Er^{3+} and Nd^{3+}, have transitions within the infrared region, while others, such as Ce^{3+}, Eu^{3+}, and Tb^{3+}, have transitions in the visible part of the electromagnetic spectrum.

Er^{3+} is definitely the most studied rare earth element for light emission purposes [21]. Erbium-doped fibre amplifiers (EDFAs) are used for long-haul telecommunications. This is only possible due to the efficient 1.54 μm energy line - within the low loss window of silica fibres. This case of success has driven much attention to Er doped Si based thin films (porous [44]–[48], carbides [49]–[51], nitrides [52]–[54], oxides [55]–[57] etc.) and later paved the way for the investigation of other rare-earths on those same solid hosts for a wide range of different potential applications.

One element of the rare-earth family is Tb^{3+}. It has intense blue and green light emission lines which are widely used in display and lighting applications. Nevertheless, luminescence of Tb within silicon based thin films have received much less attention. A thorough research on the available works on the topic reveals that the first studies date back to late 1990s [45], [58], [59]. Although almost 20 years have passed, no more than 30 works have been published in peer review journals which precisely investigated the luminescence properties of Tb^{3+} ions in silicon based materials. Starting timidly in the first years with an average of one work per year, more interest about the topic slightly increased only after 2002, concurrently with the development of *in-situ* incorporation techniques which allowed higher amounts of lanthanide incorporation and better control of concentration over film depth.

Much of the research on Tb-doping in silicon based alloys have focused mostly on silicon rich silicon oxides [60] and oxynitrides [61] exploring the excitation provided by silicon nanocrystal engineering [62] and the influence of defect passivation on the luminescence [63]. Little attention has been given, though, to nitrogen rich amorphous silicon nitrides ($a\text{-}SiN_x\text{:}H$). As it is well known, $a\text{-}SiN_x\text{:}H$ have large band gaps, ranging from 2.0 to more than 5.0 eV [64]–[66], making it suited for hosting emissions in the visible range, characteristic of terbium ions.

There is still a debate regarding the different excitation mechanisms of Tb^{3+} ions in different Si-based materials. Different routes for Tb^{3+} excitation may occur in silicon based matrices. Some authors presented evidence that the band tails do not participate in excitation [61]. Others claim that silicon nanoclusters [67]–[69] and/or rare earth silicate clusters [60] are involved in the process. This view has been dominant for much of the work on Tb doped silicon based materials. When embedded in a wide band gap amorphous network, clusters can produce energy levels inside the gap which could resonantly transfer energy to one of the higher Tb^{3+} energy levels. Other authors cite an alternative high yield excitation process from the host's extended electronic states to the high energy Tb^{3+} ^7D band [70], [71], a transition associated with the promotion of one 4*f* electron to the 5*d* orbital – see Figure 1 for photoluminescence excitation spectra. Nonetheless, there is very little discussion about the role of deep levels and the silicon dangling bonds (Si-dbs) in the amorphous network itself. In Er doped a-Si:H [72] and Nd doped a-SiN_x:H [40], this is the main pathway for rare earth excitation. In fact, for the specific case of Tb^{3+}, in a-SiN_x, this was cited as a possible path for Tb excitation by Yuan *et al.* [73], who also considered $N_4^+$and N_2^0 defects (Figure 2) as other possible excitation sources. However, these defects are more common in the crystalline phase of Si_3N_4 [74] and are not commomnly reported in amorphous materials.

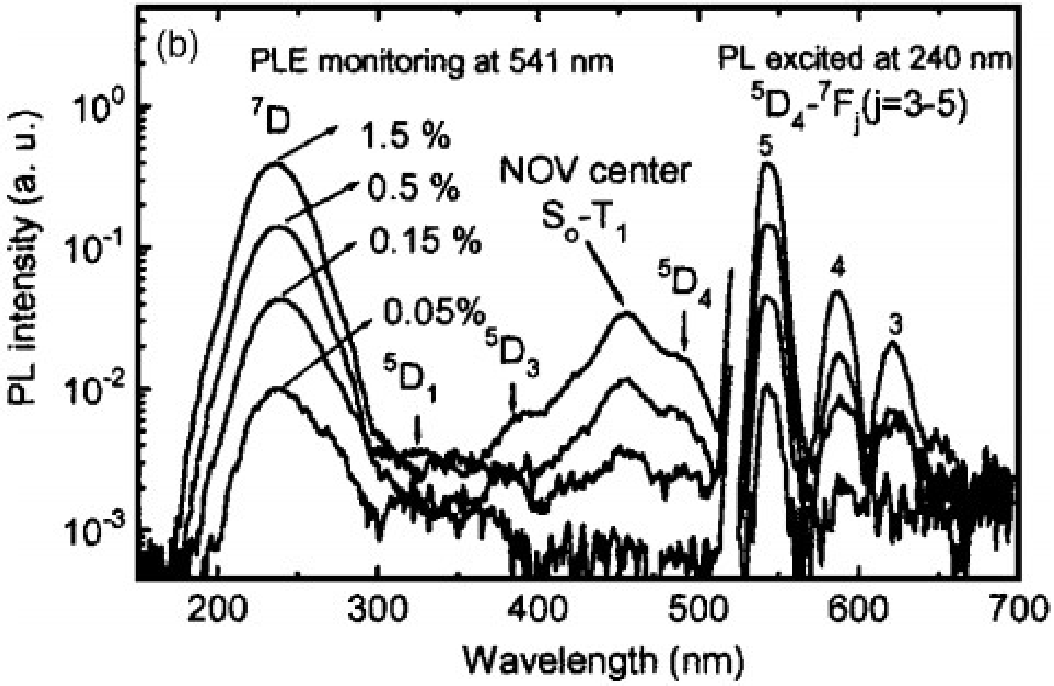

Figure 1: PL and PLE spectra of Tb doped SiO_2 films obtained by Sun *et al.* [75].

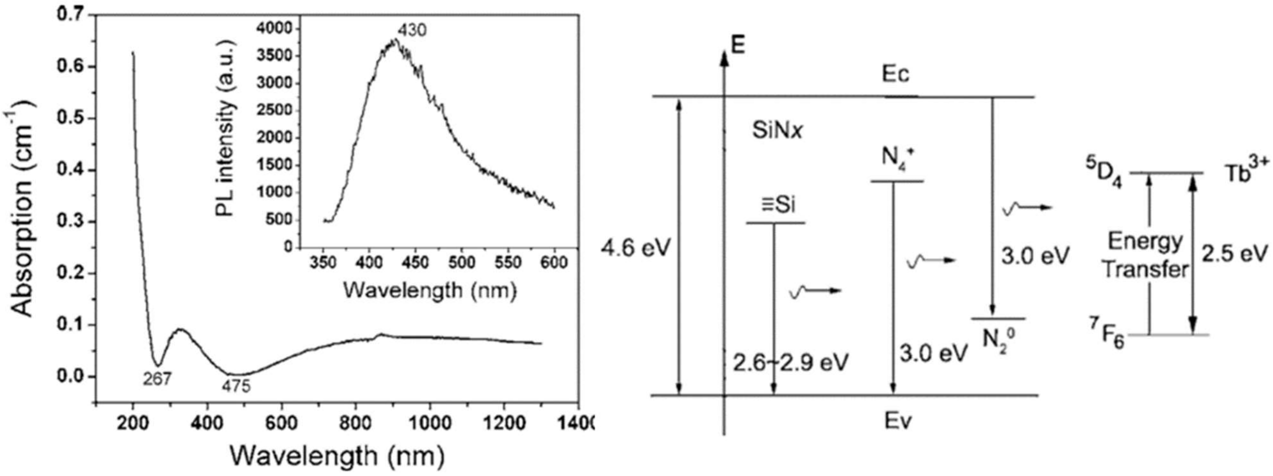

Figure 2: **Left** - Absorption spectrum of undoped nitrogen rich SiN_x. In the inset is its PL spectrum at room temperature; **Right** - Proposed energy transfer process involving both Si and N dangling bonds. After [73].

1.1 Thesis Objective and Methods

This work was conceived to provide further investigation of Tb doped a-SiN_x:H thin-films (or a-SiN_x:H<Tb>) in view of the search for active materials that could make viable silicon-based light-emitting devices in the visible region, with efficiencies comparable to those obtained in III-V semiconductors. To achieve this goal, a clear understanding of the underlying mechanisms responsible for light emission is required. It is expected that the information provided in this thesis can offer helpful information towards the development of new materials, applicable to new efficient devices.

The research presented in this thesis is a somewhat natural continuation of earlier work at *Laboratório de Pesquisas Fotovoltaicas* (LPF) in IFGW/Unicamp, that studied PL properties of other rare-earth elements embedded in SiN_x and SiO_x hosts [38], [40], [76], [77]. Using reactive RF-Sputtering as the film fabrication method, the deposition parameters space was widely explored and the best conditions of film deposition, for maximum PL of Tb^{3+}, and the parameters of thermal treatment were determined. Samples of a-SiN_x:H<Tb> were grown and characterized at McMaster University using plasma enhanced chemical vapor deposition generated by electron cyclotron resonance (ECR PECVD), a very different deposition method. The characterization experiments were conducted at the Centre for Emerging Device Technologies (CEDT) together with the Department of Engineering Physics at McMaster University. With such an amount of data, a direct comparison of film characteristics grown by two different methods could be done.

The approach used for the investigation of the important parameters for Tb^{3+} light emission was through chemical composition characterization, by Rutherford Backscattering Spectrometry (RBS). Along with it, room temperature photoluminescence experiments were conducted and optical constants film thickness determination were obtained by Variable-Angle Spectroscopic Ellipsometry (VASE). As already mentioned, the samples were prepared over a broad range of deposition parameters using the two different deposition methods: ECR PECVD and reactive RF-Sputtering. Chemical vapor deposition (CVD) techniques, in general, operate much closer to the thermodynamic equilibrium when compared to the physical vapor deposition (PVD) techniques – in CVD, a chemical reaction requires energy scales of the order of tenths to tens of eV, while for PVD, the energy scale is shifted to several hundreds [78] –, so structural differences, and, notably, differences in the concentration of defects in the amorphous network were expected and investigated. These energy scale differences in the two methods are most prominent by the fact that Sputtering relies on the vaporization directly from a solid precursor whose binding energies are elevated when compared to the gas precursors used for CVD and Plasma enhanced CVD techniques.

A wide range of annealing temperatures was used to investigate the concentration of defects in the matrix. The films were annealed for 1h in N_2 atmosphere. The defects are represented by the Si-dbs. Fourier Transform infrared spectroscopy (FTIR) was employed to determine how Si-dbs density affect the PL emission of Tb^{3+} in ECR PECVD grown samples. One of the expected characteristics in the two groups of samples is a consistent difference in dangling bond concentration in films with similar chemical compostion which offers a framework for comparing Tb PL in the two sets of samples.

This work also includes a direct study of the chemical neighborhood of the Tb^{3+} ions in Tb doped a-$SiN_{1.5}$:H grown by reactive RF-Sputtering films through EXAFS absorption spectroscopy of the L_{III} absorption edge of Tb. This study was conducted for samples which had undergone different annealing treatments (annealing with different temperatures in an inert gas atmosphere). Regarding the causes of changes in photoluminescence intensities from Tb ions caused by annealing with different temperatures, one of our earliest hypothesis was of possible alterations in the chemical neighborhood around Tb^{3+} ions. As it will be discussed more in-depth in Chapter 2, the crystal field, generated by the neighboring atoms, can vary the transition intensities changing the PL spectrum.

Moreover, it shows the first report of atom probe tomography (APT) studies in this system. The APT data were used for an atomic 3-D spatial reconstruction of the film composition. The measurements and characterization were made as a result of a collaboration with Prof. Gianluigi Botton and were conducted by Brian Langelier of the Canadian Centre for Electron Microscopy (CCEM) at McMaster University. The APT studies were conducted in films with high and low concentrations of Tb which had undergone annealing at very high temperatures (1200ºC).

1.2 Outline

This introduction contextualized the importance of the research in novel silicon based materials, compatible with CMOS processing, and directed the reader specifically to rare-earth doping of a-Si alloys as a potential route for the development of active layers for Si-LEDs. It also raised relevant information available about Tb doping in Si-based alloys. An overview of the material studied and the methods employed was also provided. A more in-depth description, with more details, will be presented on the subsequent chapters. The rest of this section is dedicated to outline each of the chapters presented in this work.

Chapter 2 has some background information on the spectroscopic properties of Rare Earth elements– their electronic structure, transition intensities and radiative and non-radiative processes. In Chapter 3, the focus is directed towards general aspects of tetrahedrally coordinated amorphous semiconductors and some electronic and optical properties of amorphous silicon. The existent models for photoluminescence properties in rare earth doped a-Si:H are also covered.

Chapters 4 and 5 presents experimental background information regarding the growth systems' specifications used in sample preparation and the characterization methods employed. Along with it, details of the samples, such as optical characteristics and chemical composition, are presented. A comparison of film properties between RF-Sputtering ECR PECVD grown samples, is also provided.

The results and discussion were condensed in Chapter 6. Information regarding the chemical environment around Tb^{3+} ions and atomic distribution reconstructed from APT are presented for samples submitted to thermal annealing at different temperatures. Effects of concentration quenching of the Tb^{3+} photoluminescence are presented. Emphasis is given to the experimental data consistency with the defect related Auger excitation model, originally proposed for Er^{3+} in a-Si:H, that resulted from studies of the Si-H and N-H vibrational properties given by Fourier transform infrared spectroscopy.

Conclusions and perspectives are in Chapter 7.

2 Considerations on Rare Earth Spectroscopy

Atoms from the lanthanide family form a subgroup of a slightly bigger family denoted by Rare Earths (RE) – which includes yttrium and scandium [79]. When they are embedded in insulators, they preferably ionize to their trivalent state [80], RE^{3+}. Their optically active electrons are within the 4*f* shell, but, their valence electrons do not participate in bonding because of the shielding from their neighborhood generated by the 5s, 5p and 6s shells – see Figure 3. One consequence of this is the fact that Rare Earth ions emit narrow lines due to their intra 4-*f* electronic transitions, which means that their electronic structure can be described, in first approximation, through pure atomic physics, i.e., the system is first treated as if the lanthanide ion was isolated. Nevertheless, the atomic transitions involve initial and final states of the same parity which are electric dipole forbidden. This constraint is partially relaxed when the atoms occupy non-centrosymmetric lattice sites. In this case, the solutions to Schroedinger's equation can be expressed as linear combinations of eigenfunctions of the free ion and the transitions become partially allowed. The transition probabilities depend very strongly on the detailed chemical environment of the RE^{3+} ions that determine the symmetry of the sites and the local electrical fields - the crystal field.

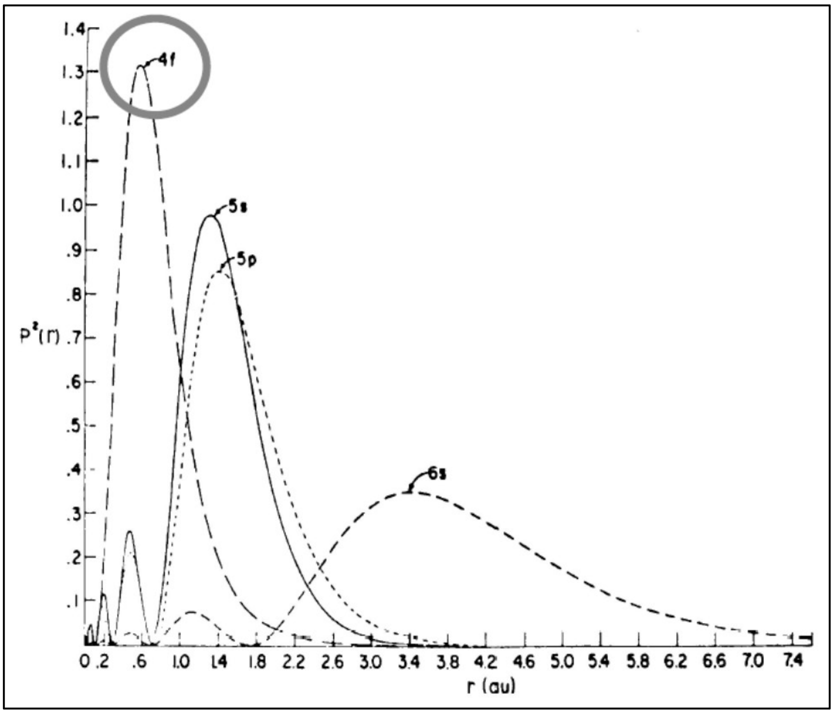

Figure 3: Radial Distribution Function for 4f, 5s and 6s electron shells calculated for Gd^{3+} using Hartree-Fock's method. It is a textbook example of how well inside and shielded the 4f shell is. Adapted from [81]

In this chapter, a short review of RE spectroscopy is presented and then applied to the case of trivalent terbium ion (Tb^{3+}). More specifically I will present the electronic energy structure, the effective Hamiltonian applicable to the system, the eigenstates nomenclature system, the Judd-Ofelt theory, some of the energy transfer mechanisms important for RE excitation (sensitization) and the DRAE excitation model.

This section is based in standard texts like: G. Liu, "Electronic Energy Level Structure" [82] and, more recently, in J. C. G. Bünzli and S. Eliseeva, "Basics of Lanthanide Photophysics," [79].

2.1 Electronic Structure of Trivalent Lanthanide Ions (RE^{3+})

2.1.1 Free Ion

The Hamiltonian of the free N-electron atom, without considering relativistic effects, many body interactions and nuclear movement can be written as [82]:

$$H_0 = -\sum_{i=1}^{N} \frac{\hbar^2}{2m} \nabla_i^2 + \sum_{i=1}^{N} \frac{Ze^2}{r_i} + \sum_{i<j}^{N} \frac{e^2}{r_{ij}} + \sum_{i=1}^{N} \zeta(r_i)\, \boldsymbol{L_i} \cdot \boldsymbol{S_i} \tag{1}$$

where the first term is the kinetic energy of the electrons; the second is the electron-nucleus attraction; the third is the mutual interelectronic repulsion between an i-j pair separated by a distance r_{ij}; the fourth a is the spin-orbit term that can be interpreted semi classically as a magnetic dipole-dipole interaction between orbital and spin magnetic dipoles mediated by the $\zeta(r_i)$ function.

This Hamiltonian obviously does not have an analytic solution for N>1 and must be solved using approximations. In the first place, the problem is solved for each electron separately, i.e., the solutions for the H atom are used for each electron. The energy is assumed to be constant with time. The Born-Oppenheimer approximation is used: the nucleus is fixed from the electron's point of view. The perturbation method is used, that is, the diverse interactions occurring in the electron-nucleus system are treated separately in decreasing order of magnitude.

The most usual way of solving it is self consistently through the Hartree-Fock's method [83]. In this method, the central free ion Hamiltonian, without considering the L-S term, is substituted by equation 2 where each electron moves independently under the action of an average central field, $U(\boldsymbol{r_i})$, which depends over the i^th electron and represents the effective repulsion potential that is applied to it by the other electrons and the nucleus – eq. 3.

$$H'_0 = \sum_{i=1}^{N} -\frac{\hbar^2}{2m}\nabla_i^2 - U(r_i) \tag{2}$$

$$\sum_{i=1}^{N} U(r_i) = -\sum_{i=1}^{N} \frac{Ze^2}{r_i} + \left\langle \sum_{i<j}^{N} \frac{e^2}{r_{ij}} \right\rangle \tag{3}$$

Nevertheless, eq. 3 does not have all the interelectronic repulsion since [82]:

$$\sum_{i=1}^{N} \frac{Ze^2}{r_i} \neq \left\langle \sum_{i<j}^{N} \frac{e^2}{r_{ij}} \right\rangle \tag{4}$$

In this way, the third term in equation 1 is substituted by:

$$H'_C = \sum_{i<j}^{N} \frac{e^2}{r_{ij}} - \left\langle \sum_{i<j}^{N} \frac{e^2}{r_{ij}} \right\rangle \tag{5}$$

This is known as the residual Coulombic interaction which is small enough to be treated by the perturbation method.

Equation 2 operates in the N electron space which constitutes the atom, that means, is an operator for the complete system. Because it depends upon a central potential, which depends only on the ith electron coordinates, it is possible to separate it into a collection of monoelectronic hydrogen like equations – also called orbitals – and consider each electron moving independently. To be more precise, the angular part of the solutions is solved exactly and separated from the radial part which is constructed from a self-consistent method (Hartree-Fock method). In this method, an initial wavefunction is guessed, usually takes the form of a solution of the hydrogen atom and then used for computing the average central potential. Using this potential, new wavefunctions are constructed which, in principle, are closer to the true solution. With these new solutions, a new average potential is constructed and the process is repeated until the obtained wavefunctions do not significantly change within the calculations precision. For more details on the method, please refer to [84], [85]. Figure 3 gives some results of such calculations for the case of Gd^{3+}.

In this way, it is possible to use the solution for the H atom to construct the multi-electron wavefunction. This function must obey Pauli's exclusion principle and so is given by a Slater's determinant of the one-electron wavefunctions which are occupied in crescent order of energy. This determinant is what gives the microstate of the atom and is related to what is called the atom's electron configuration; usually represented by the quantum numbers of the last occupied orbital with the occupancy number – the number of electrons in that orbital. In the case of the trivalent lanthanides ions they would be represented only by $4f^{N}$ [82], [86]. Table I illustrates the order of magnitude of different contributions to the electronic structure [82].

Table I: Energy level splitting scale from different contritutions. Adapted from [82]

Interaction Mechanism	Energy (eV)
Configuration	10
Residual Coulombic interaction	1
Spin-Orbit Interaction	0.1
Crystal Field Interaction	0.01

2.1.2 LS Coupling

To build the wavefunctions of the multielectronic atom is necessary to choose the way the angular momenta of each electron couple together in each shell.

There are two special kinds of coupling schemes. Each one is best employed in two different possible extremes: residual Coulombic interaction is bigger than spin-orbit's and the opposite. For the first case, the LS coupling, often referred to as Russel-Saunders scheme, gives the best coupling. In this case, we count each orbital by the shell's total orbital and spin angular momenta and total angular momentum, J, is given by $\mathbf{J} = \mathbf{L} + \mathbf{S}$. For the latter, the best coupling is the j-j in which each electron's spin and orbital angular momenta couple together and the total angular momentum is given by $\boldsymbol{J} = \sum_{i=1}^{N} \boldsymbol{j_i}$.

In the LS coupling, the multielectron states are represented by 6 quantum numbers, $|nl\tau LSJM\rangle$, where *n* and *l* give electronic orbital configuration of the most energetic state (or 4*f*, in the trivalent lanthanide ion fundamental level). It basically represents the radial part of the wavefunction. The other quantum numbers are represented through the spectroscopic notation $^{2S+1}L_J$, where J is the total angular momentum ($\mathbf{J} = \mathbf{L} + \mathbf{S}$) and M its z-component. The number τ symbolizes additional quantum numbers necessary to individually define the state (hyperfine structure). [87]

2.1.3 Crystal Field

In the previous sections, we made an overview of the electronic energy level structure without considering the effects of the host medium. The common physical interpretation of the main interactions of the Hamiltonian of the free ion was given. In this section the basics of the interactions of the neighboring atoms that surround the RE^{3+} ion, the crystal field contribution, will be developed. [81]

The crystal field is introduced in the form:

$$H = H_{FI} + H_{CF}$$

where H_{FI}, is the free ion contribution, already discussed in previous sections and H_{CF}, the crystal field contribution. It is often expressed by:

$$H_{CF} = \sum_{i,k,q} B_q^{(k)} C_q^{(k)}(i) \tag{6}$$

where the $Y_{k,q}$ operators are irreducible spherical tensor operators that are, operating for the i^{th} electron, defined by following expression with the spherical harmonics, $Y_{k,q}$:

$$C_q^{(k)}(i) = \sqrt{\frac{4\pi}{2k+1}}\, Y_{k,q}(\theta_i, \phi_i)$$

They are often represented by the effective operator for the entire shell by:

$$C_q^{(k)} = \sum_i C_q^{(k)}(i)$$

The matrix elements, $\langle nlSLJM | C_q^{(k)} | nlS'L'M' \rangle$, of these operators are numerically calculated and do not depend of the ion's site symmetry. They are given in tables and modulated by the complex crystal field parameters $B_q^{(k)}$they completely describe the crystal field interaction [81], [88].

One interesting property of the crystal field Hamiltonian is that it presents the same symmetry as the site the RE^{3+} is embedded in. That means, it must obey the same set of rotation, reflection, and inversion rules as the site the lanthanide ion occupies. Consequently, some restrictions, beyond the selection rules given for the angular momentum, must be valid to the $C_q^{(k)}$operators. In practical terms, only a subset of the allowed values of k and q are valid depending on the site symmetry. Consequently, that shrinks the number of $B_q^{(k)}$ parameters necessary for the full description of the system. Table II shows some examples of non-zero values of $B_q^{(k)}$ for different site symmetries.[89]

As they are defined, the crystal field parameters depend on the orientation of the reference axis and sometimes is very difficult to compare their values for different hosts. With the purpose of overcoming the comparison problem an average, reference system orientation independent, crystal field strength is defined by the expression [82], [89]:

$$N_v = \left(\sum_{k=2,4,6} (S_k)^2 \right)^{1/2}$$

$$S_k = \frac{1}{2k+1} \sum_{q=-k}^{k} |\hat{B}_q^k| = \frac{1}{2k+1} \left[B_0^k + 2 \sum_{q=2,4,6} Re(B_q^k) + Im(B_q^k) \right]^{1/2} \tag{7}$$

A summary of what has been presented in the last few sections is represented schematically in Figure 4. It shows, for the specific case of Tb^{3+}how the different interactions present in the RE^{3+} system split the energy level structure.

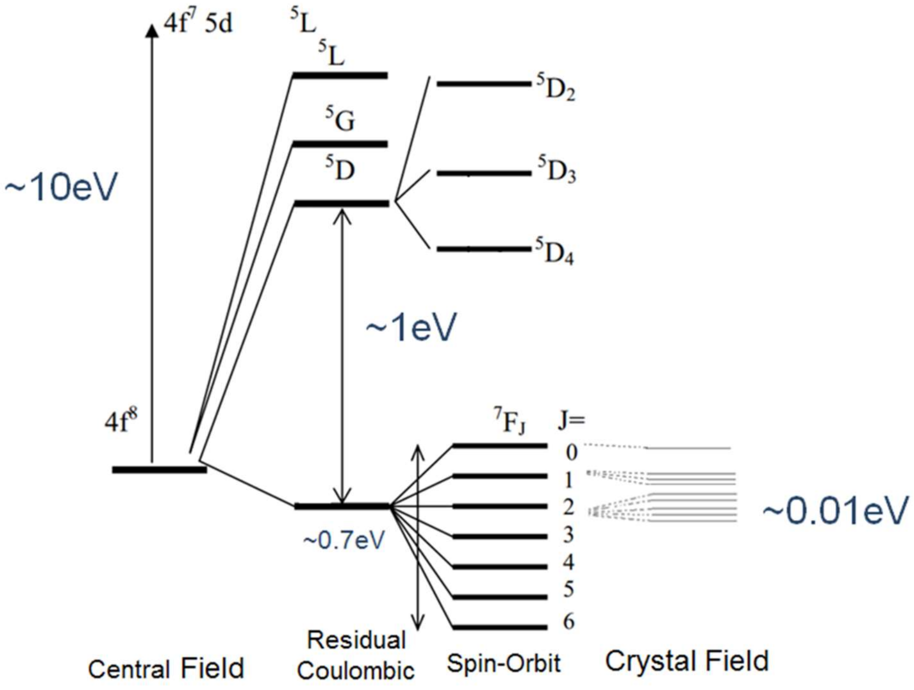

Figure 4: Rare Earth ion energy level structure for the Tb^{3+} case – also representative of the Tb^{3+} energy level structure. The energy levels between different contributions to the Hamiltonian are out of scale. [90]

Table II: Non-zero crystal field parameters for three different site symmetries of common occurrence in the literature. R and E indicate respectively the real and imaginary parts of the parameters. [89]

k	|q|	C_{3V}	C_2	D_{4h}
2	0	R	R	R
2	2	--	R,I	--
4	0	R	R	R
4	2	--	R,I	--
4	3	R	--	--
4	4	--	R,I	R
6	0	R	R	R
6	2	--	R,I	--
6	3	R	--	--
6	4	--	R,I	R
6	6	R	R,I	--

2.2 Transition Intensity: Judd-Ofelt Theory

When looking to the intensities of electronic transitions, a direct application of Fermi's Golden Rule is necessary. In the discrete level form, it can be written:

$$W_{i\to f} = \frac{2\pi}{\hbar} \left|\langle \phi_i | H' | \phi_f \rangle\right|^2 \ \ \delta(E_i - E_f - h\nu)$$

where $W_{i\to f}$ is the transition rate between initial and final states; H' is the perturbation caused by the light wave (whose photon energy is given by $h\nu$). In first order, the light wave contribution if of electric dipole order ($H' = H_{ED}$), whose operator is given by:

$$H_{ED} = -e \sum_i \boldsymbol{r_i}$$

According to this rule, the intra-$4f$ transitions are electric dipole forbidden because the matrix element the initial and final states have the same parity – given by the quantum number l – and the electric dipole term is an odd term, that means, it couples only states with opposite parity [91]. Nevertheless, when the crystal field is "turned on", the centrosymmetric condition is usually broken and these transitions are "less forbidden". In other words, the crystal field imposes a preferential direction, breaking the spherical symmetry of the other interactions and, under the scope of first order time independent perturbation theory, it mixes the $4f^{\mathrm{N}}$ wavefunctions with wavefunction of opposite parity from higher order configurations – like the $4f^{\mathrm{N}-1}5d^1$, for example. Under the assumptions of a static and free ion that has a negligible configuration interaction, the intensity of the transitions between $4f$ levels can be explained through what is known as Judd-Ofelt theory [92], [93]. Its strength resides in the semi empirical approach capable of giving, within 10 to 15% error margin (for absorption measurements), the radiative lifetimes which are usually very complicated to observe directly.[94], [95]

Within the Judd-Ofelt theory, the absorption dipole line strength of the electronic transitions, represented in equation 8, is given in terms of three adjustable parameters and in terms of doubly reduced matrix elements for intermediate coupling.[79]

$$S_{f\leftarrow i} = \frac{1}{e^2} |\langle \psi_f | H_{ED} | \psi_i \rangle|^2 = \sum_{\lambda=2,4,6} \Omega_\lambda \, |\langle 4f^N SLJM \| U^{(\lambda)} \| 4f^N S'L'J'M' \rangle|^2 \qquad (8)$$

In Equation 8, H_{ED} is the electric dipole component of the time-dependent perturbation created by radiation; Ω_λ or Judd-Ofelt parameters, depend only on the nature of the free ion $4f^{\mathrm{N}}$ wavefunctions and give the crystal field effect considering radial integrals over $4f^{\mathrm{N}}$ wavefunctions and higher energy opposite parity states, divided by the energies separating these levels; the elements in double brackets with $U^{(\lambda)}$ are the reduced tensors for the electrical dipole operator within the intermediate coupling scheme characteristic of the 4*f* wavefunction nature, thus crystal field independent – their values are found in diverse tables.[96]

The three Ω_λ parameters are usually considered as phenomenological coefficients, which represent the crystal field influence upon the intra 4*f* transition probabilities, and are experimentally determined from absorption and emission experiments through a least squares adjustment.[94]

The dipole line strength is related to the oscillator strength, $f_{f\leftarrow i}$, through the expression:

$$f_{f\leftarrow i} = \frac{8\pi^2 + mc}{3h\bar{\lambda}(2J+1)} n \left(\frac{n^2+2}{3n}\right)^2 S_{f\leftarrow i} \tag{9}$$

where, *m* is the electron's mass, *n* the refractive index of the matrix where the lanthanide ion is embedded, measured at the average wavelength, $\bar{\lambda}$, of the transition; *h* is Planck's constant, *c* light velocity and *J* the total angular momentum of the upper level excited state.

Experimentally, these transition intensity parameters can be obtained from absorption measurements sensitive enough to get the absorption lines from the studied lanthanide. The line strength can be obtained from absorption cross section through the expression:[79]

$$S = \frac{3_{ch}(2J+1)}{8\pi^3 e^2 \bar{\lambda}} n \left(\frac{3}{n^2+2}\right)^2 \int_J \sigma(\lambda) d\lambda \tag{10}$$

The measured absorption cross section given by equation 10 can also be obtained from emission spectrum. In that case, it is essential to have in the first hand, though, information of the radiative lifetime (τ) and of the branching ratio (β). Equation 11 shows how to obtain the emission cross section from emission experiments in an isotropic medium [97]:

$$\sigma(\lambda) = \frac{\lambda^5}{8\pi c n^2 (\tau_r/\beta)} \frac{I(\lambda)}{\int I(\lambda)\lambda d\lambda} \tag{11}$$

2.3 Trivalent Terbium (Tb^{3+}) Energy Levels

Terbium (Tb) is the eighth element form the lanthanide family. Together with ytterbium, its name is another tribute to the village of Ytterby, Sweden, one of the most important stages for the RE discovery and initial science developments in the XIXth century [98]. It is metallic when pure and assumes the [Xe]$4f^9 6s^2$ configuration, when in the trivalent ground state though it loses the two electrons from the 6s shell and one in the 4*f* thus adopting the [Xe]$4f^{\,8}$ configuration. When diluted in insulators it emits strong green light under excitation, emission that has been extensively exploited over the last century in lighting and display applications [87]. Together with blue and red emission given respectively by divalent and trivalent Europium in an Yttrium based phosphor it was very used in the, now old, cathode ray tube technology for color television but it is still used in fluorescent lamps [99], [100].

The intra 4-*f* energy levels of Tb^{3+} are usually described within the L-S coupling per the standard notation $^{2S+1}L_J$. In this notation, S is the total spin angular momentum of the shell, so, with 2S+1 multiplicity; L is the total orbital angular momentum, written in spectroscopic notation: S, P, D, F and so on. to indicate, respectively, L= 0, 1, 2, 3, …; and J the total angular momentum which satisfies the angular momentum sum rules, $| L - S | \leq J \leq L + S$.[101][1]

The optical ground state is determined under the scope of Hund's rule. [102] According to this rule, for a given electronic configuration, the state with less energy is the one with maximum S and maximum L. Besides, it must have minimum J value if the 4*f* shell is occupied with less of its full capacity, if not, the fundamental state is the one with minimum J. Therefore, as Tb^{3+} has 8 electrons in the 4*f* shell the fundamental level must have $S_{max} = 7 \times \frac{1}{2} - \frac{1}{2} = 3$ e $L_{max} = 2.(3)+2+1+0-1-2-3 = 3$ (thus represented by the letter F). As the 4*f* shell is more than half-filled – 7 electrons – the J value for the fundamental level is the maximum S + L = 6. So, the fundamental level is represented by the spectroscopic term $^7F_6$. The first excited states are the ones with decreasing J values – towards the highest energy within the ^7F shell: 0. The next multiplet is the ^5D_J (J = 4, 3, 2, 1, 0) – see Figure 5.

---

[1] In fact, the most accurate coupling scheme to describe the RE^{3+} wavefunctions is the intermediate coupling which consists of a linear combination of pure L-S terms. This is because the spin-orbit interaction is of the same order of magnitude as the interelectronic repulsion. In the intermediate coupling the spectroscopic notation is the same as the one used for the L-S coupling for the dominant term.

In summary, the energy levels of Tb^{3+} consist of a ^7F multiplet well separated from the excited states composed by the ^5D_J multiplet. The $^5D_4$ level, the first excited state is 2.5 eV apart from the fundamental level $^7F_6$.

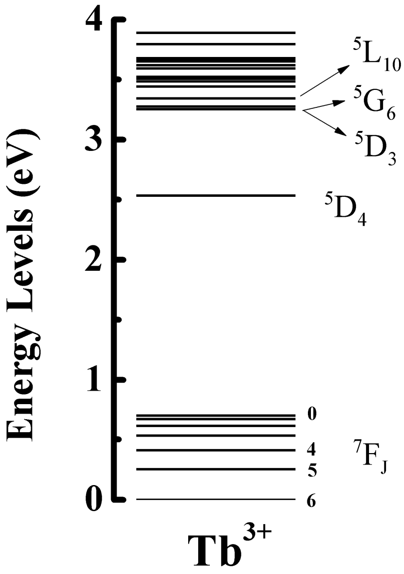

Figure 5: Energy level diagram for Tb^{3+} showing the ^5D and ^7F multiplets.

2.4 Luminescence and Non-Radiative Processes

One of the main concerns in developing efficient luminescent materials based on lanthanide luminescence is quenching. Lanthanide luminescence are characterized by long lifetimes (of the order of milliseconds [80]) and natural lifetime of a transition can always be described as composed by radiative and non-radiative contributions as follows [86]:

$$\frac{1}{\tau} = \frac{1}{\tau_r} + \frac{1}{\tau_{nr}} \tag{12}$$

One of the biggest quenching sources and, consequently, a big competing mechanism for luminescence is multiphonon relaxation. In this process, instead of emitting a photon, the transition is accomplished by the emission of several phonons. One general rule is that the process is less likely to happen when more phonons are required to bridge the gap. It states that, for absolute zero temperature, the non-radiative transition rate is given by [103]:

$$W_{NR}(T = 0K) = \beta_{el} exp[-\alpha(\Delta E - 2h\nu_{max})] \tag{13}$$

where the constant β_{el} contains electronic coupling information; ΔE is the energy gap between the two participating levels of the considered transition, $h\nu_{max}$ is the maximum phonon energy, and α is a constant for the host lattice.

The temperature dependence for multiphonon relaxation rate is given by [104]:

$$W(T) = W(0)\{1 + [exp(h\nu/kT) - 1]^{-1}\}^{p} \qquad (14)$$

where p is the number of phonons related to the relaxation process, and is given by ($\Delta E/h\nu$). Therefore, multiphonon relaxation is a process that is most probable as less phonons are involved, or, equivalently, when the energy separation between the energy levels are close enough.

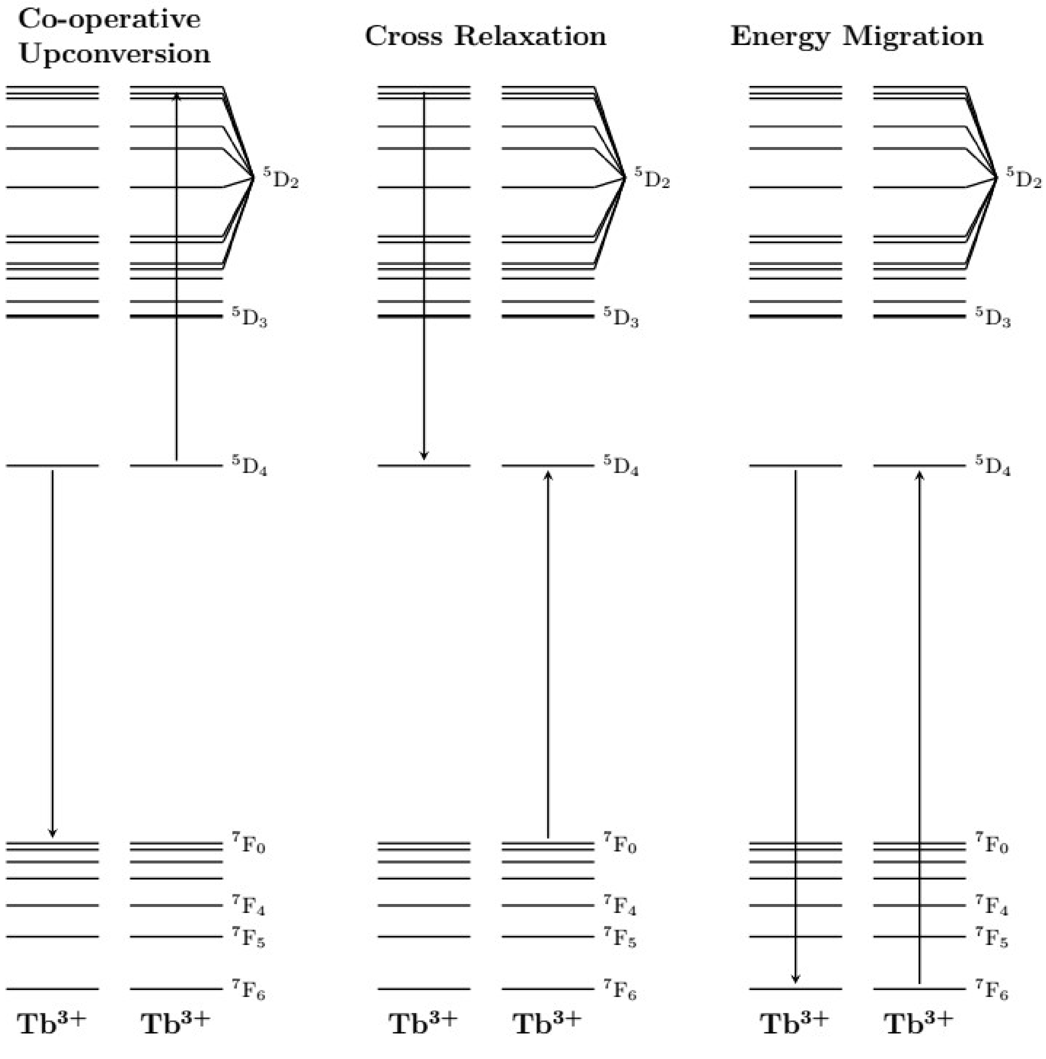

Figure 6: Possible non-radiative ion-ion processes occurring between two neighboring Tb^{3+} ions: co-operative upconversion, cross relaxation and energy migration. From [105].

Ion-ion interactions, or non-radiative energy transfer between two neighboring lanthanide ions is also an important nonradiative processes which is highly sensitive to the lanthanide ion density. They are usually relevant at higher concentrations. Three processes are predominant: energy migration, cross relaxation and co-operative upconversion. These three processes are depicted in Figure 6. Energy migration, the simplest of the three, involves one electron in a high energy metastable state while the other is its fundamental level. It is the non-radiative energy transfer from one excited electron to the fundamental level of another ion promoting it to the excited state where the first electron was occupying. Despite seemingly an event with no net impact, it does quench radiative emission as each event of migration prevents one photon emission.

Cross relaxation is an event like energy migration but involves two neighboring ions in excited states. One in a highly-excited level and the other in another state in such a way that the two electrons end up at the same energy state.

Finally, we have the co-operative upconversion, which is basically the opposite process of cross relaxation. Instead of the two electrons in the two ions ending up at the same energy level, they start at this configuration. One electron decays to the fundamental state promoting the neighboring one to a much higher energy level. Average Distance between Randomly Distributed Ions

One problem of importance in this work's discussion is the average distance between two ions of the same species randomly distributed in a solid. As it will be shown later, in the case of N-rich silicon nitrides, that is the case for Tb^{3+}. This problem, first considered by Hertz was initially discussed by Chandrasekhar [106] but in this work it will be applied a modified version, to account for the finite radius of Tb ions, not discussed in the original work of Chandrasekhar's, introduced by Benz, *et al.* [107]. In their approach, the probability density for the presence of a nearest neighbor in a spherical shell between r and $r+dr$ can be found to be:

$$\rho(r) = (r^2 - d_0^2)n\times e^{-\frac{4}{3}\pi(r^3-d_0^3)} \qquad (15)$$

The required average distance is then:

$$(r) = \frac{\int_{d_0}^{\infty} dr\rho(r)\times r}{\int dr\rho(r)} \qquad (16)$$

where n is the atom density, d_0 is the minimum distance between two Tb^{3+} ions which can be approximated to be two times its ionic radius.

3 Amorphous Silicon

Different from its crystalline counterpart, amorphous silicon does not have translational symmetry. This does not necessarily mean that the atoms are randomly positioned in the matrix. In fact, the covalent bonds of Si atoms with other elements are, in average, very much the same as it is expected from covalent bonds between Si atoms in a perfect Si crystal having almost the same coordination number and bond angles - ± 5º around the full coordinated perfect sp^3 bond. Despite lacking the long-range order, characteristic of the crystals, mostly due to this distribution of bond angles, amorphous Si still presents what it is called short range order as their crystalline counterpart. The atomic arrangement nearby a reference atom is very similar to the corresponding crystal. [108]–[110]

Disorder is very often represented by the atom pair distribution function, or radial distribution functions (RDF), which is the probability of finding an atom in a spherical shell of radius *r* apart from another one, in the shell's center [111]. In phases of matter with true random positioning of atoms, such as dilute gases, except for very short distances, we would have the same probability to find another atom whatever the distance from its center – a constant RDF. That is not the case in amorphous materials. As Figure 7 points out, amorphous semiconductors still preserve atomic ordering in the first shells of neighbors, due to the presence of peaks in the RDF function which share the same positions as the delta-like, or well defined, atomic spacings present in a crystal.

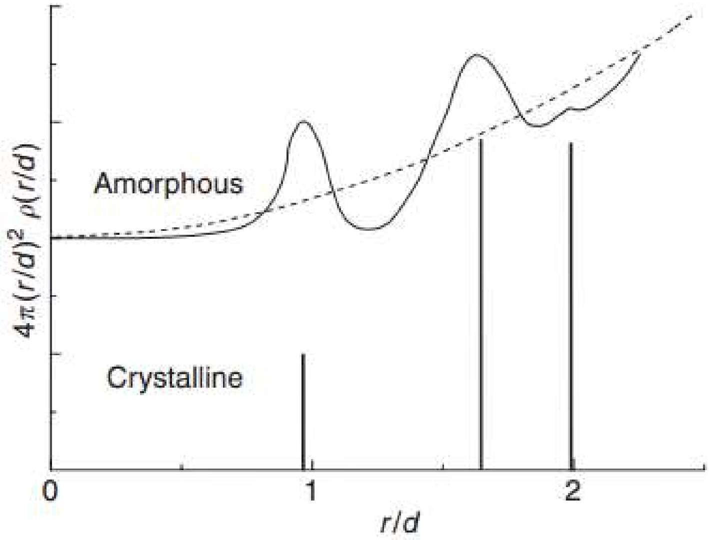

Figure 7: Radial Distribution Function (RDF) of both amorphous and crystalline Si at 0K. The abscissa is in units of bond lengths characteristic of a perfect crystal phase. It is noticeable that from the third peak on, the RDF loses coherence. From [110].

Amorphous silicon has as trait, beyond the lack of long range order, the presence of weaker bonds; twisted and tensioned bonds. Moreover, there are the common presence dangling bonds, when neutral, composed of one electron that is not shared with any other atom. These are normally called defects in amorphous materials and can be passivated by hydrogenation. Dehydrogenated films have higher density of defects which prevents any characteristics that are desirable for a semiconductor intended for electronic applications.

3.1 Electronic Band Structure in Amorphous Semiconductors

The standard, and, often, first introduced approach in solid state textbooks for the formation of bands and the existence of bandgaps in the electronic structure of solids supposes translational symmetry, or periodicity in the lattice, as the most important hypothesis. This is the base of the free electron theory and one of the consequences is the Bloch's wavefunctions as the one electron solutions for the problem. That is the main reason why, historically, there was a debate of even whether an amorphous semiconductor had a band gap at all! [109]

One breakthrough for a clear understanding of the presence of bandgaps and their formation in amorphous semiconductors came out with Weaire and Thorpe's work [112] who described the solid using a tight binding Hamiltonian approach, taking into account only the first neighbors. The Hamiltonian is represented in Equation 17:

$$H = V_1 \sum_{j \neq j'} |\phi_{ij}\rangle\langle \phi_{ij'}| + V_2 \sum_{i \neq j'} |\phi_{ij}\rangle\langle \phi_{i'j}| \qquad (17)$$

The first term is the sum of interactions over sp^3 hybrid electronic wavefunctions of the same atom, denoted by i. The second term, though, is a sum of interactions of the same orbital from the same bond, j. It does not suppose long range order. With this only, they could show that, irrespective of periodicity, there is band gap formation if the ratio of the interactions intensity, V_1/V_2, is within specific intervals.

As the energy bands are more strongly influenced by the short-range order, materials like amorphous SiO_2 are insulators just like their crystalline phase, a-Si is a semiconductor and so on. That explains why the amorphous counterparts of known crystalline materials preserve the bandgap. Figure 8 illustrates the method, for the special case of a-Si, showing the hybrid atomic orbitals that, can give rise to the bands and to the band gap in amorphous semiconductors.

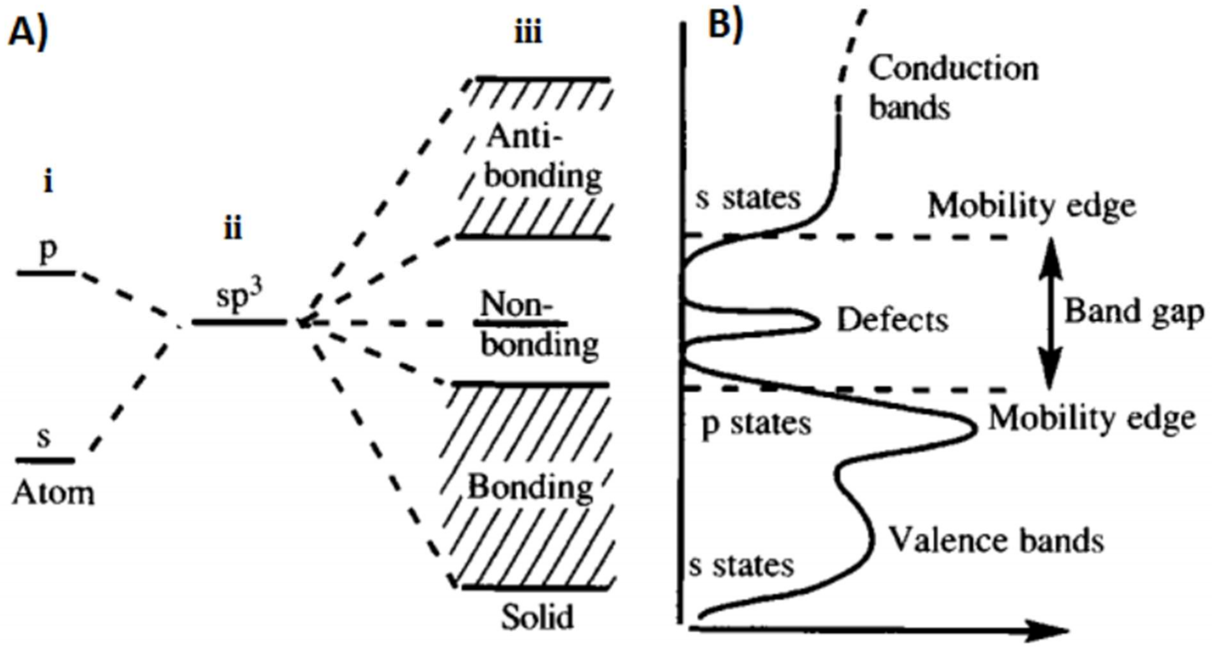

Figure 8: Origin of valence and conduction band states from a tight binding point of view for a-Si. (a) In (i) are given the pure s and p atomic orbitals; (ii) sp^3 hybrid states; (iii) bonding and anti-bonding states from sp^3 orbital interactions, and (iv) broadening of bonding (σ) and antibonding ($\sigma*$) into valence and conduction bands as a result of bringing the atoms closer (condensation). (b) Density of states (DOS) for such a scheme. There is a presence of a tail from the mobility edge towards the gap for both valence and conduction bands. At the middle of the gap, are the energy states corresponding to the neutral dangling bonds. The character of the extended states near the top of the valence band are p-like orbitals while the character of the extended states at the bottom of the conduction band is s-like. Adapted from [109].

In contrast, disorder and the lack of long range order has a very important implication. Electron wavefunctions tend to be localized in space. The breakthrough that allowed the understanding of the origins localization is the Anderson localization model – see Figure 9. According to it, the crystal is described as a collection of potential wells, each of them having the same depth and a width B. To describe the amorphous phase, a random potential with a mean amplitude, V_0, is added to the potential of each site. He showed that, for three dimensions, when the V_0/B ratio exceeds a critical point, the one electron wavefunction is completely localized.

Alternatively, but still using Anderson's model to illustrate, the origin of the localization of the electron's wavefunction can be intuitively thought of as the consequence of multiple scattering from potentials with a distribution of depths. From crystal theory, it is known that a small perturbation in the periodic potential, the presence of an impurity atom, for example, causes scattering in the electron wavefunction, making the electron to change its momentum. Transposing it to the amorphous case, when the disorder is strong, these wavefunctions would rapidly lose their phase coherence. That means they carry a large uncertainty in their momentum, which, per Heisenberg's uncertainty principle would mean that the uncertainty in the electron position can not be infinite, or the size of the whole crystal. In fact, the consequence is the confinement of the electron within few atomic distances.

The localized character of the electron's wavefunctions in amorphous semiconductors is recall of momentum conservation for electronic transitions. This means that the wavefunctions can not be described by Bloch's functions – known to be completely delocalized. Considering Heisenberg's uncertainty principle again, it means that, in a crystal, presence of electrons with very well defined momenta. So, its use as the quantum number to determine electron's state within a band in a crystal. In this manner, we have importance of knowing the E x **k** dispersion to describe the crystal's electronic and optical properties. This is not the case for the amorphous semiconductors though. Their electronic states are spatially localized rendering momentum uncertainty of the same order of its momentum! Thus, electronic transitions are not constrained to momentum selection rules. Consequently, the distinction between direct and indirect semiconductors is also lost.

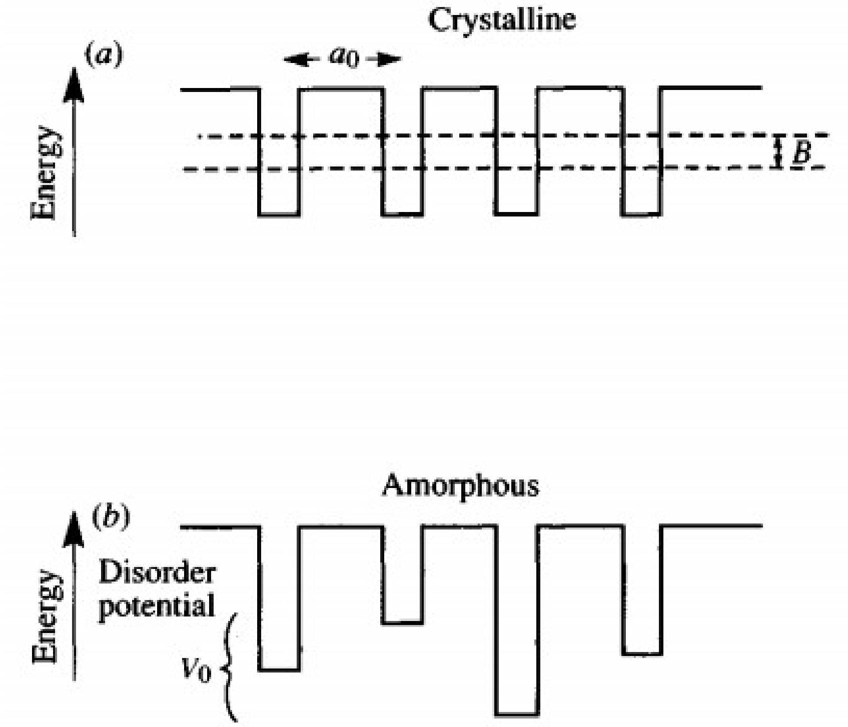

Figure 9: Anderson model of potential wells. a) crystal case and b) the amorphous problem. V_0 is a measure of the disorder. From [109].

3.1.1 Mobility Edge and the Band Tails

The fact that amorphous semiconductors have localized electronic states, does not necessarily mean that all states are localized. In fact, amorphous Si also have delocalized states, or, in the jargon used in amorphous literature: extended states. These states arise from fully coordinated near perfect tetrahedral Si sp^3 bonds which are more stable and energetic than the tensioned, weaker bonds which come from the natural disorder of the amorphous Si. So, the extended states always lie deeply inside the bands while the weaker, disordered bonds go to the bandgap giving origin to band tails in the density of states (DOS) - depicted in Figure 10. If we use again the comparison with crystals, instead of having sharp band edges in the DOS we would have a smooth distribution from the extended states towards the center of the bandgap. More than that, the energy bands are also characterized by the presence of an edge which separates the extended states from the tail states. This edge is called simply by “mobility edge”. Because the states in the tails are localized then it is not expected any electrical conduction at 0 K. That is expected only when the electrons belong to extended states, with much better mobility. This energy line from which extended states are separated from localized ones is the mobility edge. [110], [113]

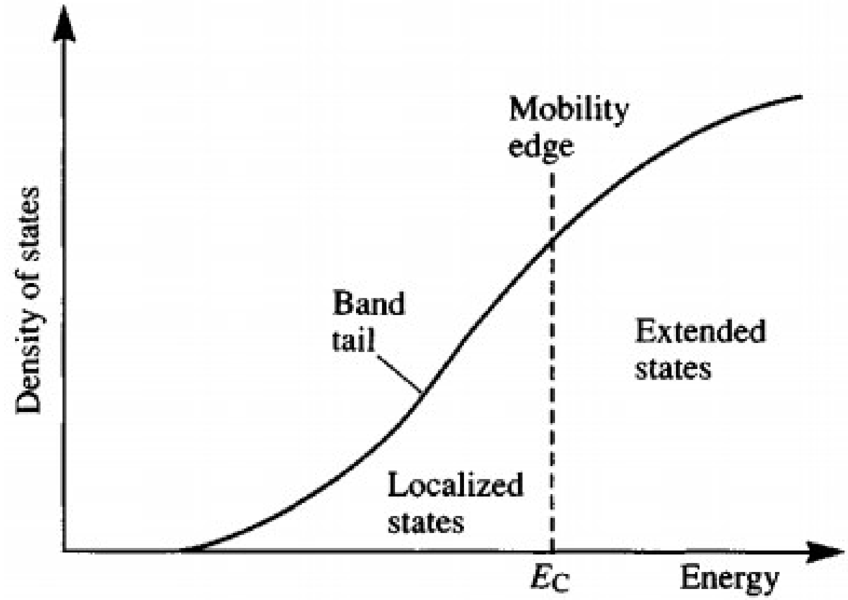

Figure 10: Density of states near the mobility gap separating localized from extended states. After [109].

3.1.2 Dangling Bonds

The atoms that compose amorphous semiconductors are, very often, not fully coordinated. In the specific case of nitrogen rich a-SiN_x:H, it means that a Si atom could be bonded with only three atoms, instead of four, or that a N atom would be bonded to just two. These sometimes called “coordination defects”, or dangling bonds leave, in the neutral state, an unpaired electron state that does not covalently bond to any other.

There are three possible types of Si dangling bonds (Si-dbs): D^0, D^+ or D^-, that is, neutral, positively charged or negatively charged dangling bonds. While the neutral Si-dbs lie in the middle of the bandgap, positively or negatively charged can lie below or above neutral’s depending on the material’s electron-phonon interaction magnitude (sometimes referred to as U-effect [110]). For materials with weak electron-phonon interaction, D^- states lie slightly above the neutral’s-dbs, while D^+ lie below. The opposite is valid when the electron-phonon interaction is strong, which is the case for nitrogen rich a-SiN_x:H [114]

3.2 Optical Properties

3.2.1 Absorption and Urbach Tail

Figure 11 represents the typical absorption coefficient of an amorphous Si based thin film as a function of photon energy around the mobility edge region. As the log α curve shows, there are three distinct regimes of photon absorption: A) the highest energy portion, which is related to transitions between extended energy states; B) the mid portion, related to the tail to extended states and, finally; C) the lowest energy portion, which represents transitions between dangling bonds and the extended states.

In region B, the α dependency can be expressed by $\exp(\hbar\omega/E_u)$, where E_u indicates how abrupt the dominating band tail is: the Urbach tail [115].

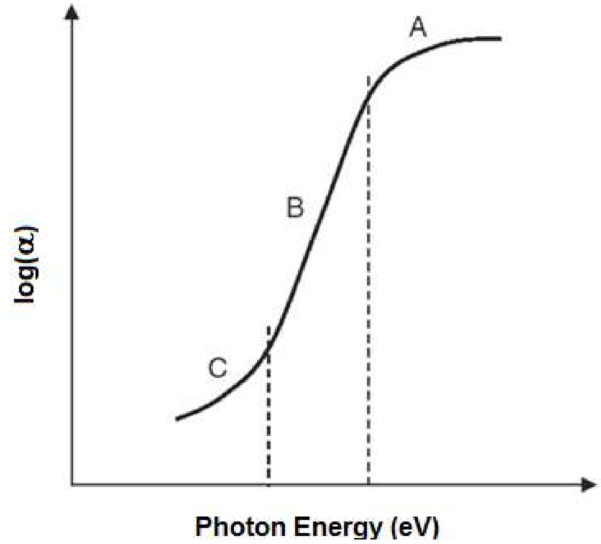

Figure 11: Absorption curve typical in amorphous silicon materials. It show three main absorption regimes: A, B and C. Adapted from [110].

3.2.2 E_{04} Gap

Usual gap definition for crystalline semiconductors don't make much sense in the case of amorphous materials. For crystals, it is very straightforward and directly means the interval of energy values where there is total absence of energy states. This definition is not very suitable for amorphous semiconductors because there is no such a region in their states distribution in energy.

A suitable gap definition considers carrier conduction at 0 K. The mobility gap is defined as the separation in energy between the mobility edges of the valence and conduction bands. At 0K carriers with energy below the mobility gap have zero mobility and thus cannot transport charge.

Experimentally, though, it is not easy to determine the mobility gap. One obvious reason is the difficulty of achieving temperatures near 0 K at everyday equipment used for optical characterization. Nevertheless, it is experimentally verified and tested that this gap definition is usually close to the energy of the photon for which the absorption coefficient is 10^4 cm^{-1}. That is precisely what is known as the optical gap or E_{04}. [109]

Other common gap definition is Tauc gap. Obtained from the extrapolation of the linear part of the $(\alpha h\nu)^{1/2}$ vs $h\nu$ plot to the energy axis, this plot needs the quantity $(\alpha h\nu)^{1/2}$ to be linear over at least one decade [116] for a completely unambiguous Tauc gap determination. This condition is not very often found in the nitrides produced in this work because they were very transparent.

Since the E_{04} gap is very strictly defined, we opted for using it as our gap definition for the optical absorption description purposes.

3.2.3 Recombination and Thermalization

When a-Si:H is exposed to an external source of light, excess carriers are generated initially populating the extended and localized states at the band edges. These carriers interact among themselves and with the network giving origin to a series of different phenomena of which one is the photoluminescence (PL). Its study, accompanied by complementary techniques such as radiative lifetime measurements and excitation photoluminescence, for example, can give much information about the nature of the gap states as well as the recombination mechanisms within the studied material.

The whole recombination process in solids consists of two different steps for above gap excitation (as illustrated in Figure 12):

a) right after excitation, the carriers constantly lose energy by many transitions within the band, at which they are located, losing small amounts of energy by emitting phonons. As energy is lost, the carriers eventually fall in the localized states where the transition rate decreases significantly. This process involves the emission of single phonons when the carriers are still at the extended band states (with a time rate of the order of 10^{-13} s); tunneling when they are at the localized band (time rate in the range of 10^{-8} to 10^{-5} s) or even multiple trapping, in which the carrier is excited to the mobility edge and then recaptured by a different tail state. This whole process is often referred to simply as thermalization;

b) Large amounts of energy can often be released from carriers at localized states when they recombine at the deep, and strongly localized, defects that are located at the middle of the gap – recombination. It can occur either radiatively, by emission of one photon – which has a much greater probability than by emission of two or more – or non-radiatively, with the involvement of multiple phonons or even by an Auger process (which involves third carrier - when the energy released by one e-h pair recombination excites another electron).

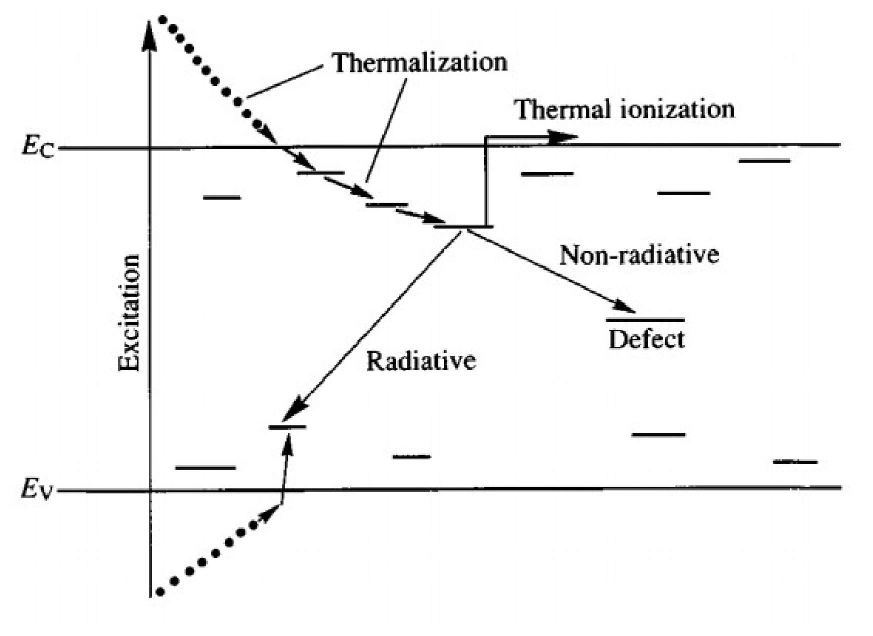

Figure 12: Diagram illustrating the typical recombination process that takes place in amorphous semiconductors. After R. A. Street [109].

3.2.4 Photoluminescence Spectrum (PL)

The PL spectrum shape of a-Si:H is a featureless nearly Gaussian single peak that it is somewhat 400 meV below the optical band gap and has a width of about 200-300 meV [117]. Moreover, the emission peak redshifts when the excitation energy is reduced below the bandgap energy by, approximately, 400 meV below the excitation energy [118]. Since the PL spectrum does not have features, as compared to the crystalline Si, many models can be used to fit the data. Historically, two models were of greater importance for interpreting the PL spectrum: Stokes-shift model [117], [119] and a static disorder model [120], [121].

In the static model, the PL spectrum is given in terms of probabilities of occupation multiplied by the probabilities of radiative recombination from a given state determined by its energy, defined below the material's bandgap [121]. The PL spectrum is the result of a convolution between the density of carriers over the two band tails in states that are the lowest in spheres of volume V_c – within each is the maximum distance over which the carriers can thermalize before they recombine radiatively. The density of such states is given by:

$$P_i(\epsilon) = N_{0i}\exp(-\beta_i\epsilon)\exp[-V_cN_{0i}\beta_i^{-1}\exp(-\beta_i\epsilon)] \quad (18)$$

where, i indicates the band (valence or conduction), N_{0i} the density of states at the mobility edge in band i, ϵ the energy below the mobility edge, V_c the volume of thermalization and β_i the inverse of the characteristic energy of the exponential density of states for band i, identified with the reciprocal of the Urbach energy $(1/E_u)$.

The equation above has a slightly asymmetric Gaussian profile with maximum at ϵ_{max} given by [116]:

$$\epsilon_{max} = \beta_i^{-1}\ln(V_cN_{0i}\beta_i^{-1}) \quad (19)$$

The width of the curve depends only on the Urbach energy and is roughly equal to [116]:

$$\Delta\epsilon_i \approx 3\,\beta_i^{-1}$$

Equation (18) is, indeed, a good approximation of the PL band shape itself. Due to differences in the characteristic energies for the two band tails, the density of states of the valence band tail is much wider, typically of the order 3 times, than the conduction band tail [122].

3.3 Silicon Nitride, Electronic Structure, and PL

Given the basic concepts related to amorphous silicon outlined in the last sections, focus will be now directed to the electronic properties of the material that was investigated in this thesis: a-SiN_x:H. There is plenty of literature covering most aspects of it, but some aspects regarding its electronic properties and the states in the gap will be reviewed in the next sections. All the material covered here was selected and adapted from five papers of Warren, Robertson and coworkers [74], [114], [123]–[125].

The structure of a-SiN_x:H alloys consists of a random network composed mainly of Si–Si and Si–N bonds. According to first principles calculations by Jarolimek *et al.* [126], the short range order remains up to the second neighbor shell, very similar to the two crystalline phases of Si_3N_4, where the Si atom are bonded to 4 N atoms, defining tetrahedral angles distributed around 109º, and N bonded to three Si atoms in a planar configuration with angles around 120º. The presence of N–N bonds is very rarely found, especially in Si-rich materials [126], so there is very little evidence of their existence. Their absence is attributed to their low stability when compared with the triple bonds which form molecular nitrogen.

Hydrogen, as in the a-Si:H case, has an important role in the electronic properties of the nitride alloys. It passivates both Si and N dangling bonds and thus lowers the density of states associated with them. The Si-H bonds are more abundant in Si-rich samples while N-H dominates N-rich samples. N–H bonds are the most responsible for raising gap size – up to the point where it exceeds the stoichiometry point ($x = 1.33$) [125]. Hydrogen can also be found in its molecular form inside micro voids spread across the film [126]. H incorporation is very dependent on the deposition technique used and the precursor gases chosen (NH_3, N_2, H_2 and so on). Concentrations of up to 40 at.% (both bonded as non-bonded to Si and N) have been reported [127].

The electronic structure of silicon nitride alloys has a lot of similarities with the mentioned afore electronic structure of a-Si:H. It can be characterized by the presence of extended and localized states separated by a mobility edge generally associated with an E_{04} gap. The density of states at the tails can also be considered approximately exponential following an Urbach relation and there is presence of very localized defects in the middle of the gap. Nevertheless, there are some important differences.

Table III: Bond energies between elements which composes the network of a-SiN$_x$:H. [125]

Bond	Energy (eV)
N-N	1.70
Si-Si	2.34
Si-H	3.10
Si-N	3.45
N-H	4.05

The replacement of Si–Si by Si–N with increasing x in the films increases the band edges distances and, consequently, the optical E_{04} gap, due to the higher binding energy of the N related bonds – see Table III. According to Robertson *et al.* [123], this occurs very slowly until $x \approx 1.1$. Then the optical gap increases rapidly up to a point where it gets saturated around 5.5 eV.

The critical concentration of $x = 1.1$ (not 1.33) described above, is often referred to as the percolation threshold of Si–Si in the SiN$_x$ network. Percolation here refers to simplified lattice models of random system networks while the threshold is the critical occupancy probability such that there is a big connectivity between the Si–Si bonds. This threshold clearly separates two different electronic structures for the SiN$_x$ network. While $x < 1.1$, in unhydrogenated films the band tails are predominantly formed by Si–Si like states. Above $x \approx 1.3$, the valence band tail is composed by N pπ like states while we still have the weak Si–Si antibonding σ^* states at the conduction band tail.

The opening of the bandgap is roughly symmetric around its center, depicted in Figure 13. For Si-rich hydrogenated films, deep Si-H states, instead of Si–Si, composes the conduction band tail, which makes E_v in general 0.8 eV lower than in the unhydrogenated case. In the N-rich phase, with gap of the order of 5.5 eV, coincident with that of stoichiometric Si_3N_4, is only achieved for $x > 1.5$, a value significantly higher than the 1.33.

The PL band shape of amorphous silicon nitrides obeys roughly the very same mechanism used to explain the PL of a-Si:H [128] – already described in section 3.2.4. Figure 14 illustrates the natural PL spectrum of PECVD grown a-SiN$_x$:H layers with varying stoichiometry controlled by the relative gas fluxes of NH_3 and SiH_4 used during growth. In the picture is possible to see the quasi Gaussian emission band shape as well as the peak energy blueshifts with increasing stoichiometry, represented by the increase in the relative amount of NH_3 flow in respect to SiH_4.

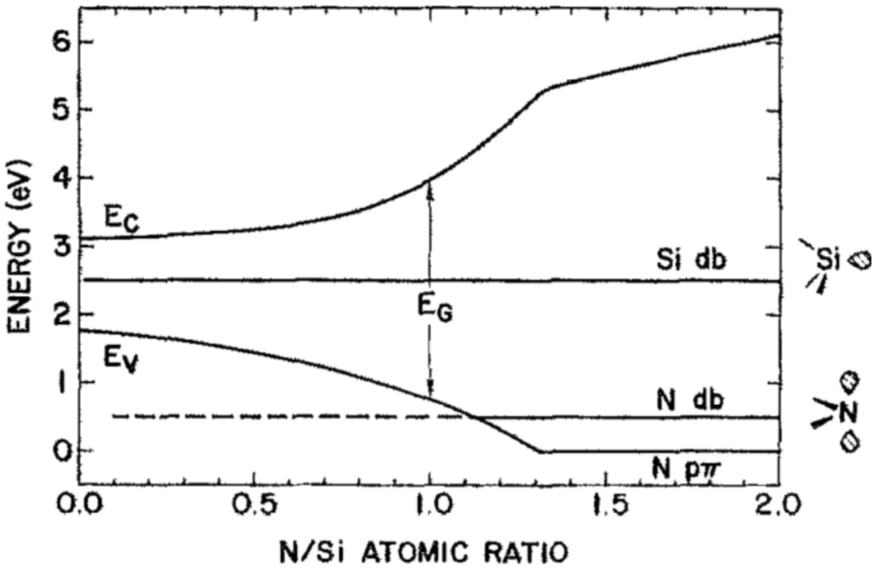

Figure 13: Band edge energies with N/Si ratio calculated for a-SiN_x:H thin films. From [74].

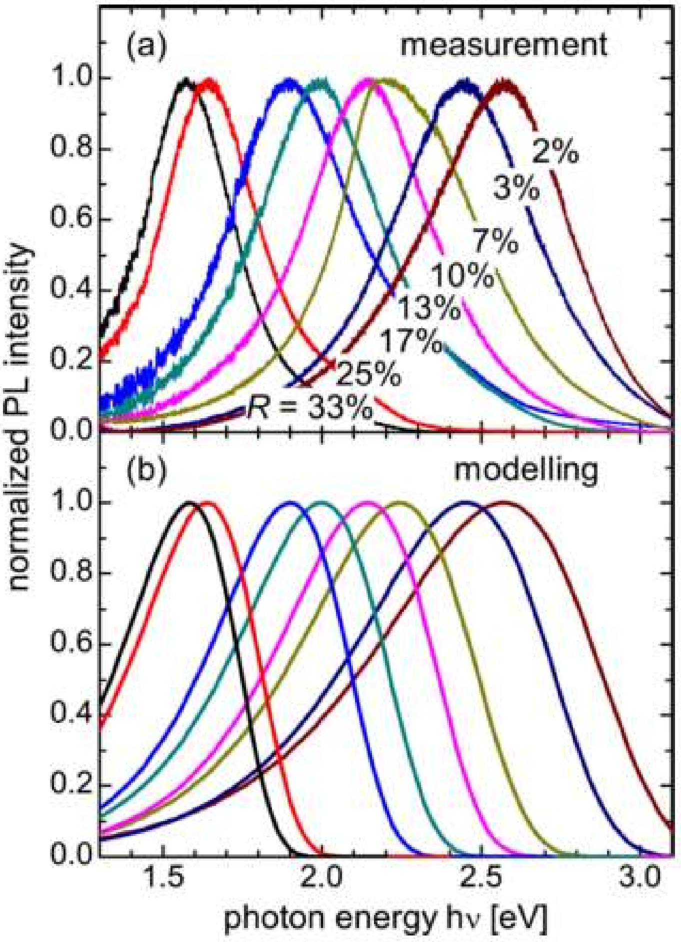

Figure 14: Normalized room temperature PL spectra of PECVD grown samples. R is the relative amount of SiH_4 in NH_3 flow used for growth. (a) Measured PL spectra for samples with different compositions and; (b) Predicted emission from the optical parameters using equation (19). From [128]

3.4 Defect Related Auger Excitation Model (DRAE)

Originally formulated for the explanation of the excitation mechanism of Er^{3+} ions in a-Si:H, the DRAE model [72] can be, in principle, applied to any rare earth ions in any Si based alloy host whose dangling bond energy is consistent with the transitions of the RE. For instance, it was used to describe the photoluminescence of Nd in a-SiN_x:H [40]. According to this model, a hole in the extended valence band is captured by a charged D^- defect, making it neutral (D^0). Followed by it, is the capture of an electron from the conduction band tail. The RE^{3+} ion is excited near resonantly from the matrix through an Auger process caused by the recombination of an electron with a hole in a neutral silicon dangling bond defect (D^0).

The mechanism is explained using adiabatic potentials in a general configurational-coordinate diagram, which basically represents, in one dimension, the change in distance between the erbium and its neighboring atoms – see Figure 15. It considers an electron-phonon interaction, i.e., local vibrations of the defect atoms.

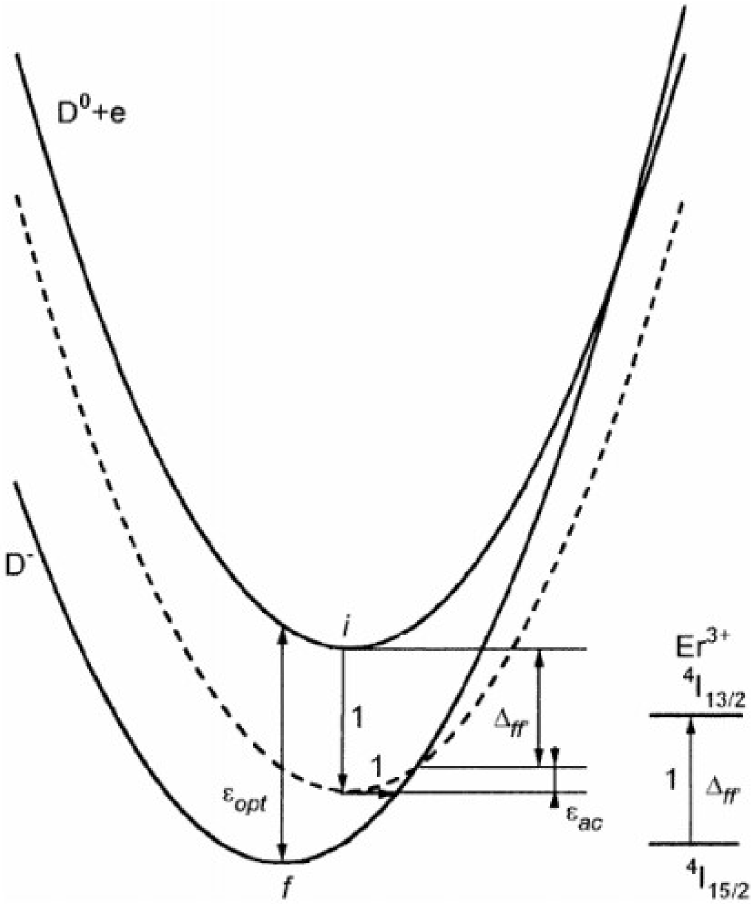

Figure 15: General configurational-coordinate diagram for the $D^0 + e \rightarrow D^-$ transition for the erbium case. The initial and final states are represented respectively by *i* and *f*. Dashed curve represents the intermediate virtual state (erbium excitation). Δ_{ff} is the energy for Er excitation. ε_{ac} the excitation energy (from [72]).

4 Sample Characterization Techniques

In this chapter, the characterization techniques used in this work will be presented with some considerations on their fundamentals. Each technique is presented by one section where the experimental setup and conditions will be described.

4.1 Rutherford Backscattering Spectroscopy (RBS)

RBS is based on the spectroscopy of α (He^+) particles, with well-defined energy, backscattered from a sample as a result of collisions with its constituent atoms. With RBS, it is possible to determine composition of the samples and also elemental concentration depth profiles.

During the collisions, energy is transferred from the incident particles to atoms of the studied material. The ratio at which the incident beam energy is reduced as a result of collisions with the film surface, often referred to as the K ratio (Equation 20), is a function of the ratio between incident's and target's atomic masses. The backscattering of RBS can be described by elastic, hard sphere collisions described by classical mechanics and the K ratio, between the incident energy (E_0) and the backscattered beam (E) is given by: [129]

$$K = \left[\frac{(1-(M_1/M_2)^2\sin^2\theta)^{1/2} + (M_1/M_2)\cos\theta}{1+M_1/M_2}\right]^2 \tag{20}$$

where M_1 is the mass of incident He^+ particles, M_2 the mass of the scattering atom and θ the scattering angle. Knowing the incident ion masses, it is possible to identify each element that composes the film.

When the incident ion moves through the film, it also loses energy by collisions with electrons inside the material. The energy loss is directly proportional to film depth so it is possible to associate the total energy loss with the depth at which the collision occurred.

The technique is very well adapted to heavy elements, as is the case of the elements of the Rare-Earth family. The differential cross-section can be written by [129]:

$$\frac{d\sigma}{d\Omega} = \left(\frac{Z_1Z_2e^2}{4E_0}\right)^2 \frac{1}{(\sin\theta/2)^4}$$

Thus, for heavier elements, the sensitivity of the technique can reach with reliability even for concentrations of less than 1 at.%.

One disadvantage of the technique, though, is its low sensitivity to H. The use of complementary techniques such as ERD (or Elastic Recoil Detection Analysis) or spectroscopy in the Infrared region can give a full determination of the a-SiN_x:H composition.

Basically, the RBS spectrum is a histogram where the abscissa is energy lost by the beam and the y-axis the number counts of the detector. The signal is calibrated in energy and incident beam intensity with well-known reference samples for each laboratory. The spectra are analyzed by iterative methods and software which allows RBS spectra simulation for a given composition of the studied sample. In fact, one of biggest advantages of RBS is low computational requirements for simulation of experimental results. The equations involved use only classical scattering of central forces [130]–[132].

Figure 16 shows a typical spectrum of our Tb doped a-SiN$_x$:H thin films. Measurements were done using 2.2 MeV α-particles. The spectra were all processed using the SIMNRA software [131], [133]. Since the low computation requirements, the data are usually treated iteratively where the user guess an approximate composition based on the accumulated experience he has. Once the model and the data are close enough it is possible use a Simplex method to adjust the model to the data.

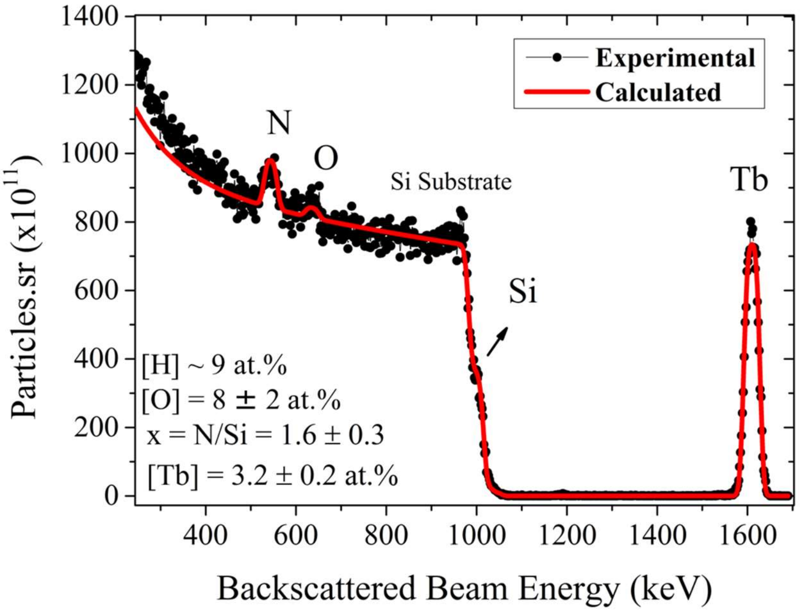

Figure 16: Typical RBS spectrum encountered in our Tb doped a-SiNx:H thin films on Si substrates.

The RBS measurements were conducted at two different laboratories. Samples grown by sputtering were measured at LAMFI (*Laboratório de Análises por Feixes Iônicos*) of University of São Paulo (USP). Samples grown by ECR CVD were measured at the Tandetron Accelerator Laboratory of the University of Western Ontario, Canada.

4.2 Atom Probe Tomography (APT)

Atom Probe Microscopy (APM) comprehends several nanostructures imaging and microanalysis techniques through field ionization, emission, and evaporation of particles from the studied material. APM offers an analytic map in three dimensions with atomic resolution and, as such, is capable to offer rich information about the structure and chemical composition of the sample [134].

Atom probe Tomography (APT – see Figure 17), more specifically, refers to the one that explores the field evaporation principle to remove atoms from a sample in a needle shape and their detection with composition reconstruction purpose atom per atom. Field evaporation process is achieved by very precise laser pulses which triggers the surface atoms from the needle which are then ejected and ionized. These electrons are then accelerated by an applied external electrical field towards a (X,Y) position detector. Once they hit the detector, the mass-charge ratio of the ejected particles is determined by a time-of-flight technique.

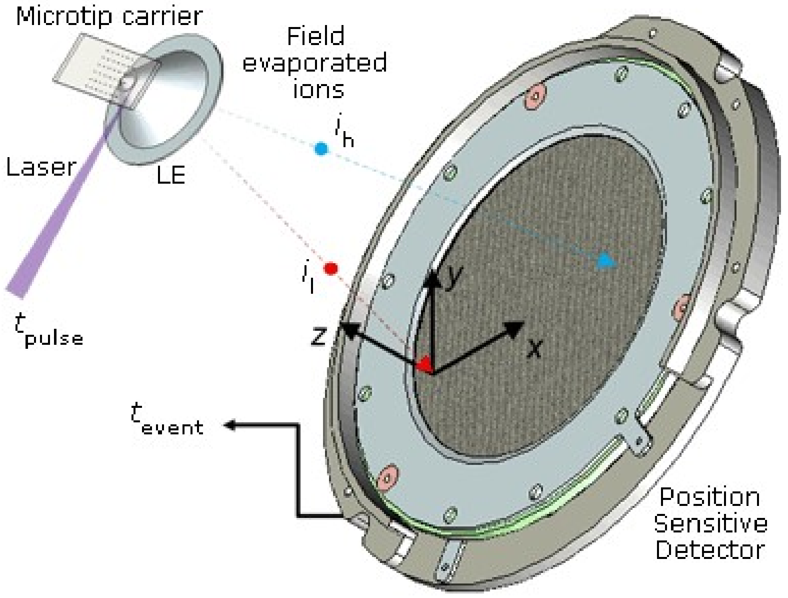

Figure 17: Schematic diagram of an APT system. (Adapted from <http://www.cameca.com/instruments-for-research/atom-probe.aspx>, access in 29/03/2016)

More specifically, a micro tip is electrically charged at high voltage (3-15 kV) right before the atom evaporation point. A high intensity laser is focused in the micro tip trigger, precisely in time, the evaporation process which allows a very precise time of light measurement between the beginning of the process and the arrival of the atom specimens at the position sensitive detector. Therefore, it is possible to determine the m/q ratio of the sample elements. The (X,Y) position is also determined which, together with some assumptions on the evaporation process, allows the lateral and depth reconstruction of the tip.

The atom reconstruction is done in two steps: first, the lateral coordinates, around the microtip, are determined and at second place their depth. Some approximations are often used for the reconstruction:

1) The evaporation occurs layer by layer, from outside in. The tip is approximated by a hemisphere or radius R which is altered as the material is evaporated. That can be measured through the penetration depth, d_p, of the electrical field, F, with a surface charge density, n_e, through the expression:

$$d_p = \frac{n_e}{F_{\varepsilon_0}}$$

typically, in the picometers scale.

2) The electrical field distribution is assumed to be uniform around the tip. Because the problem has cylindrical symmetry, that is, the ejected ions trajectories evaporated from the material are in the same plane defined by a specific value of the polar angle. Therefore, there is a direct relationship between the (x, y) coordinates of the atoms in the sample with the coordinates in the detector according to the equations:

$$x = \frac{X_D}{M_{proj}} \quad \text{and} \quad y = \frac{Y_D}{M_{proj}}$$

where,

$$M_{proj} = \frac{D}{d} = \frac{L + \xi R}{\xi R} \approx \frac{L}{\xi R}$$

is the magnification (Bas *et al.* protocol [135]) (see Figure 18). The ions trajectories are assumed to be straight lines defined by initial and final points to simplify calculations.

The tip radius determination, also shown in Figure 18, can be done through two distinct ways:

a) Through the applied difference in electrical potential, electrical field necessary for evaporation in the specified material and from the reduction field, k_f, also know as field factor – it reflects the studied tip shape and the electrostatic environment. The equation below gives the relationship:

$$R = \frac{V}{k_f F}$$

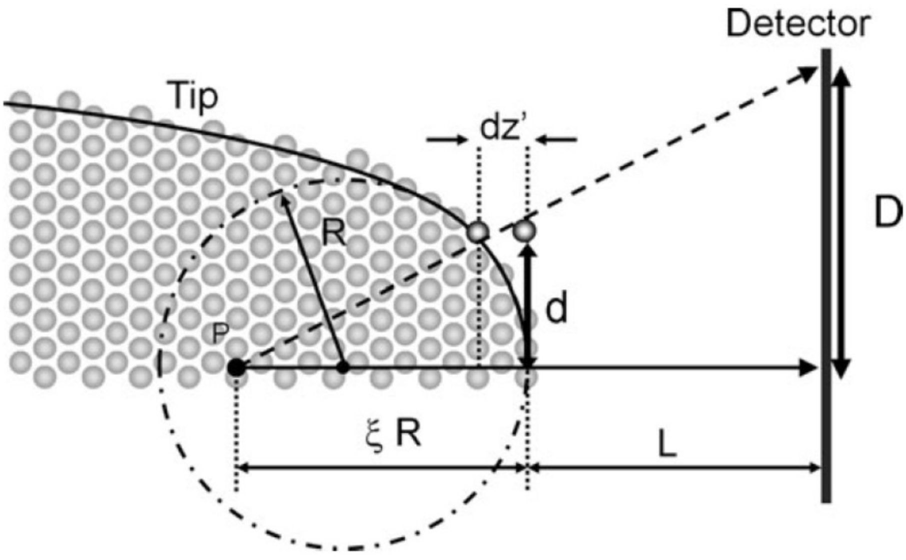

Figure 18: Geometric parameters used in atom reconstruction of the punctual projection model. In this model, the real atom paths are substituted by affective straight lines from their starting point at the surface up to the detected position. ξR is the reduction factor which gives the projection point onto the symmetry axis of the particle's trajectory. It reflects the electrical field strenght at the tip's surface.

b) Through sample's geometry. If the shape of the sample is known in details, given in terms of the inclination angle of the tangential line which connects the tip with the direction in which the needle grows, through the expression:

$$\frac{dR}{dz} = \varpi_R(z) = \frac{1 - \sin\alpha}{\sin\alpha}$$

The depth coordinate, z, can be determined considering the average atomic volume, Ω, and measuring the evaporated volume, $V_{evap} = n_{evap}\Omega$, in a sequential evaporation hypothesis, through the equations:

$$z_{tip}^{(i+1)} = z_{tip}^{(i)} + dz$$

$$dz = \frac{\Omega}{\eta\varpi_v(z)}$$

where η represents the fraction of actual detected atoms, represented by n_d, or $n_d = \eta n_{evap}$, and $\omega_v(z)$ is a function that describes the analyzed volume growth:

$$V_{evap} = \int_0^{z_{max}} \omega_v(z)dz$$

which can be estimated through many different protocols available:

Figure 19 and Figure 20 respectively show TEM images of sample preparation at different stages and the fabricated micro tip made with the use of a Focused Ion Beam.

Covering with Cr is necessary to enhance thermal and electrical properties of the microneedle for a better mass/charge spectrum. Figure 21 shows a graph of the results of the atom reconstruction for one sample grown by RF-Sputtering.

Figure 19: TEM images at different stages of the micro-needle preparation. Experiments conducted by Brian Langelier from CCEM.

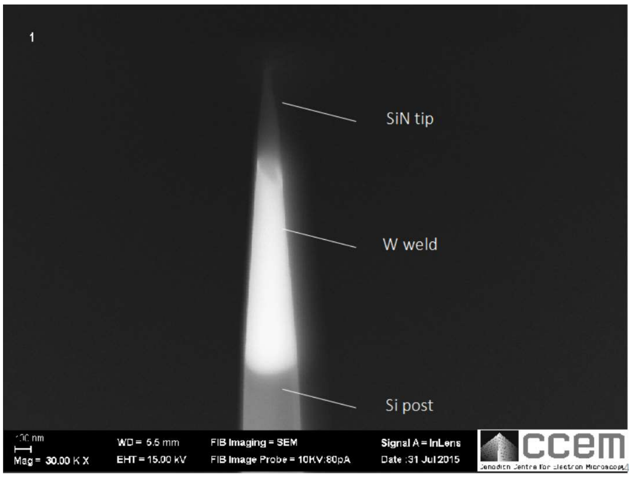

Figure 20: A TEM image of a micro-tip forged by a focused Ar$^+$ beam (30 kV). After being sharpened, the needles are coated by a Cr layer (15 nm of nominal thickness) to enhance thermal and electrical conductivities.

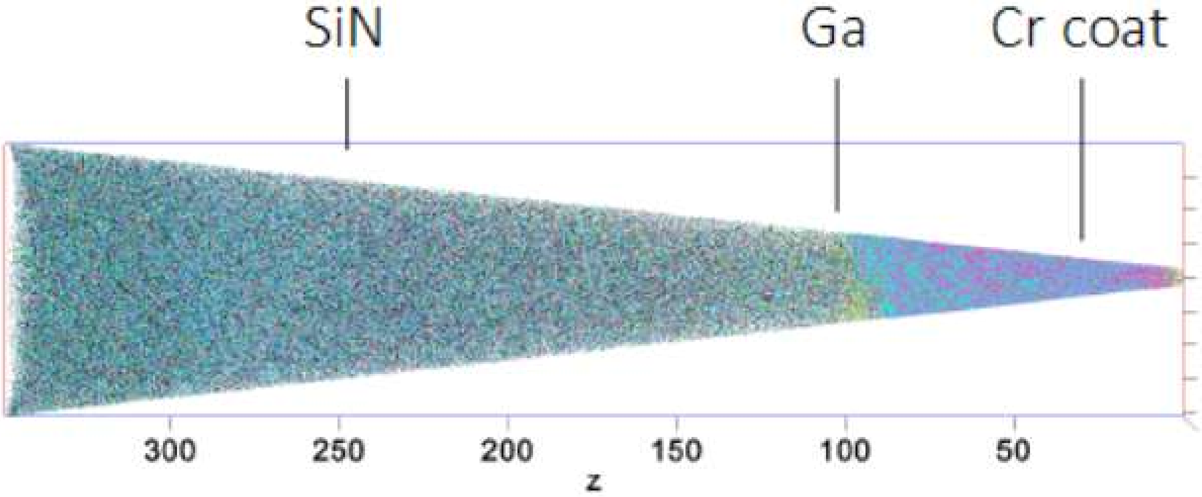

Figure 21: Two-dimensional view of a 3D atomic reconstruction from an APT measurement for a selected $a - SiN_x{:}H < Tb >$ sample grown by Sputtering. Each pixel represents an atomic element.

4.3 X-Ray Absorption Fine Structure (XAFS)

Information about the neighborhood around a Lanthanide ion can be obtained by X-Ray absorption fine spectroscopy (XAFS). XAFS uses the photoelectric effect and the wave nature of the electrons to gather this information. It consists on measuring the absorption coefficient up to a few hundred eV above an absorption edge from one of the core levels of the analyzed ions [136], [137]. As the photoelectron propagates from the core, the neighboring atoms partially reflect it – see Figure 22. The absorption spectrum contains very small oscillations (typically up to a few %) due to interference between the outgoing and reflected wavefunctions. The interference condition depends on the wavelength associated with the photoelectron which depends on its kinetic energy and is generally given in terms of the variable $\chi(E)$:

$$\chi(E) = \frac{\mu(E) - \mu_0(E)}{\Delta\,\mu_0}$$

where $\mu(E)$ represents the actual absorption coefficient and $\mu_0(E)$ the absorption coefficient of the isolated atom.

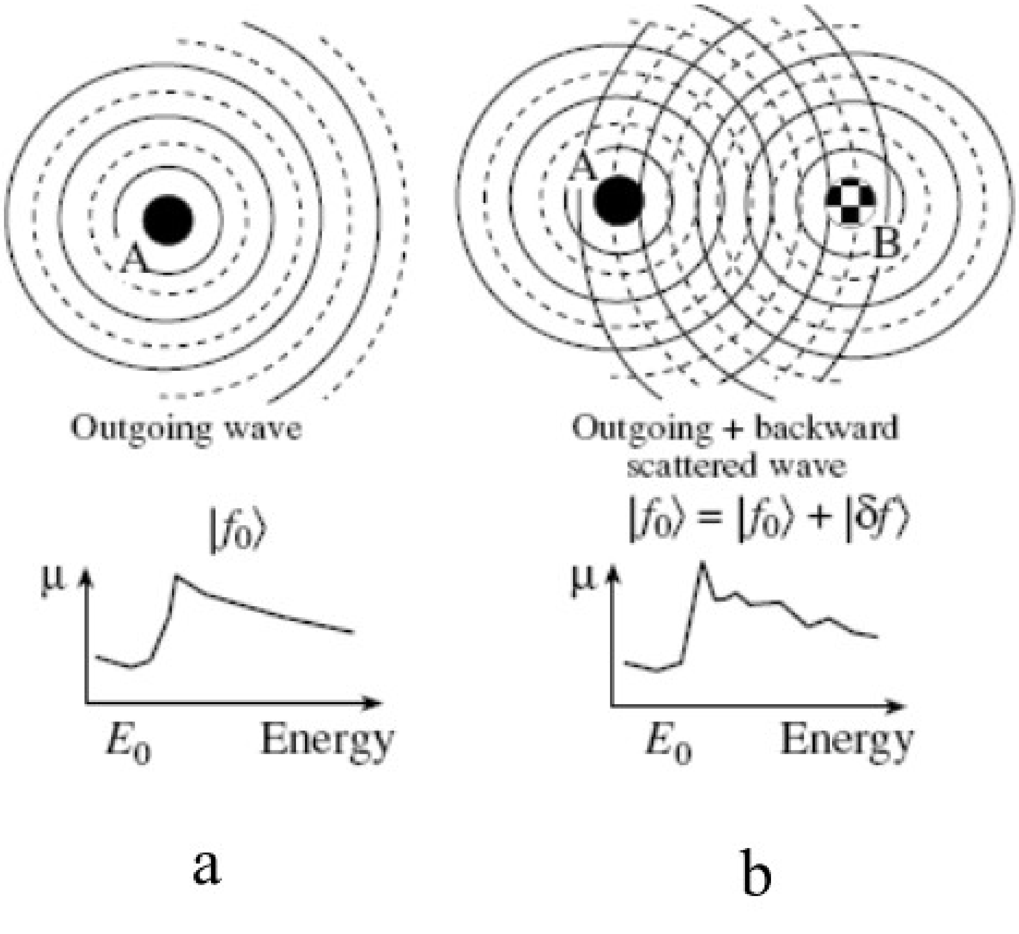

Figure 22: Schematics of the interference process that takes place in the EXAFS phenomenon. From [138]

The absorption spectrum at low energies, or next to the edge, is referred to as XANES (X-ray Absorption Near Edge Structure) and may contain sharp peaks (often referred to as white line) when the electronic X-ray absorbing transition is allowed, or involves quantum states of opposite parity. The white lines have information about the ionization state of the absorbing atom. In the first tens of eV above the absorption edge (long photoelectron wavelengths) the oscillations are dominated by multiple scattering which makes structural information determination very tricky. For higher photoelectron energies (shorter photoelectron wavelengths) the neighboring atoms behave as point obstacles and contribute each with a tiny wavelet in the so-called EXAFS (Extended X-Ray Absorption Fine Structure). Understanding the interference is straightforward. Fourier analysis yields for each neighbor sphere parameters such as average coordination, interatomic distances, and a radial disorder parameter (the Debye-Waller Factor).

Since the Tb concentration is of a few at.% in films of thicknesses ranging around 500 nm, the fluorescence mode of absorption measurement was employed rather than transmission. The films were measured at grazing exit limit, with $\varphi \rightarrow 0$ in a right-angle configuration (between the incident beam and the fluorescence detector) – see Figure 23. With this configuration, elastic scattering of the incident beam by from the sample is greatly suppressed and self-absorption effects become negligible. In this situation, the absorption coefficient can be approximated to the expression:

$$\mu(E) \propto \frac{I_f}{I_0}$$

It is interesting to clarify the meaning of *self-absorption* here. It is not the absorption of the fluoresced X-rays from the sample itself. The term, in the XAFS jargon, usually means the damping in the XAFS signal caused by absorption of the element of interest. The worst case is represented by a material composed purely of the element being under study. XAFS signal changes the penetration depth of the X-rays but, essentially, the escape depth of the fluoresced X-rays is much longer. Consequently, all absorbed X-rays generate one fluoresced X-ray, damping severely the XAFS signal. [139], [140]

To attenuate the elastically scattered beam, a filter, consisting of a slab of Mn, was placed between the sample and the detector. A collection of slits, referred to as Soller slits, are placed in the entrance of the detector to avoid the light emitted back from the filter itself.

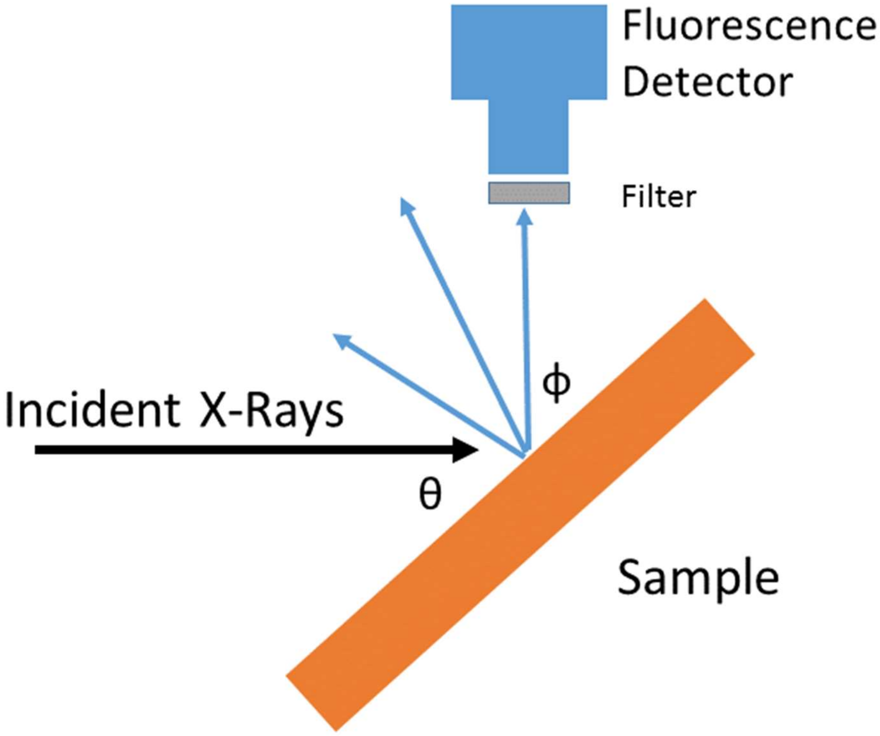

Figure 23: Fluorescence x-ray absorption measurement configuration: adopted for XAFS data collection of Tb doped a-SiN_x:H thin films. The X-rays generated by the synchrotron source are monochromatized by a rotating Si crystal and then focused in the sample, oriented with an angle θ, with respect to the incident beam. The detector is placed at an angle φ, between the fluoresced X-ray and sample surface.

XAFS is normally measured in synchrotron light sources because of the possibility of easily obtaining intense tunable monochromatic X-rays. The present EXAFS measurements of this work were taken at the D08B – XAFS2 line in *Laboratório Nacional de Luz Síncrotron* (LNLS) at Campinas–SP, Brazil). X-ray absorption at the L_{III} edge of Tb^{3+} element, approximately at 7530 eV, was measured monitoring the $L\alpha_1$ fluorescence line in the thin film samples and by transmission in the reference oxides – in this case, the absorption coeeficient is measured by $\mu(E) = -\ln(I/I_0)/t$, where t and I stand for the thickness of the prepared reference material and the transmitted beam intensity, respectively. Acquisition time for each spectrum was typically one hour long. Fluorescence was measured by a 15 element Si(Li) detector.

Figure 24 show one typical absorption spectrum, $\mu(E)$, obtained through fluorescence, of the Tb^{3+}'s L_{III} absorption edge.

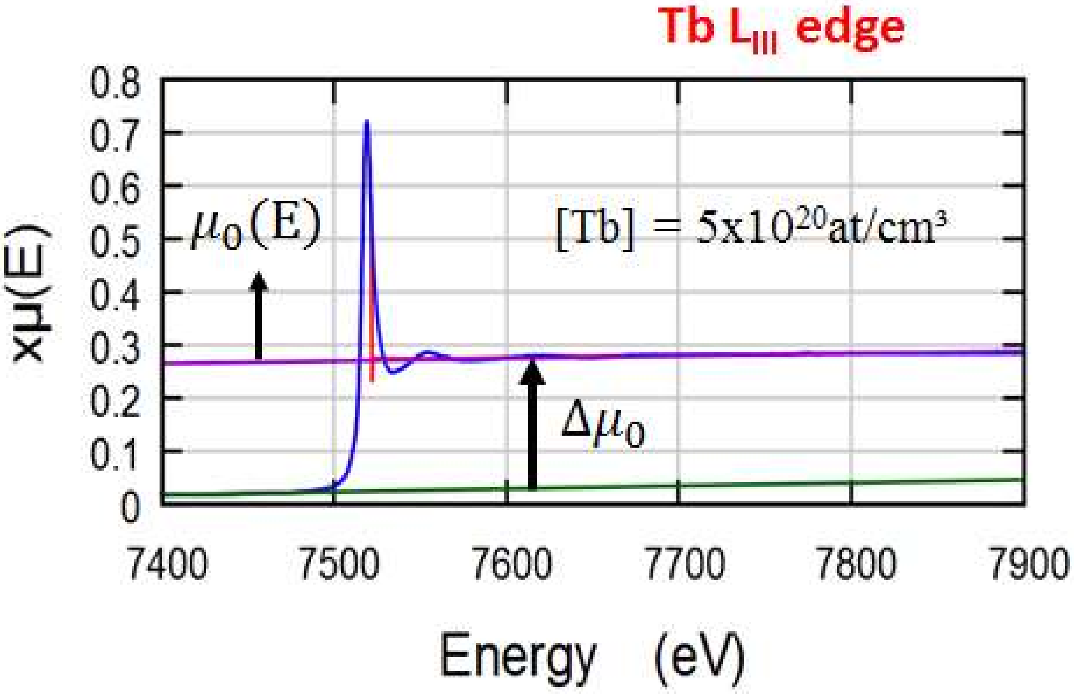

Figure 24: "White line" corresponding to the Tb^{3+} L$_{III}$ absorption edge obtained from one of our sputtered grown films. Some oscillations in the absorption spectrum, which corresponds to the EXAFS signal, are visible between 7550 and 7700 eV. The combination of RBS and VASE results were used to determine Tb concentration in this sample. It represents the Tb's area density, given by RBS divided by the thickness obtained by VASE.

4.4 Fourier Transform Infrared Spectroscopy (FTIR)

One of the advantages of FTIR is the possibility of an easy and direct characterization of bonded H to Si and N. The estimation of bonded H present in films is done through the measurement of the spectral absorption coefficient of the Si–H and N–H stretching vibration modes at ~2150 and ~3350 cm^{-1}, respectively – see Figure 25. One of the proposed methods was given by Lanford and Rand [141]. They used nuclear techniques involving the direct count of hydrogen atoms bonded to Si and N in a series of a-SiN$_x$:H films with different concentration of H. In doing so they could establish the calibration constants, given in eq. 21, for the FTIR signal for the to the before mentioned absorption peaks.

$$H/_{cm^2} = 1.36 \times 10^{17} \times (1.4\, area\ N - H + area\ Si - H) \qquad (21)$$

where *area* is the integral of the absorption coefficient, obtained from transmission measurements, of the two peaks, i.e., $\int A(\nu)\, d\nu$, where ν is the wavenumber (cm^{-1}) and $A = \log(I/I_0)$ is the absorbance.

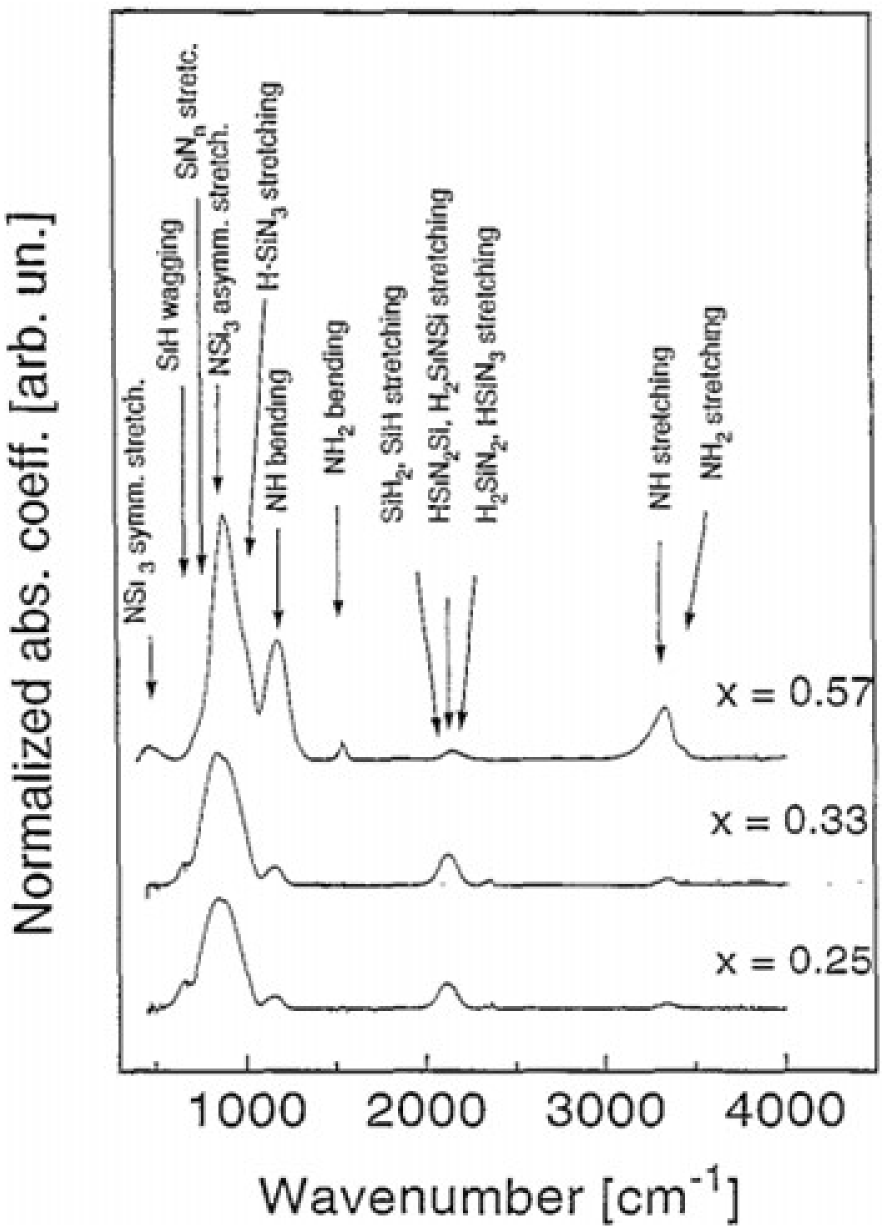

Figure 25 - Infrared absorption peaks typical in hydrogenated amorphous silicon nitride thin films for different stoichiometries and their relationships with vibration modes between Si, N and H bonds. The “x” shown here refers to an alternative formula used for nitrides: $a\text{-}Si_{1-x}N_x:H$.. From [127]

With bonded H information in the films, and consequently their density, since the films’ thicknesses were determined by VASE, it is possible to correlate them with Tb^{3+} PL behavior and find signs and evidence of the mechanisms behind terbium sensitization.

Infrared measurements were taken in a modified Bruker Vertex 80v FTIR. The source used was a piece of heated globar for using a KBr beam splitter and detected by a liquid nitrogen cooled Digitect InSb detector.

4.5 Variable Angle Spectroscopic Ellipsometry (VASE)

Ellipsometry is a non-destructive optical technique specially designed for thin films. It directly measures the change in the polarization state of light caused by reflection from the analyzed sample. Based on some assumptions and models used to fit the experimental data, it can determine the optical constants and film's thickness among other properties. The change in the polarization state of light (see Figure 26) is described in terms of the Ψ and Δ parameters, that represent the amplitude and phase change, defined by:

$$\tan(\psi) \cdot e^{i\Delta} = \rho = \frac{r_p}{r_s}$$

where r_p and r_s are the Fresnel reflection coefficients for parallel and normal components with the incidence plane, respectively, which are directly related to the real and imaginary parts of the refraction index of the studied film.

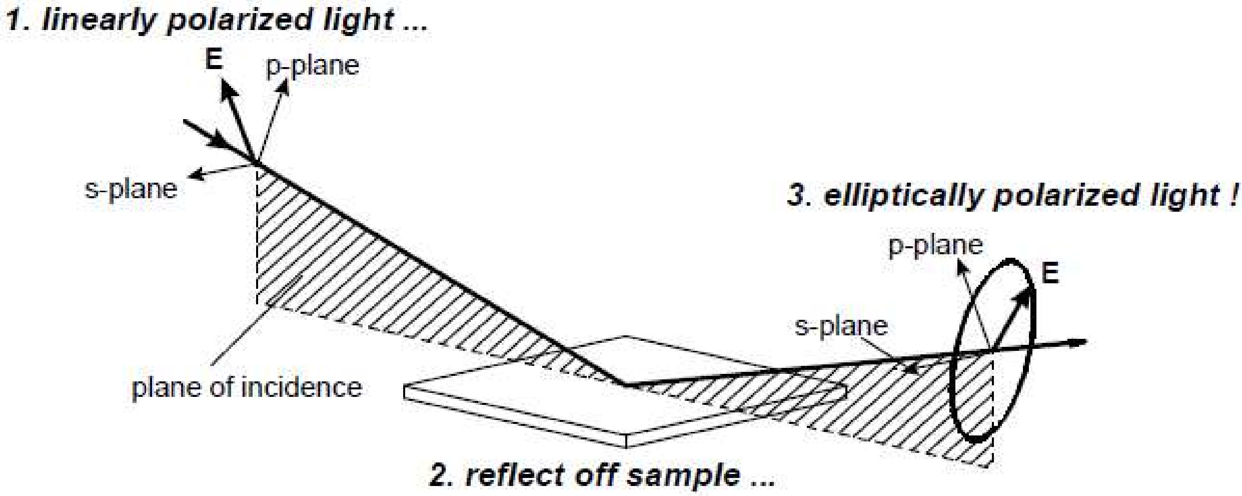

Figure 26: Illustration of the basic principle used in ellipsometric measurements evidencing the s and p components of the electric field. A linearly polarized monochromatic light beam is shined upon a reflective surface. The elliptically polarized light beam reflected goes to a detector where each polarization component is measured.

Common ellipsometers use the HeNe laser as a light source but one technique that has become increasingly available is the Spectroscopic Ellipsometer where the Ψ and Δ parameters are measured as a function of wavelength of the incident light beam. To get more data, so more reliable results, some available ellipsometry systems are designed to even measure several different reflection angles. These systems are referred to as Variable Angle Spectroscopic Ellipsometers (VASE).

Compared to a simple intensity transmission, reflection, or absorption measurements, ellipsometers double the information content in a single shot since it measures independently two different parameters. VASE is very sensitive in thickness determination.

Particularly because of the Δ parameter in which the discontinuities in their dispersion relations are very sensitive to film's thickness.

Because it measures the polarization change due to reflection, VASE allows for optical measurements using substrates that absorb at the wavelengths used.

A VASE M-2000 ellipsometer (from J.A. Woollam) operating in the wavelength 240–1700 nm range (or UV-VIS-NIR wavelength range) was used to determine the optical constants and thicknesses of the films – Figure 27 depicts a photograph of the system that is available in the optics lab of the Department of Engineering Physics at McMaster University.

Similarly to RBS data, VASE data (see Figure 28 and Figure 29) are treated using some assumptions and models well know from the literature used for fitting. This data analysis was performed using the ellipsometry software: CompleteEase™. The software has a built-in database where it is possible to construct a model of the system under study. Based on the model assumptions, the software can calculate the produced Ψ and Δ parameters as a function of the wavelength and directly compare it with the measurements.

For whole set of the a-SiN_x:H<Tb> films studied in this work, the Cauchy and Urbach dispersion models were very well suited for fitting of the experimental data points. These dispersion relations are written as [142], [143]:

$$\begin{aligned} n(\lambda) &= A + \frac{B}{\lambda^2} + \frac{C}{\lambda^4} \\ k(E) &= k_0 \exp[(E - \overline{E}\,)/E_0] \end{aligned} \tag{22}$$

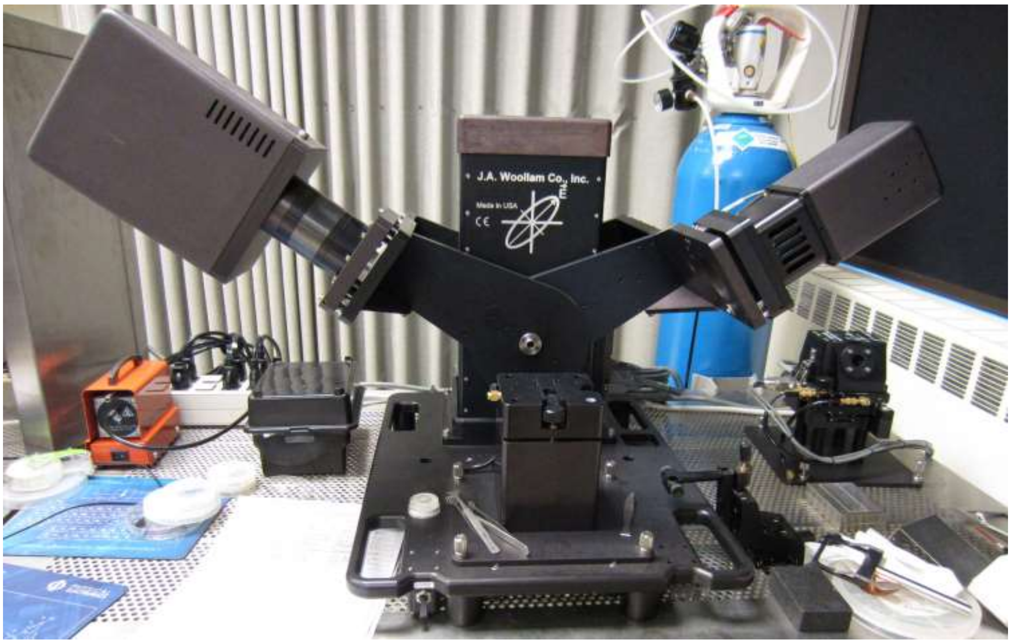

Figure 27: Photograph of the J.A. Woolam's VASE instrument used for this work. Photograph taken by P.R.J. Wilson.

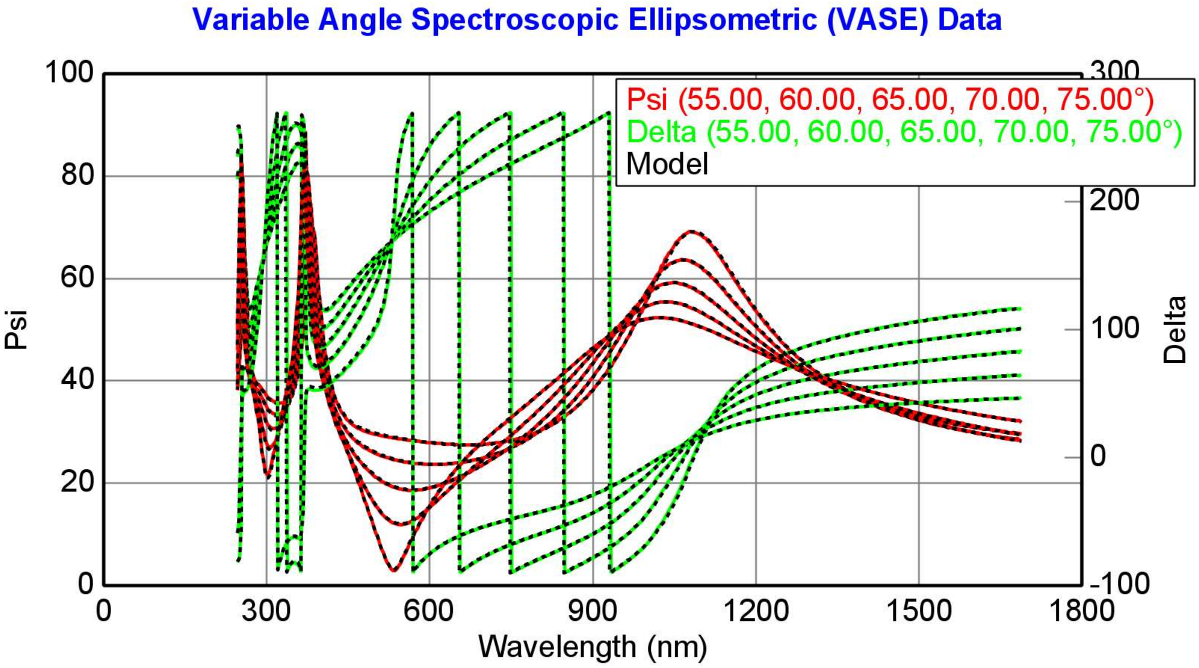

Figure 28: Typical VASE spectra found in Tb doped a-SiN$_{1.5}$:H films. The Ψ and Δ parameters are measured for 5 different reflection angles, described in the inset of the picture. The red curves represent Ψ while the green ones represent Δ . The sample shown has thickness of 177 ± 1 nm and n(λ = 632,8 nm) = 1,76.

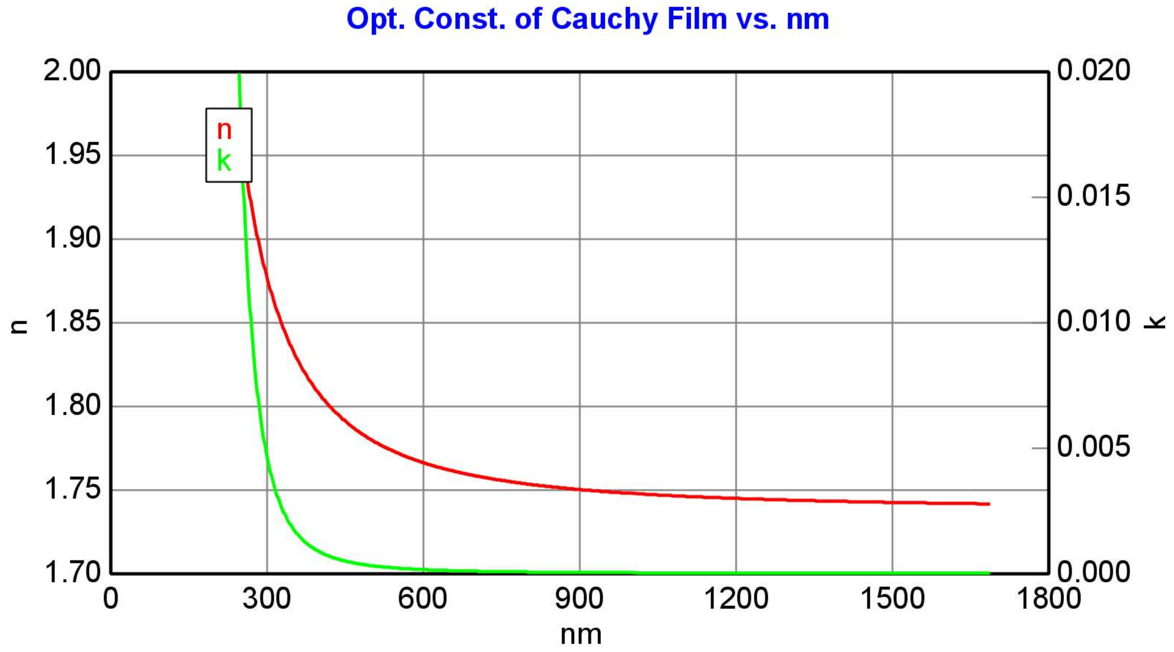

Figure 29: Dispersion relations for the complex refraction index. The Cauchy parameters are: A = 1,738, B = 0,0092 nm² e C = 2,9x10^{-4} nm [133]. The imaginary part, given by an Urbach relation has as parameters: k_0 = 8,82 x10^{-3}, E_0^{-1} = 1,61 eV and $\overline{E}$ = 3.1 eV.

4.6 Photoluminescence Spectroscopy (PL)

When light hits a solid sample, part of it is absorbed and promotes carriers to excited states. One way this excess energy gets dissipated is through the re-emission of light, or photoluminescence. PL spectroscopy is a non-destructive method to access information of the electronic structure of a solid material under study. It measures the spectral composition of this re-emitted light. From this experiment, important information of the electronic structure of the studied material can be obtained.

The current understanding of the recombination and photoluminescence processes and mechanisms in a-Si based materials was already presented in section 3.2.3 followed by a description of the electronic structure specific for a-SiN_x:H (section 3.3) and the DRAE model for Er^{3+} excitation (section 3.4) in a-Si:H. This section will be focused in the description of the PL spectroscopy experimental setups used for room temperature visible emission characterization of the Tb doped a-SiN_x:H thin films.

The visible emission of the films was characterized through room temperature ultraviolet and visible-excited PL experiments using three laser excitation sources: a 325 nm (3.82 eV) HeCd laser, a 375 nm (3.31 eV) diode laser and the 488 nm (2.54 eV) line of an Ar^+ laser. Two PL characterization systems were used. One for the 325 nm excitation, located at the Department of Engineering Physics, in McMaster University, and another, for characterizations in 375 and 488 nm excitation, located at *Departamento de Física Aplicada*, in Unicamp.

For both systems, appropriate color filters were applied to avoid laser signal in the spectra. The laser beam was directed onto a sample holder using free space optics and the PL was collected by two different systems:

- For 325 nm excitation: a lens which coupled the light into a fiber optic cable that was connected to an Ocean Optics S2000 visible charge-coupled device (CCD) spectrometer – see Figure 30.
- For 375 and 488 nm excitations: luminescence was collected using f/1 optics, dispersed by a 500mm f/4 SPEX spectrograph, and detected by a Princeton Instruments ST121 1340 column back illuminated liquid nitrogen cooled Si CCD – see Figure 31.

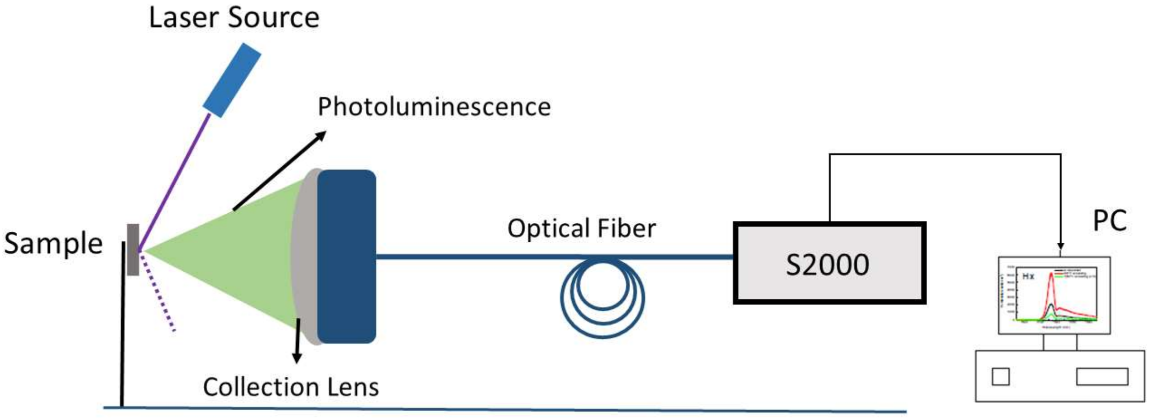

Figure 30: Photoluminescence spectroscopy experiment schematics used for HeCd 325 nm laser excitation used at Dept. of Engineering Physics in McMaster University (Canada). The photoluminescence light is collected by a lens that is coupled to an optical fiber that delivers the light to the spectrometer S2000.

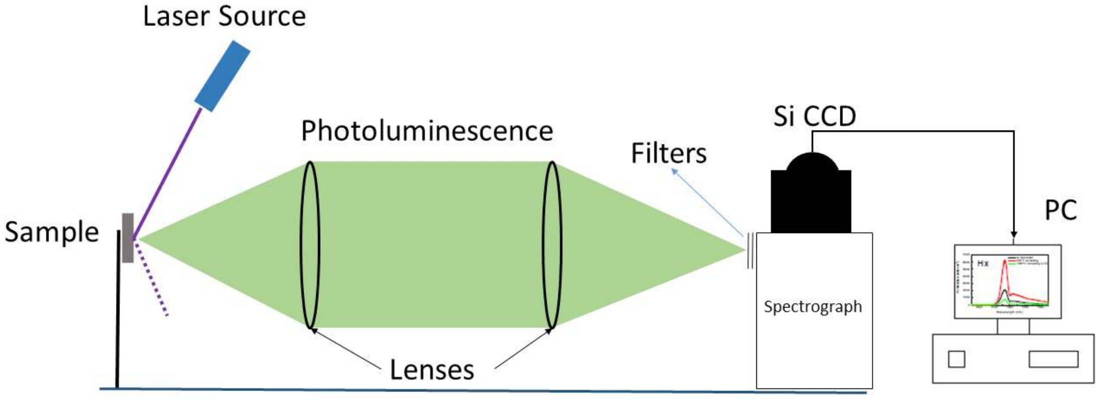

Figure 31: Photoluminescence spectroscopy experiment schematics used for 375 (diode laser, model nº L375P20K01.A02) and Ar^+ 488 nm laser line excitation sources. Measurements were taken at Unicamp (Brazil). The photoluminescence is focused directly to the spectrograph through free space optics. The detector is a liquid nitrogen cooled Si CCD.

5 Sample Preparation

Samples were prepared using two techniques: reactive RF-Sputtering and ECR-PECVD. This section reviews some of the main aspects of the two deposition techniques and describes the conditions and protocols used for sample preparation. Some characteristics (such as thicknesses, optical parameters, and chemical composition) of the a-SiN_x:H films are presented in function of the deposition parameters used for each deposition method.

5.1 Reactive RF-Sputtering

Sputtering is a thin film fabrication process which consists in the vaporization of a solid material, the “target”, by the transfer of momentum from accelerated positive ions that compose a plasma. There are at least two very commonly used sputtering setups: ion beam and glow discharge. The main difference is the source of the accelerated ions. For the glow discharge setup, shown in Figure 32, a parallel-plate configuration is commonly employed. Moreover, the ions are accelerated out of the plasma by a voltage drop between the two electrodes, so the ions impinge perpendicularly on the target. To prevent target charge build up in insulator targets, a radio frequency power (RF) is also used [144] .

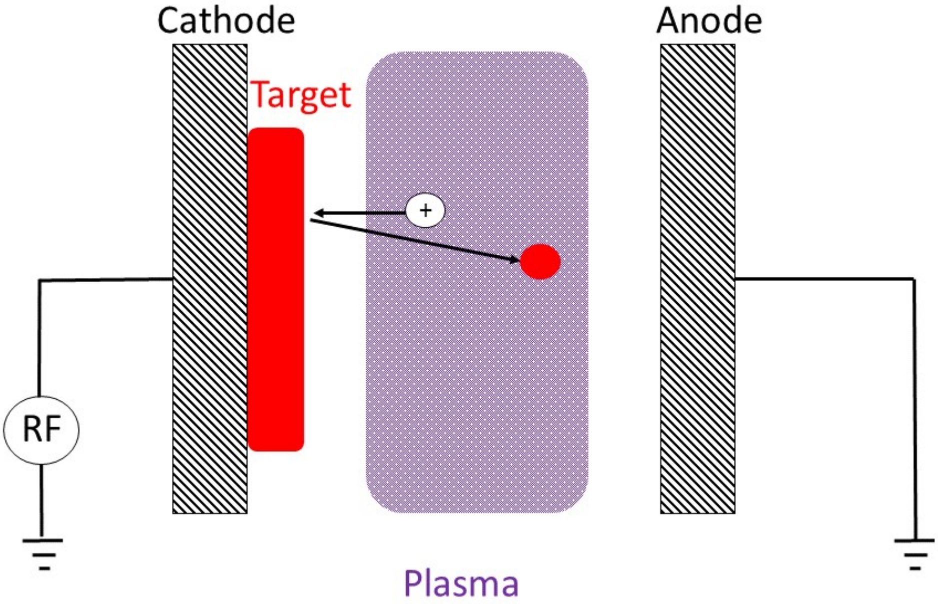

Figure 32: Schematics of a glow discharge setup using a parallel-plate configuration for plasma generation in a RF-Sputtering system used at the LPF in IFGW/Unicamp. Adapted from [144]

High vacuum, of the order of 10^{-6} mbar – or, approximately, 7.5×10^{-4} mtorr – is mandatory before deposition. Since the plasma is a very reactive medium, it is important that the chamber where the process takes place is sufficiently clean to avoid contamination by undesired elements.

The reactive RF-sputtering system present at *Laboratório de Pesquisas Fotovoltaicas* – LPF – is a modified commercial Leybold Z400 and is schematically shown in Figure 33. It consists of a 20 *l* chamber with an impedance matched RF source. Linked to the chamber is a series of gas lines controlled with needle valves and a mass flow controllers. The system is pumped by a 400 *l*/min turbomolecular pump roughed by a dry mechanical pump. Two independent sensors measure the pressure: an absolute capacitive membrane MKS Baratron 270 B, and a Balzers IMG 060 B Ion Gauge. The Target and substrates (composed of Czochralsk Si single crystal wafer pieces) are positioned inside the chamber respectively at the cathode and the anode. The substrates can be heated to temperatures up to 300ºC measured by a chromel-alumel thermocouple.

The procedure adopted for the RF-Sputtering deposition of a-SiN_x:H films was the following: with the chamber fully opened, the substrates were positioned in the substrate holder (grounded anode) at the top of the chamber as schematically shown in Figure 33, the target (75 mm diameter metallic disk of 99.999% pure Si) was then placed at the cathode; Tb_4O_7 (99.9%) powder tablets were placed above the target where they were properly covered with float zone Si wafer pieces to prevent target contamination – see Figure 34; the chamber was then closed and pumped down to a base pressure of 3.0×10^{-6} mbar or less.

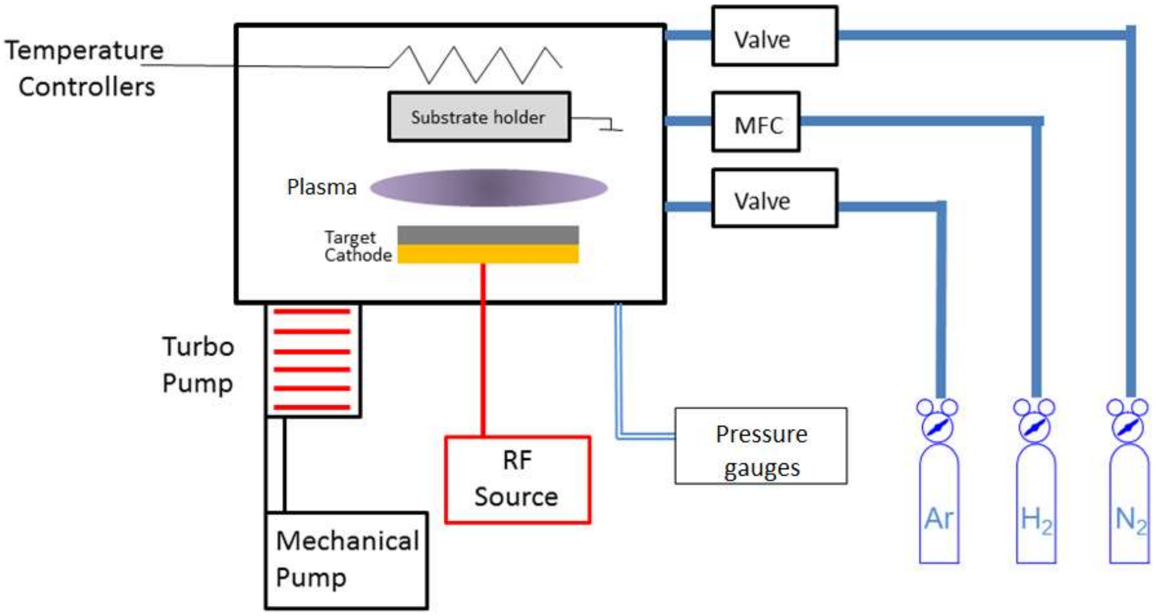

Figure 33: Schematic drawing of the RF-Sputtering system used for depositions of nitrogen-rich a-SiNx:H at LPF in University of Campinas. Adapted from [145].

Once the base pressure was established, Ar gas was introduced in the chamber while the RF source was on. Ar gas pressure was then increased until plasma breakdown. Ar gas pressure is then maintained to a constant pressure of 8.0×10^{-3} mbar and a self-bias of -1 kV was applied to the target and maintained for at least half an hour – in this moment the substrates were placed in another region of the chamber where there was no plasma, which stayed confined between the two electrodes. This procedure is what I will call from now on as "pre-sputtering" and was repeated every time the chamber is closed for deposition.

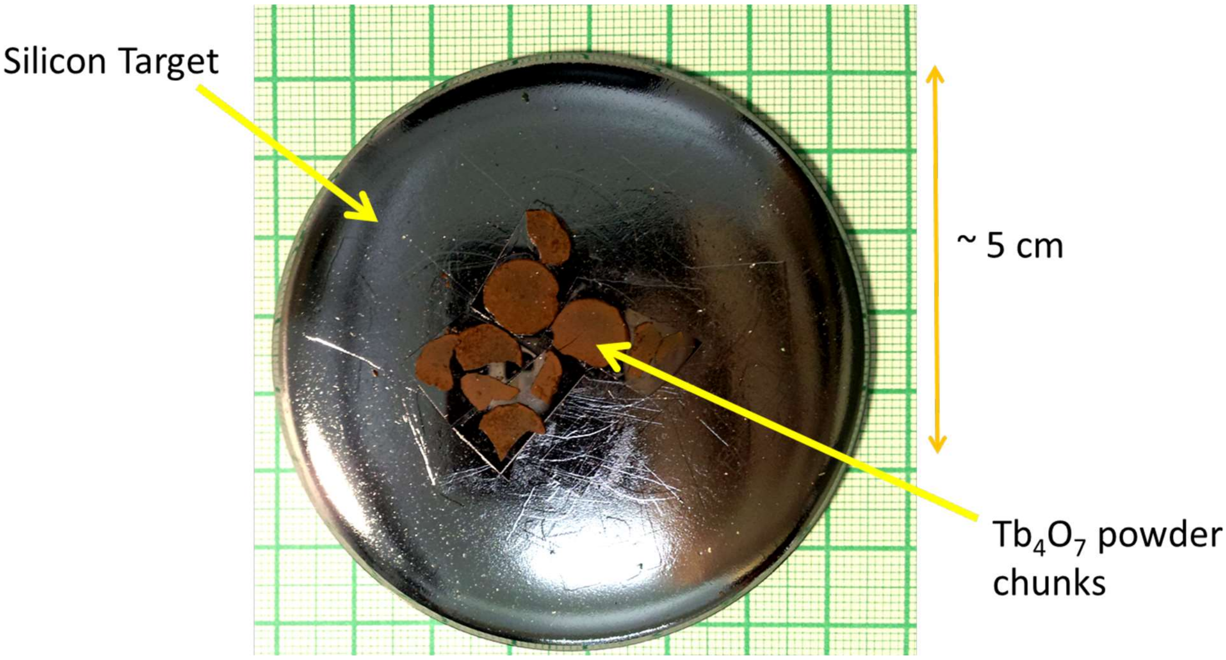

Figure 34: Sputtering target configuration with Tb_4O_7 compressed powder tablets for Tb incorporation in the nitrides. Even though the work was intended to study Tb in nitrides, the option to work with the Tb_4O_7 was taken due to two reasons: a) even if we worked with pure metal precursors, contamination with oxygen from the air would always appear in the samples since the metals from the lanthanide family are very reactive to O_2; b) Tb_4O_7 was readily available.

After the pre-sputtering procedures, the reaction chamber was again evacuated and the deposition process started. The heated substrates were moved directly above the Si target and a N_2 gas flow, 99.999%, was introduced and controlled by a needle valve. N_2 gas partial pressure was set to pressures around 2.0×10^{-3} mbar using the Ion Gauge controller. The offset for the capacitive membrane gauge was then calibrated and used for monitoring the reaction chamber pressure for the rest of the deposition. The Ion Gauge is then turned off. H_2 and Ar, also 99.999%, introduced. They are respectively controlled by a MFC controller and a needle valve. After the system pressure was stabilized, the RF source was ignited and the plasma generated. The plasma ignition used the same procedure for the pre-sputtering phase: a momentary pressure raise in Ar pressure until plasma breakdown. Table IV shows all the parameters kept constant for all samples grown by Sputtering depositions. All the deposition parameters used for the fabrication of the samples using reactive RF-Sputtering are in Appendix I.

Isochronal 1h annealing was performed in a quartz tube under positive N_2 gas pressure within 300 – 1200ºC range. A pre-annealing procedure was adopted to avoid film deterioration due to the presence of micro bubbles of Ar and H_2. It consisted of an annealing of 1h at 200ºC as a step before the films receive another thermal treatment at higher temperatures.

Table IV: Constant parameters during reactive RF-Sputtering depositions.

Total pressure (mbar)	8.0×10^{-3}
Bias (V)	-1000
Substrate temperature (ºC)	250
Deposition time (min)	120
Base pressure (mbar)	$< 3.0\times10^{-6}$

5.1.1 Deposition Rate, Chemical Composition, and E_{04} Energy Gap

The films grown by sputtering presented a distribution of thicknesses that ranged from 800 to 350 nm as the N_2 partial pressure (P_{N2}) in the sputtering gas composition was raised from 0.8×10^{-3} to 6.0×10^{-3} mbar. This corresponds to deposition rates ranging from 6.7 nm/min down to 2.9 nm/min, respectively. The variation in the deposition rate is due to the reduction of the average mass of the gas atoms resulting in a lower sputtering yield. For films deposited with of 2.0×10^{-3} mbar N_2 partial pressure, used in most of the depositions, the thickness was around 650 nm (~ 5.4 nm/min) within a window less than 10% of this value depending on other deposition conditions that were varied, such as H_2 gas flow and target coverage by Tb_4O_7.

The nitrogen to silicon ratio, x, of a-SiN_x:H layers strongly depends on the gas composition inside the reaction chamber [146]–[148]. A quantitative chemical composition characterization given by RBS is shown Figure 35. In this Figure, N to Si ratios is given as a function of the N_2 partial pressure in the reaction chamber used for each deposition. The N incorporation increases monotonically up to 5.0×10^{-3} mbar and seems to slightly decrease above it, as shown at 6.0×10^{-3} mbar. As pointed out by Signore *et al.* (2012) [148], Ar gas flux is the responsible for N_2 dissociation and ionization, so a concentration decrease of nitrogen active species, N_2^+ and N^+, is expected at higher P_{N2}, when the relative amount of N_2 to Ar is bigger. So, if the N_2 content in the chamber is too high, as evidenced at 6.0×10^{-3} mbar point, less active species available to react with Si are expected, and thus a decrease in stoichiometry is obtained.

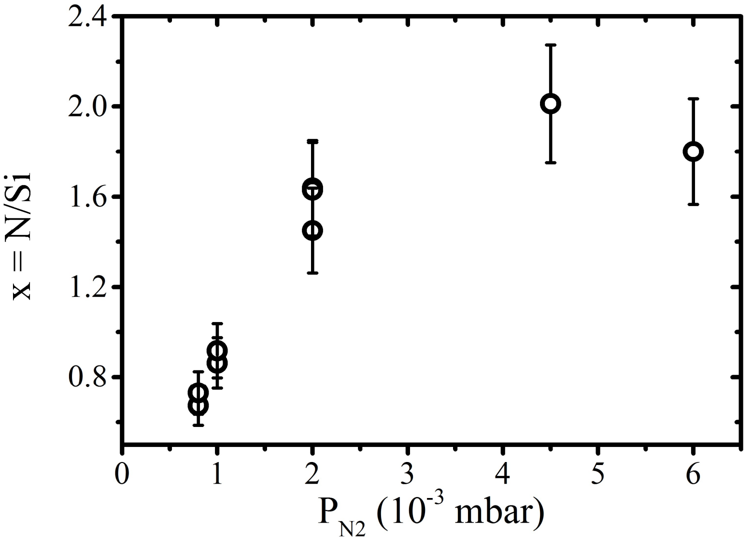

Figure 35: Stoichiometry of the films, $x = N/Si$, as a function of the partial pressure of N_2 (P_{N2}) in the chamber. The films shown here were prepared keeping the H_2 gas flow constant at 2.3 sccm. The total pressure in the chamber was kept constant at 8.0×10^{-3} mbar.

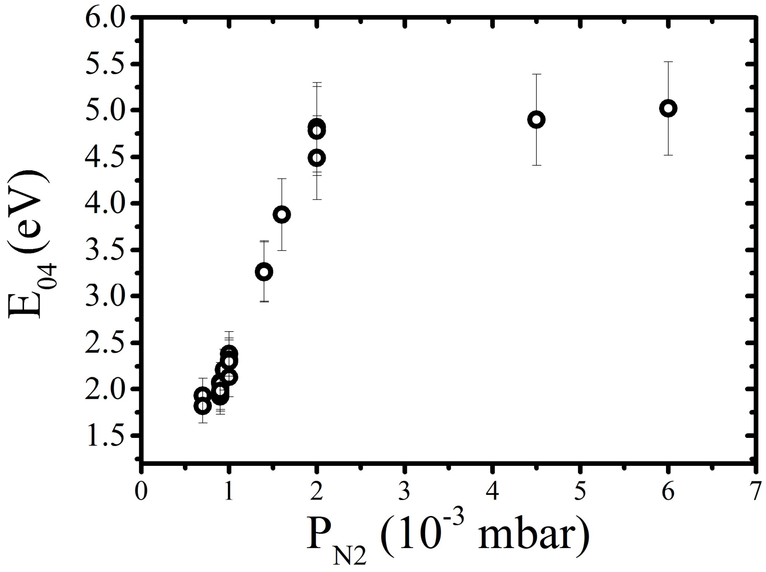

Figure 36: E_{04} optical gap for the reactive RF-Sputtering system as a function of the N_2 partial pressure.

The E_{04} optical gap can be very easily controlled and is very sensitive to the N_2 gas partial pressure in the chamber. The introduction of nitrogen atoms replaces less energetic Si-Si energy levels by more energetic Si-N ones (see Table III) thus increasing the energy separation between bonding and antibonding states and, consequently, the optical bandgap. Figure 36 shows the characterization of the E_{04} gap for some of the reactive RF-Sputtering grown samples. E_{04} increases from a-Si:H bandgap, around 1.8 eV when no N_2 is introduced, up to the stoichiometric films' gap, around 5.3 eV when the gas partial pressure N_2 (P_{N2}) is 2.0×10^{-3} mbar. According to Figure 35, this corresponds to $x \approx 1.6 \pm 0.2$, well beyond the stoichiometric silicon nitride value of 1.33. This is a well-documented result and happens because of the presence of N-H bonds [74], not present in Si_3N_4, which raises the necessary amount of N for stoichiometric energy bandgap.

RBS measurements also revealed the effect of the H_2 flux variation and the area coverage by Tb_4O_7 onto Si and N incorporation - Figure 37. The more H_2 in the forming plasma gas, the less Ar is in the chamber and so it is expected Si active species in the forming plasma. One would probably expect that less Si is being incorporated, and from that could result a film with a higher stoichiometry. In the same manner, as the exposed area of the silicon target to the plasma is reduced through the introduction of Tb_4O_7 pieces, less Si could be sputtered to the plasma, so that could also result in less Si being incorporated in the films. Figure 37 shows, however, that Si and N concentrations are “somewhat independent” from these deposition parameters in the regions explored. So, the films show the same stoichiometry, except, perhaps, for slight deviations in the higher values of H_2 flux and area coverage – where a slight decrease in N incorporation is observed.

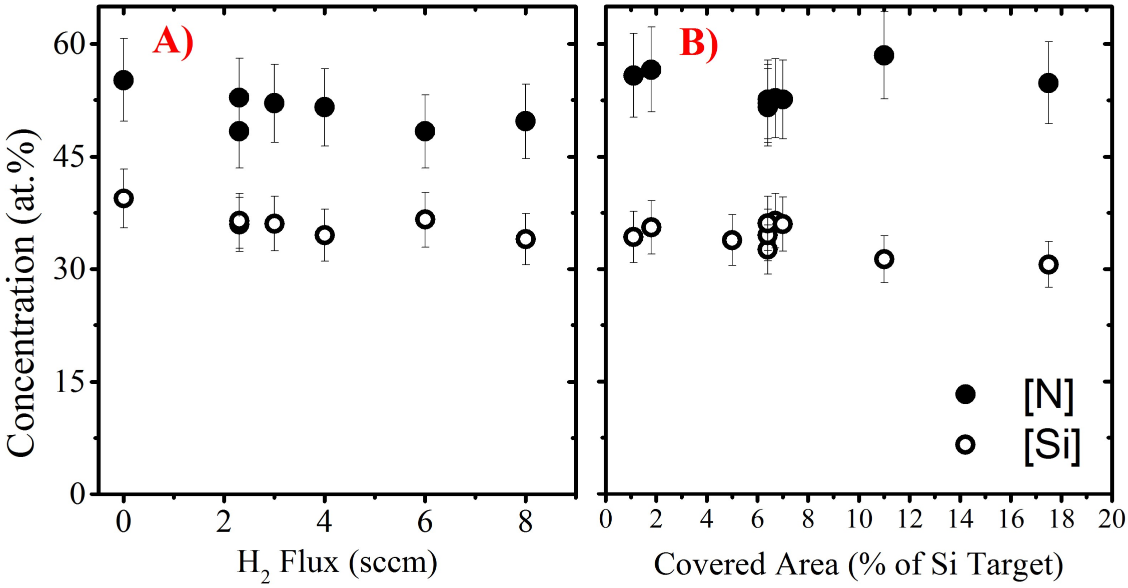

Figure 37: Si and N atomic fractions in Tb doped a-$SiN_{1.4}$:H thin films versus molecular hydrogen flux, **A**), and the area of the Si target covered by Tb_4O_7 powder chunks, **B**). The films were prepared using a constant partial pressure of N_2 always equal to 2.0 x 10^{-3} mbar. The graphs show independence of films’ stoichiometry with the other deposition parameters.

5.1.2 Terbium Incorporation

The sputtering yield is a function of several deposition parameters such as gas composition, pressure, and bias voltage. Thus, it is expected that a variation of deposition parameters such as H_2 partial pressure, the target covered area by terbium oxide (Tb_4O_7) and the partial pressure of N_2 in the chamber during deposition could influence the terbium incorporation. The quantitative characterization of the films' H incorporation was done ERD measurements.

The samples were grown using different H_2 gas fluxes and using different areas of Tb_4O_7 – this area is given in terms of the percentage fraction of the total area of the Si target.

In addition to other deposition parameters, for the Tb incorporation determination, the samples were fabricated also keeping constant: the overall pressure inside the deposition chamber and the partial pressure of N_2, respectively at 8.0 x 10^{-3} mbar and 2.0 x 10^{-3} mbar.

Figure 38 shows how an increase in H_2 gas flux can change both Tb (in black) and H (in red) incorporation. While no use of H_2 during deposition can produce films with [Tb] = 1.0 at.%, the introduction of H can slightly increase Tb level at low H_2 fluxes, at around 2.0 sccm, but monotonically decreases Tb incorporation as it is increased.

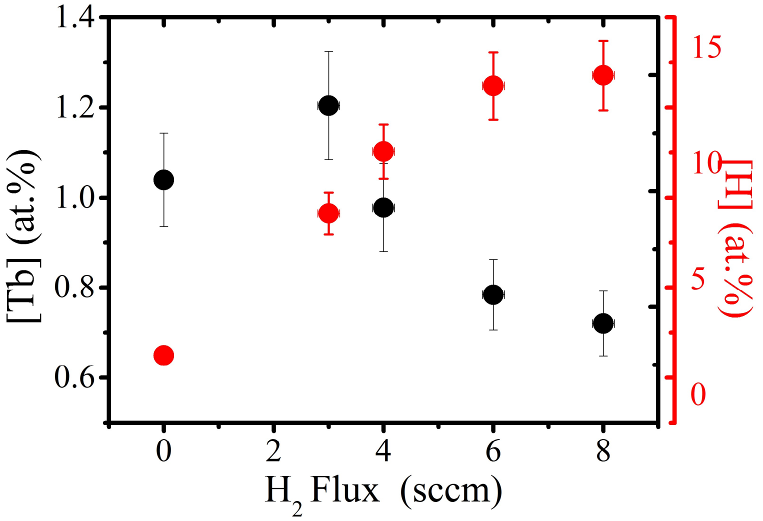

Figure 38: H (in red, right scale) and Tb (in black, left scale) atomic fractions in the films as a function of H_2 gas flow during deposition. The samples represented in this graph were prepared using partial pressure of N_2 equal to 2.0 x 10^{-3} mbar with the overall pressure constant at 8.0 x 10^{-3} mbar. H_2 gas flux variation in different depositions can almost double the Tb incorporation observed in the films while H atomic fraction monotonically increases up to 15 at.% and probably reaches a saturation point after 8.0 sccm of H_2 flux.

In the case of H incorporation, ERD results show that it monotonically increases up to 8.0 sccm where, even though the graph does not explicitly show, because it does not go further, H incorporation seems to saturate around 15 at.%. It should be noted that this result refers to both bonded and non-bonded H atoms.

Figure 39 shows Tb incorporation characterization as a function of metallic Si target covered area percentage by Tb_4O_7 chunks. In this graph, the amount of Tb incorporated by the films was corrected as if all the films were deposited using 6.0 sccm of H_2 gas flux. In the region showed, below 20% of the target area coverage, the level of Tb concentration increases somewhat linearly and can reach 2 at.%. This figure could be slightly higher if the H_2, as well as the N_2, levels inside the chamber were lower.

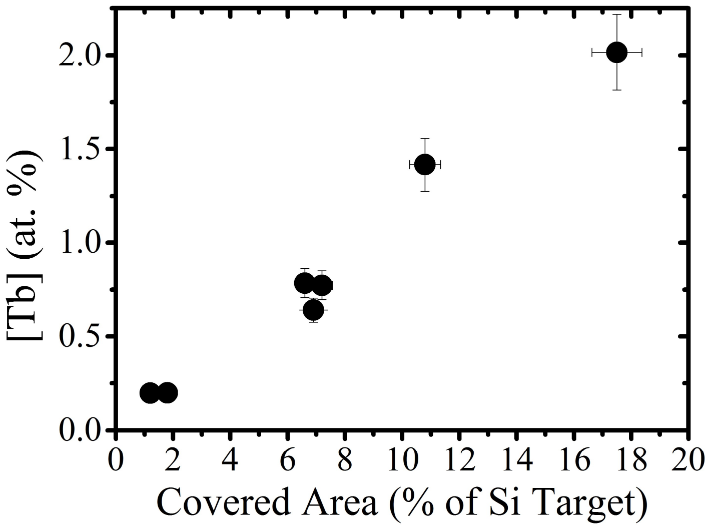

Figure 39 - Tb incorporation characterization of the Sputtering system in terms of the covered area by Tb_4O_7 tablets relative to the total area of the Si target. The data points are representative of a set of samples prepared using partial pressure of N_2 equal to 2.0 x 10^{-3} mbar and flux of H_2 of 6.0 sccm.

As Figure 40 shows, Tb incorporation in the films is very little influenced by the amount of incorporated N. As more N_2 is introduced in the chamber, evidenced by more N being incorporated, the amount of Tb in the films slightly diminishes. The data point shown were corrected, based on the changes that the other parameters have in Tb incorporation, to adjust to films grown using 6.8 ± 0.4 % of target area coverage and 2.3 sccm of H_2 gas flow. The error bars shown are different from the ones found Figure 39 because they also consider the uncertainties in the determination of the covered area and H_2 gas flow corrections.

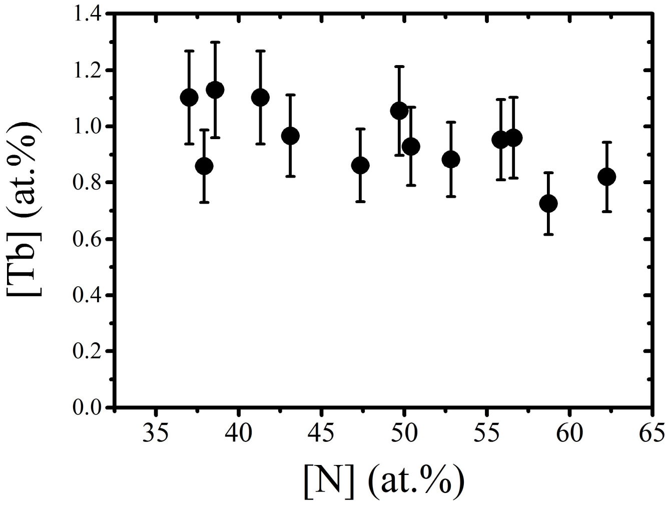

Figure 40 – Tb incorporation as a function of the incorporated N in the films. It was considered the influence of the covered area and in H_2 gas flow in the chamber. The incorporation of Tb shown here was corrected by the H_2 gas flow and area coverage by Tb_4O_7 as if they were grown using respectively a flow of 2.3 sccm and a covered area of 6.8 ± 0.4 %.

5.2 ECR PECVD

Chemical vapor deposition (CVD) is a thin film deposition technique that uses gas phase chemical reactions taking place at the substrate, the desired growth surface. What gives the precursors the necessary energy for film growth in classical CVD reactors is substrate temperature (thermal energy). For some applications, the thermal budget required is so high that plasmas are used instead as energy sources for the growth, removing the need for high substrate temperatures. This is the essence of plasma enhanced chemical vapor deposition (PECVD) technique. In PECVD, several different mechanisms can be used for plasma generation. Among them there is electron cyclotron resonance (ECR) ion source. In an ECR deposition system, the volume containing the low pressure gas is hit by microwaves at the exact frequency which corresponds to the cyclotron resonance of the electronic motion, defined by the magnetic field applied inside the volume [78]. Figure 41 gives a schematic drawing of an ECR process.

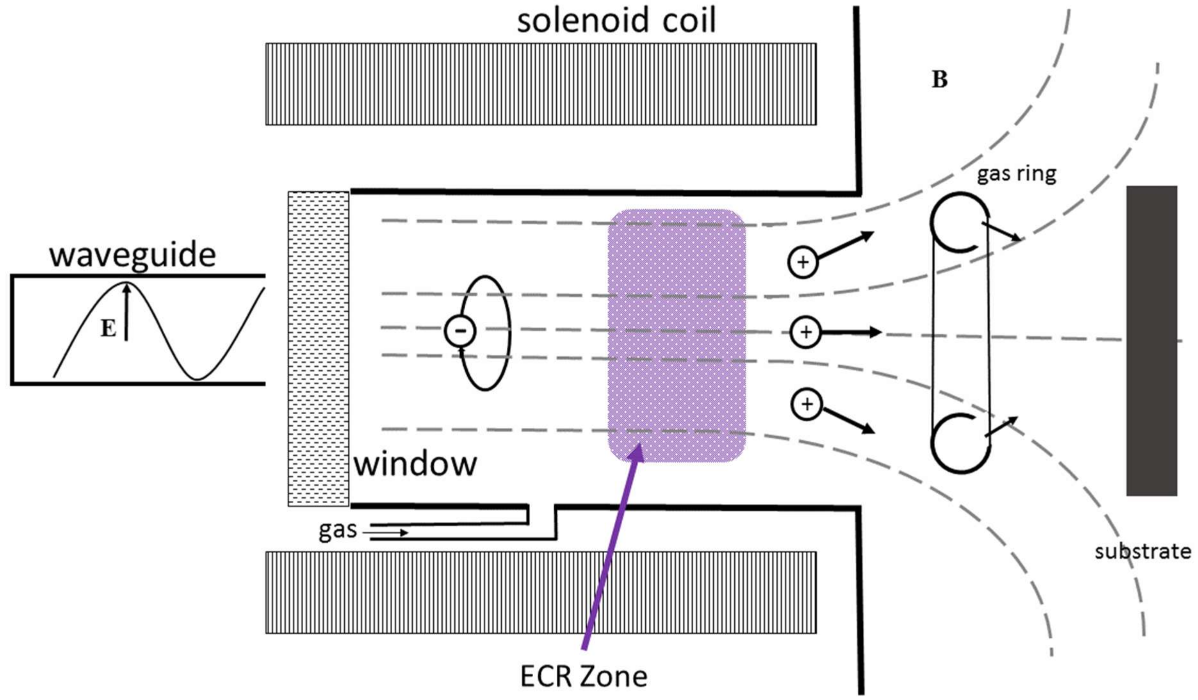

Figure 41: ECR plasma source driven by a waveguide. Electrons inside the gas chamber are accelerated perpendicular to **B** by the **E** field and move in orbits around **B** field lines – perpendicular to it. If the microwave angular frequency is the same as the angular frequency of the electron orbit, then we have the Electron Cyclotron Resonance condition ($|\mathbf{B}| = \omega_0 m_e / q_e$). For the commercial microwave band frequency of 2.45 GHz used, a magnetic field of 875 G is required to meet the resonance condition. Adapted of [78].

The ECR PECVD system used for this work is located at the Centre for Emerging Devices Technology (CEDT) at McMaster University, in Canada. It is composed by a reactor chamber coupled to a cylindrical chamber extension where the plasma is ignited, (see Figure

42). This extension is capped with a quartz window to allow the entrance of microwave radiation (at the commercial band frequency of 2.45 GHz) generated by an Astex HS-1000 magnetron head. The microwave radiation is conducted to the chamber through a waveguide whose output power is generated by an air-cooled S-1000 power supply. A reflected power detector monitor the power delivered back from the plasma to a water cooled dummy load and avoid any damage to the magnetron head. To meet the resonance condition, an 875 G magnetic field is generated by a helical electromagnet fed by 180 A generated by the high current power supply EMS 20-125-2D [149].

The reactor chamber is pumped by a 300 *l*/min Pfeiffer PMH 520 Turbomolecular pump. The typical base pressure obtained for depositions is of the order of 10^{-7} Torr. A load lock mounted above the main chamber, and separated by a gate valve, is used to reduce contamination of the deposition chamber by room pressure and to facilitate sample transfer. The gate to the reactor chamber is only opened after a minimum vacuum of 5×10^{-6} Torr is achieved. The sample is then transferred to the reactor chamber where it is positioned at the temperature controlled substrate stage. A Residual Gas Analyzer spectrometer monitored the base pressure purity to ensure impurity recognition before each deposition.

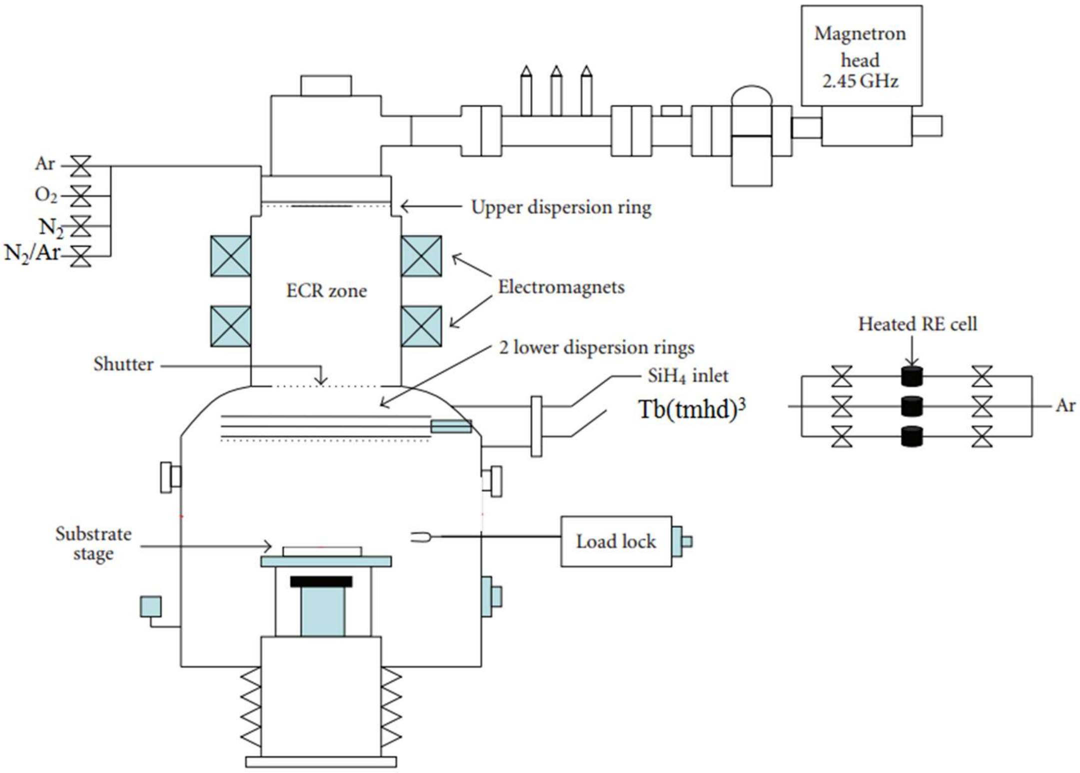

Figure 42: Schematic drawing of the ECR PECVD system used for depositions of nitrogen-rich a-SiNx:H at CEDT in McMaster University. Adapted from [150].

The insertion of Si, N, O, and H is controlled through the flux, using Mass Flow Controllers, of SiH_4, N_2, O_2. All of them, with exception of pure N_2 are diluted in Ar. Two main reasons justify the dilution: 1) safety: SiH_4 and O_2 are very flammable and reactive gases; 2) Ar dilution also allows better efficiency in gas ionization, and consequently in plasma generation. Argon has low ionization energy and, due to its molecular weight, its constant collisions with other ions that compose the plasma facilitates the ionization of other molecules [78].

Ions from the lanthanide family are *in situ* incorporated from metalorganic precursors, from the β-diketonate family. Solid at room temperature and pressure conditions, they are contained inside a canister where the temperature can be raised and controlled. The precursor is sublimated with a rate controlled by the heater cell temperature and by the flux of Ar gas, here used as carrier gas. The precursor used for terbium, specifically, was the volatile metalorganic complex β-diketonate Terbium(III) tris (2,2,6,6-tetramethyl–3,5-heptanedionate)-Tb(III) or Tb(tmhd)^3.

Tb-doped nitrogen rich a-SiN_x:H thin films were grown in Czochralski Si single crystal wafers. SiH_4/Ar (30% SiH_4 in Ar), N_2 and N_2/Ar (10% N_2 in Ar) gas mixtures were employed as silicon and nitrogen precursors, respectively. For better film homogeneity, an even distribution of SiH_4/Ar flow was achieved by specially designed dispersion rings containing pinholes through which the gas flows to the inside of the reactor chamber. Pure Ar was also used to enhance plasma density in some depositions. The sample set was prepared using SiH_4/Ar gas flow between 0.6 and 14 sccm; N_2 the gas flows between 5 and 20 sccm, N_2/Ar gas flow between and 20 and 50 sccm and Ar gas flow between 0 and 15 sccm. For better lateral uniformity, the substrates were rotated at 20 rpm. The terbium diffusion cell was heated up to 190ºC and the sublimated material introduced into the chamber alongside with silane, using Ar as a carrier gas, at a constant flow of 5 sccm. The Tb precursor cell line and the dispersion ring, located inside the chamber, through which the sublimated material was transported into the chamber were heated to 210ºC. This prevents the metalorganic complex to re-solidify along its way to the reaction chamber. The substrate stage was heated up at a constant temperature of 350ºC, which results in a surface temperature of about 120ºC [149]. Further details of the deposition system and film growth have been reported in [151].

All the deposition parameters used for the fabrication of the samples using ECR PECVD are in Appendix II.

5.2.1 Deposition Rate and Optical Parameters

Film growth in ECR PECVD is mainly conducted by the reactions of SiH_4 molecules with the other constituents of the forming gas. Thus, it is strongly dependent on the SiH_4 flow rate. As shown at Figure 43, the increase in SiH_4 forming gas flow increases the deposition rate almost linearly, but at around 10 sccm the increase seems to be reduced. For comparison with RF-Sputtering depositions, the films grown with the highest amount of N_2 had deposition rates of the order of 2.9 nm/min, but could increase to more than 6.5 nm/min.

Figure 44 shows the dependence of the E_{04} optical bandgap on the SiH_4 gas flow and the fraction N_2 flux to the Ar + N_2 gas mixture, as proposed by Alexandrov *et al.* (1998) [152]. Except in the extreme cases, of high SiH4 flow and high amounts of Ar in the forming plasma, the value of SiH4 flow used or the value of ratio $F_{N2}/(F_{N2}+F_{Ar})$ have little influence on (high) the optical bandgap of the films. This indicates that under the ECR-PECVD conditions used the samples are nearly stoichiometric a-Si_3N_4:H.

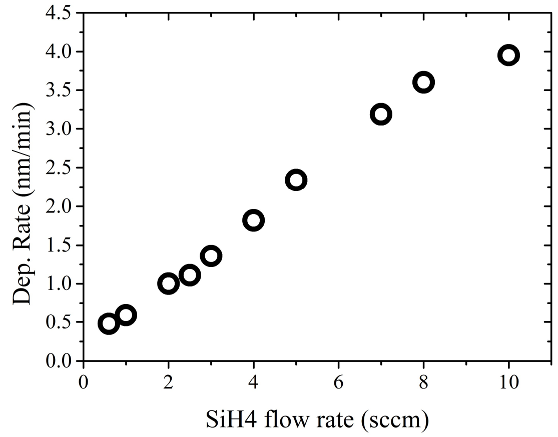

Figure 43: Deposition rate dependence by SiH_4 flow rate characteristic of the ECR PECVD system.

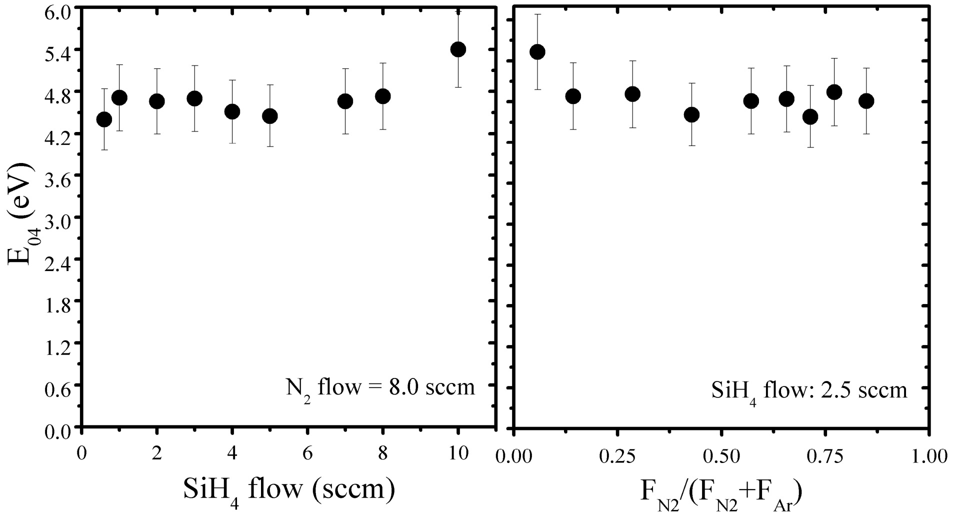

Figure 44: E_{04} optical gap as a function of the SiH4 gas flow (left) and fraction N_2 flux to the Ar + N_2 gas mixture (right).

5.2.2 Terbium Incorporation

In ECR PECVD deposition, there are two main ways of controlling terbium density in the films: a) controlling the precursor flow to the deposition chamber controlling the heater cell temperature and b) controlling the SiH_4 flow in the chamber.

Because the gas flow tubes are not uniformly heated, the vapor of the terbium precursor can be condensed during its way to the main chamber if the cell temperature used is too high, making the first method is very limited. Depending on the heater cell temperature chosen for a specific deposition, and, consequently, the pressure of the sublimated material along the line, the minimum temperature required to maintain the precursor in the vapor phase can be very different and result in possible condensations.

Nevertheless, higher terbium concentrations of up to 10^{22} at/cm^3 (equivalent to near 14 at.%) in nitrogen-rich films can be achieved by decreasing the silane flow for a fixed carrier gas flow. As it was shown in Figure 43, the deposition rate changes linearly in a somewhat linear fashion with the SiH_4 gas flow chosen to be operated. We decided to keep the Tb precursor flow constant with fixed heater cell temperature and carrier gas flow. Thus, the amount of Tb being incorporated in the films has a nearly reciprocal relationship with the SiH_4 flow. This is what is shown in Figure 45 below. Maintaining all the other deposition parameters constant, the flow of silane was varied from 0.6 to 10.0 sccm.

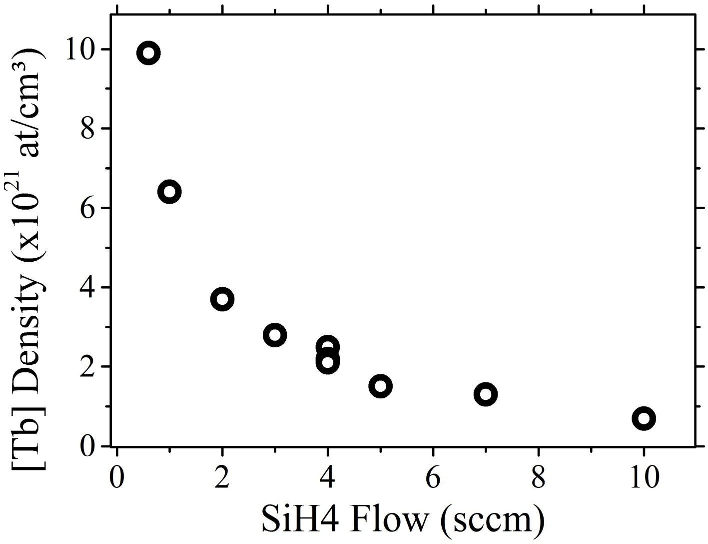

Figure 45: Terbium incorporation because of the silane flow change in the chamber during different depositions. All samples shown here were fabricated using low Ar gas flux but the pure nitrogen gas flow was changed.

5.2.3 Si-H Bonding

Bonded hydrogen densities were estimated using FTIR measurements of the Si–H and N–H stretching absorbance peaks (~2150 and 3350 cm^{-1}, respectively) over a wide range of annealing temperatures using the method of Lanford and Rand [141].

Figure 46 shows the peak wavenumber of Si–H stretching vibration mode for different amounts of N and H bonded to the Si. It illustrates the wavenumber increase when more electronegative elements, in case N and H, are bonded to Si in the Si–H bond instead of Si–Si bonds.

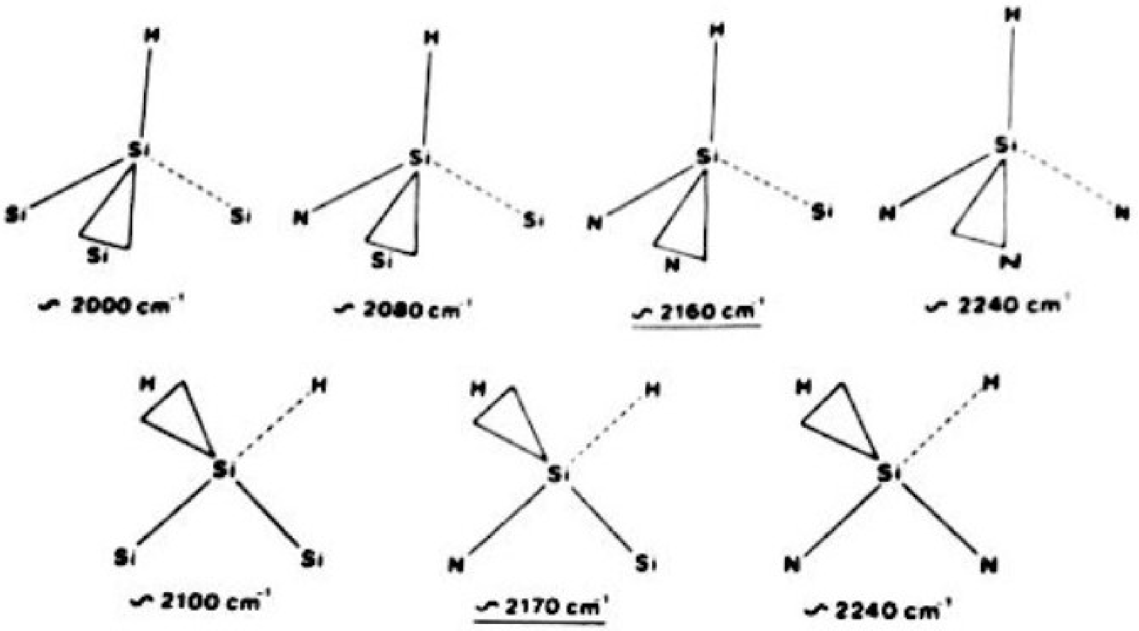

Figure 46: Peak energy of all different arrangements of the Si-H bond stretching vibration mode. Taken from [153].

Figure 47 illustrates the blueshift of the peak position of the stretching mode of the Si–H bonds because of SiH_4 flow increase between different samples – the region varied was between 0.6 to 10.0 sccm of gas flow; no Ar was used and the N_2 content in the chamber was kept constant at 8.0 sccm. The samples shown were characterized in as deposited situation. They show that as more silane is introduced inside the chamber, the resultant film will have less Si–H bonds being formed at the expense of a greater density of Si–N bonds (evidenced both by the increase of the area of the peak centered about ~890 cm^{-1} and by blueshift of the peak position of the stretching mode of the Si–H bonds). In the nitrogen-rich ambient, present inside the chamber during deposition, the breaking of the Si–H bonds in the plasma is followed by formation of Si–N and N–H bonds, which are much stronger – Table III.

Figure 48 shows the increase of N–H bond density as the Si–H bonds density decreases. After this point, the density of N–H bonds slightly decreases while the area related to the Si–N vibration mode continues to increase. This suggests that the increase of SiH4 gas flow favor the formation of molecular hydrogen microvoids rather than bonding with Si.

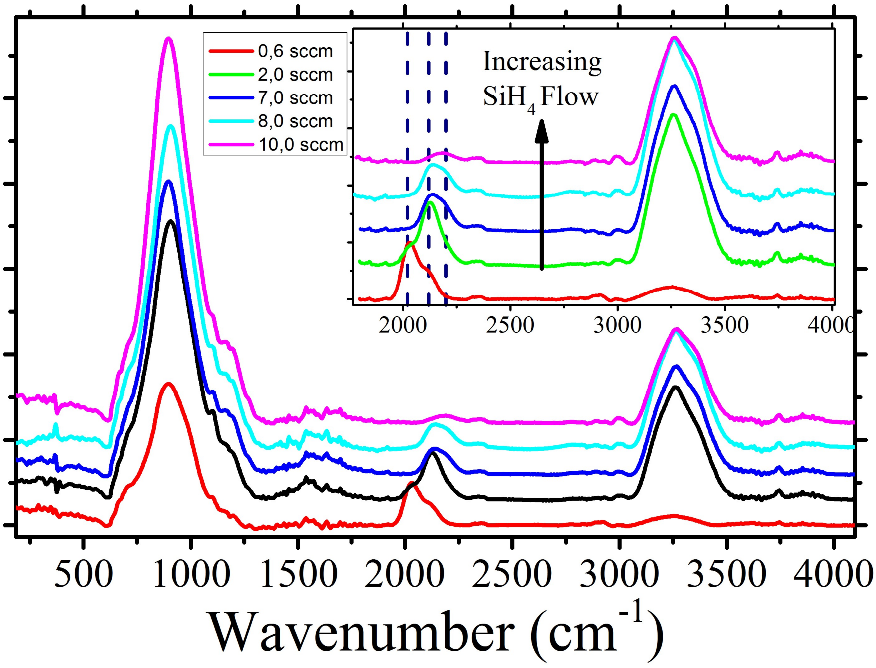

Figure 47: Evolution of Si–H bond peaks because of the increase of SiH4 gas flow. All samples show here were not annealed. The peak at ~2020 cm^{-1} refers to Si–H stretching mode in which Si is bonded to other Si atoms; The peak centered at ~2120 cm^{-1} refers to Si atoms bonded to at least one N instead; At ~2200 cm^{-1}, there are three possibilities of bonding in which the Si atom is bonded to more than one N or H.

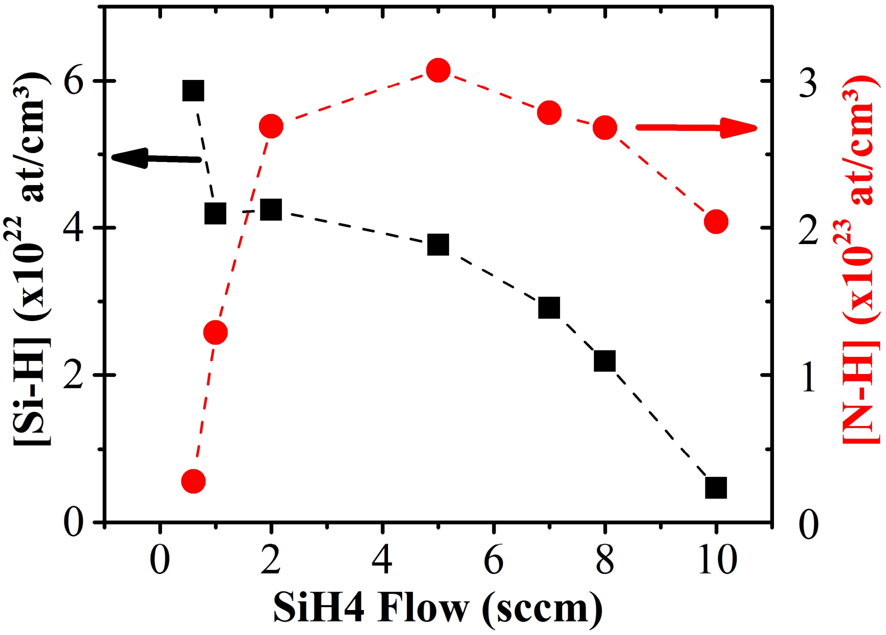

Figure 48: Evolution of Si-H bond density as result of SiH4 variation between depositions. [Si-H] and [N-H] bond densities were estimated using the Landford and Rand method.

6 Study of Tb^{3+} Photoluminescence in a-SiN_x:H

This chapter deals with Tb^{3+} photoluminescence in a-Si_3N_4:H<Tb> at room temperature.

The photoluminescence spectra observed in a-Si_3N_4:H<Tb> samples typically consist of Tb^{3+} related transition lines ($^5D_4 \rightarrow {}^7F_J$, J = 6, 5, 4 and 3) situated over a featureless broad spectrum related to recombination of carriers from the tail states of the a-Si_3N_4:H host matrix – see Figure 49. The physics background and interpretation of the spectrum was already covered in chapters 2 and 3.

To compute the total intensity of the Tb^{3+}'s transition lines, (from now on referred to as "RTPL") the area of the emission spectrum attributed to the Tb^{3+} lines subtracted the baseline the emission coming of transitions in the host.

Strong Tb^{3+} lines are only observed in samples with high enough values of E_{04} (typically of the order of 4.7 eV). Figure 49 is a clear illustration of it. For samples grown by reactive RF-Sputtering, where the bandgap is more easily tuned, it shows, in the vertical axis, the RTPL without normalization of sample thickness. In the horizontal axis, the N_2 partial pressure used during deposition. In sections 5.1.1 and 5.2.1, it was showed how the deposition parameters of the two growth methods vary the E_{04} optical bandgap. While in reactive RF-Sputtering, the bandgap of the films depends very strongly, and almost exclusively, on the N_2 partial pressure, saturating at 4.7 ± 0.4 eV for N_2 partial pressures higher than 2.0×10^{-3} mbar; in ECR PECVD, the samples have stoichiometric values E_{04} independently of the N_2 to Ar gas flow ratios used.

Moreover, Tb incorporation depends weakly on the N_2 partial pressure used. It seems to slightly decrease after 2.0×10^{-3} mbar, where there is high incorporation of N (Figure 40). So, the result shown at the graph of Figure 50 is related to the E_{04} bandgap opening in the sample series indicating a clear preference for high Tb emission in near stoichiometric samples. The subsequent decrease in RTPL with increasing N_2 pressure is caused by the slight decrease in Tb incorporation (Figure 40) combined with the decrease in the deposition rate, which, in turn, resulted in thinner films.

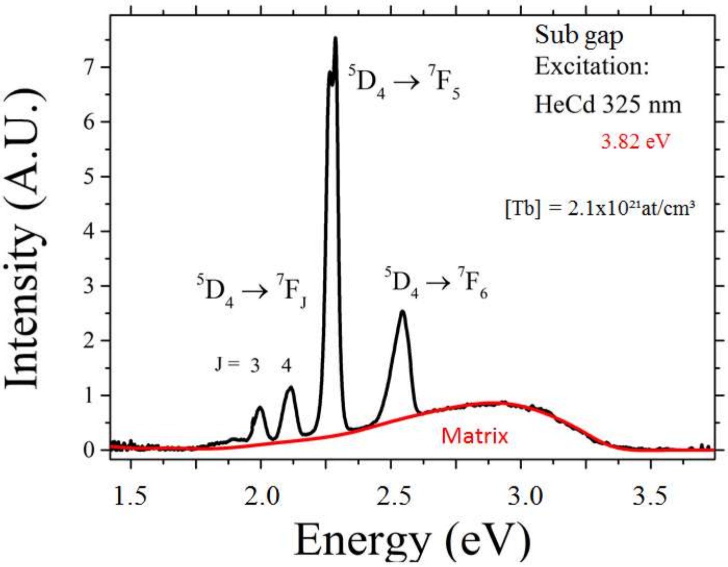

Figure 49 - Typical room temperature PL spectrum of Tb doped a-Si_3N_4:H (E_{04} = 4.9 eV) prepared by ECR PECVD showing the distinctive terbium lines over a broad spectrum (in red) related to recombination of carriers in the host. The shape of the host PL curve is distorted by the transfer function of the detection system that has a cutoff at 3.3 eV. In fact, the spectrum extends up to 0.4 eV below the subgap excitation.

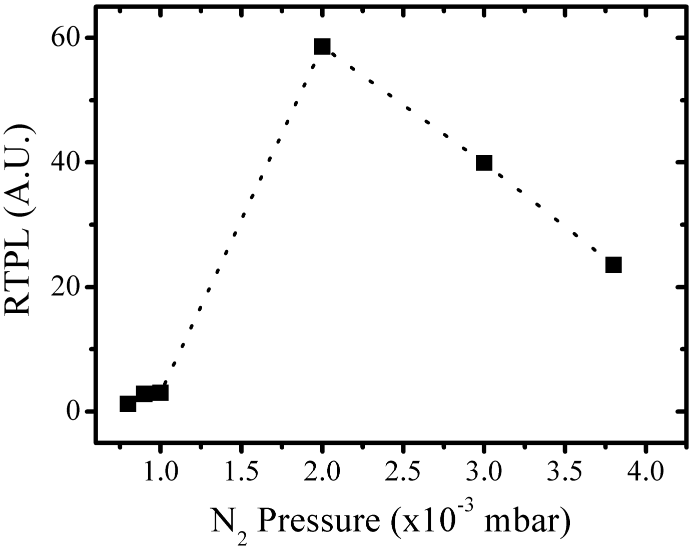

Figure 50: Integrated room temperature photoluminescence (RTPL) of the Tb^{3+} emission lines as a function of the N_2 partial pressure used for films prepared by sputtering. The coverture of the Si target by $Tb4O_7$ pellets was 6.7 ± 0.5 %. The total deposition pressure was 8.0×10^{-3} mbar.

In section 3.2.4 for a-Si:H and, later, at section 3.3 for a-SiN_x:H, the matrix's PL band shape was discussed. In the static disorder model [116], [121], [122] the PL band shape is the result of a convolution of the carrier distributions in the band tails states. Sub gap excitation truncates the PL band at approximately 200-400 meV below the excitation energy. Figure 51 shows the room temperature PL of as deposited undoped a-$SiN_{1.5}$:H (top) and Tb doped a-$SiN_{1.5}$:H (bottom) under three different excitation energies: 3.82, 3.31 and 2.54 eV. The sample has a bandgap of 4.7 eV, so all spectra correspond to subgap excitation.

Within the static disorder model, the carriers excited to the extended states thermalize very fast down to the band tails, populating it in a quasi-static distribution.

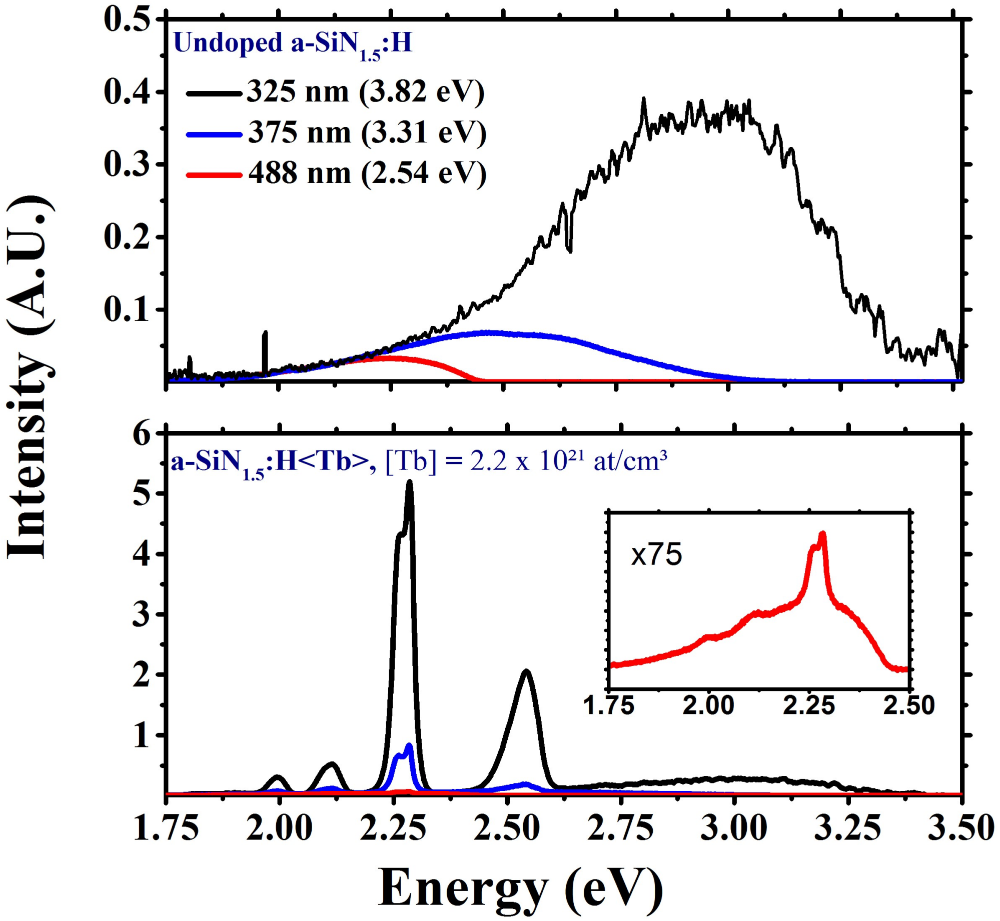

Figure 51: Room temperature PL emission of doped and undoped N-rich a-SiN$_{1.5}$:H under three different excitation wavelengths (325, 375 and 488 nm). The inset shows the PL spectrum put at the same intensity scale.

6.1 Tb Environment – EXAFS Characterization

One explanation for the changes of Tb^{3+} PL silicon based materials with annealing is a possible change in the oscillator strength of the ion due to chemical neighborhood changes around the ion [62]. This process is often refered to as “activation of the RE ion”. Judd-Ofelt theory states that a change in the local crystal-field around the ion, such as a change in the Tb’s site-symmetry, or in the crystal field strength, for example, can introduce changes in the matrix element of the transitions which, in turn, result in a lower radiative lifetime. This hypothesis was tested in our samples through EXAFS measurements. EXAFS was measured for samples prepared by reactive RF-Sputtering with Tb concentrations ranging from 0.8 up to 2 at. %.

EXAFS is very sensitive to the nanostructure around an absorbing atom. In the context of Rare-Earth doped amorphous silicon alloys, it allows us to know reliably some details of the first coordination shell. To determine these details, the EXAFS signal, $\chi(k) = [\mu(k) - \mu_0(k)]/\mu_0(k)$, is fitted to the equation below [139] (see section 4.1):

$$\chi(k) = \sum_j \frac{N_j S_0^2 f_j(k) e^{-2R_j/\lambda(k)} e^{-2k^2\sigma_j^2}}{kR_j^2} \sin[2kR_j + \delta_j(k)]$$

If the scattering properties of the j^{th} shell are known from a hypothetical structure believed to surround the ions, then the neighborhood characteristics can be determined. The scattering properties are specific for each scattering element and are given in terms of the scattering amplitude, $f_j(k)$, phase-shift, $\delta_j(k)$, and the mean-free path $\lambda(k)$. The chemical neighborhood is given in terms of the distance to the first shell of neighboring atoms, R_j, the coordination number, N_j, and the Debye-Waller factor, σ_j, which represents a mean-square disorder in the neighbor's distance. The parameter S_0, known as the amplitude reduction term, appears due to a relaxation of all the other electrons to the absorbing atom's core level hole. In Figure 52 are shown some steps of the EXAFS data treatment used for finding the Tb^{3+} first shell of neighboring atoms information.

Although the host is a-SiN_x:H, the fact that rare-earths in general are strong reducers, Tb^{3+} tends to coordinate with any oxygen available. Because terbium in the samples resulted from an oxide precursor, it is reasonable to expect this residual oxygen to compose Tb's chemical neighborhood.

The evolution of R_j, N_j , and σ_j .with annealing temperature for a sample containing 0.8 at.% Tb is represented in Figure 53. Annealing does not cause strong changes to the Tb^{3+} neighborhood: it slightly and monotonically decreases the Debye-Waller factor (indicating that the radial disorder of the first coordination coordination shell decreases with annealing, as expected), the coordination, and the Tb-O interatomic distance. Oxygen is always slightly closer to Tb than in Tb_2O_3 – calculated by FEFF software package. This is probably due to the difference in electronegativity between Tb and Si or N that compose the second sphere of neighbors. This situation is similar to that of Er doped a-Si:H and a-SiO_x:H [154]-[156].

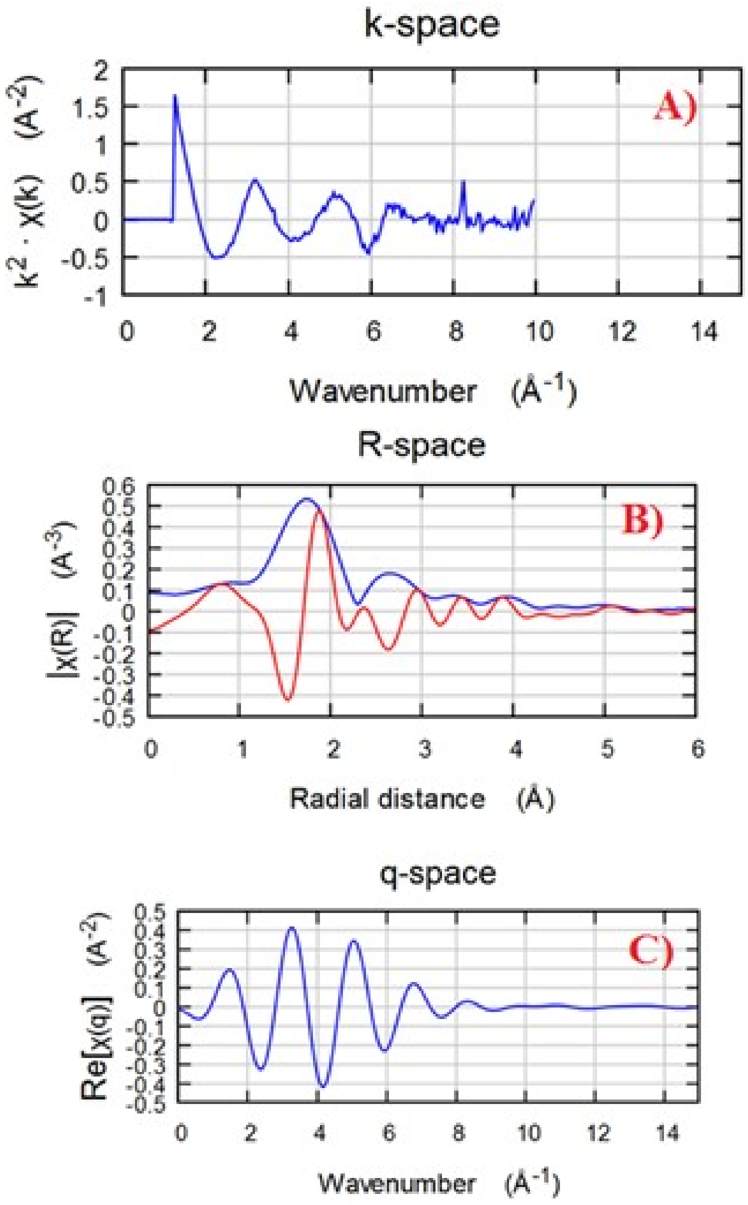

Figure 52 – **A)** The $\chi(E)$ signal evidencing the EXAFS oscillations - calculated from the data shown in Figure 24 multiplied by the electron's momentum squared ($k^2 = 2m(E - E_0)/\hbar^2$); **B)** Fourier transformation of $k^2\chi(k)$. In blue is the function modulus and in red its imaginary part. The blue curve represents, excluding a phase-shift resulting from the electron's wavefunction scattering, the distribution of neighboring atoms around Tb^{3+}. In other words, the first peak is the first shell of neighbor's radial distance shifted by some amount given by a signal phase shift; **C)** Fourier transformation of the radial distribution relative to the first shell of atoms. With a good hypothesis regarding the identity and coordination number of the neighboring atoms, the EXAFS equation for the first shell can be fitted to this signal. With that, N, R and σ are determined.

Within the experimental error bars, nothing dramatic happens to the Tb neighborhood with annealing. Although the average coordination may be slightly reduced from 6 to 4 when the samples are annealed at 250°C, this is a very unlikely situation because that is precisely the deposition temperature in RF-Sputtering – see Table IV with the deposition parameters kept constant throughout the whole project. The error bars obtained in the analysis are compatible with Tb^{3+} being already coordinated to 4 oxygen atoms in average for as-deposited samples, so no changes in the atomic coordination number are observed even for temperatures as high as 1100 ºC. The Debye-Waller factor, however, decreases with annealing temperature indicating, as expected, that annealing relaxes the network around the Tb^{3+}. Thus, the reasons for the maximum photoluminescence intensity to occur for annealing at 300/400°C [157] are most probably not related to a modification in the chemical neighborhood around Tb^{3+} but is a result of modifications in the host.

Although the error bars are high - except for the average interatomic separation - the trends are normally consistent with the expected effects of annealing. Parameter correlation causes the high values of the error bars and are a limitation of the EXAFS technique.

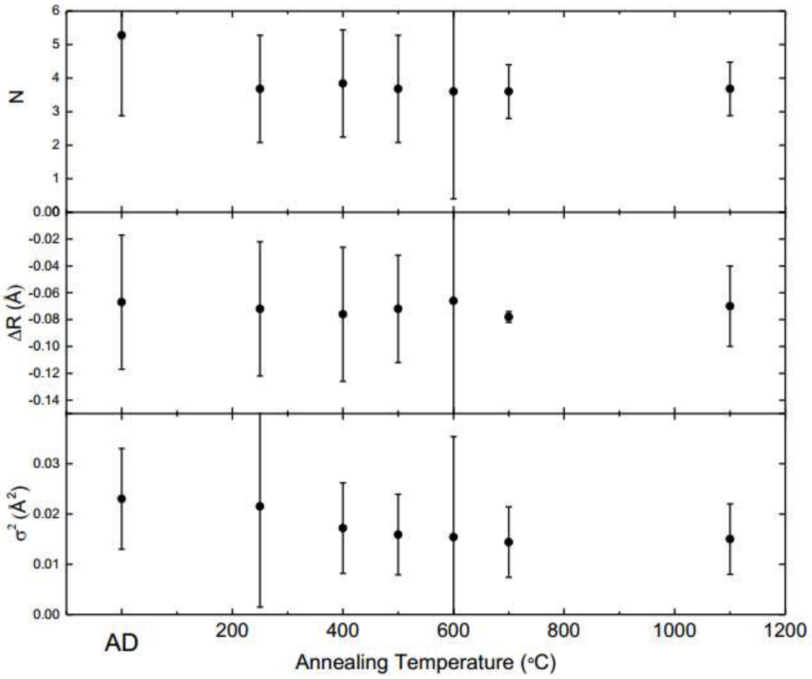

Figure 53: Chemical neighborhood around Tb^{3+} ions in a-SiN_x:H thin films as a function of the annealing temperature. N, ΔR and σ^2 give respectively, the average coordination number, bond length average variation (relative to Tb_2O_3) and Debye-Waller factor. The neighborhood around Tb^{3+} almost does not change with annealing temperature.

6.2 Terbium Ions' Spatial Distribution

Another hypothesis very used to justify Tb excitation from the Si host, is a possible presence of Si nanoclusters (Si-ncs) or nanostructures which, resonantly, transfer energy from the host to the Tb^{3+} ions. Several reports account room temperature RE^{3+} PL changes and enhancement due to Si-Ncs formation and/or RE clustering [60], [158]–[161] as a result of specific thermal treatments.

As a semi-quantitative clustering test, first neighbor's distribution test of APT results (or more often used, nearest neighbor distribution, NN) can be applied for chemical elements of interest. NN techniques examine the interatomic separations in the immediate vicinity around each atom [134]. While this method doesn't identify specific clustering formation, it is a good test to identify trends over clustering composed of an element of interest. It does so by comparing the actual sample with a solid of randomly distributed atoms of equivalent composition [134].

Nearest neighbor's investigation can also be extended to higher orders, i.e., to larger spherical shells, often referred to as kNN, where k designates the order. Figure 54 shows 1NN and 10NN distributions for a selected film grown by reactive RF-Sputtering and annealed for 1h in N_2 ambient at 1100ºC. Such an analysis makes clear that, within the technique limitation and sensibility, there is no clustering in our films at high high annealing temperatures.

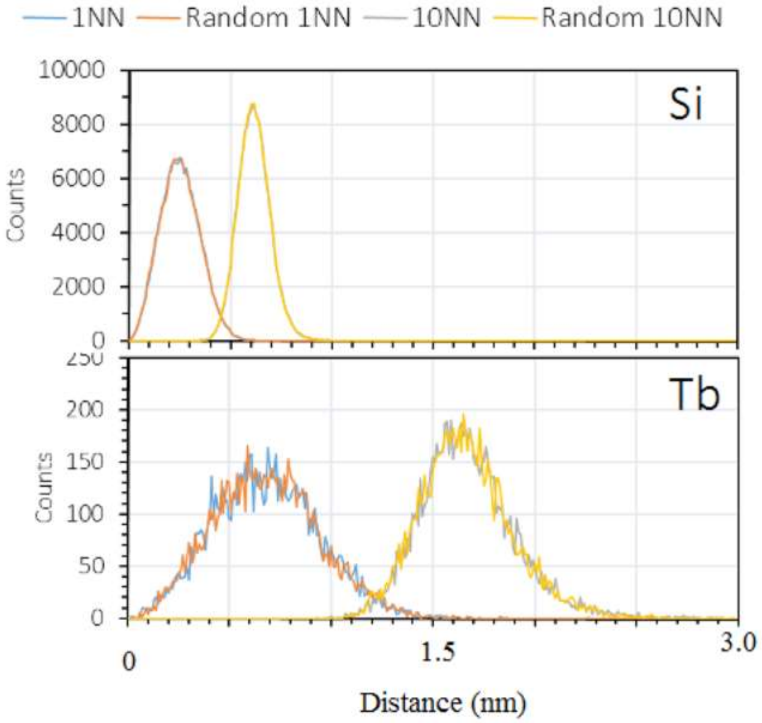

Figure 54: Nearest neighbor distributions of an ECR PECVD grown film. 1NN refers to the first shell of neighbors and 10 NN to the 10th shell of neighbors around Si and Tb atoms. The ample was annealed for 1h under pure N_2 flux at 1100ºC. Note that the actual distribution resembles simulated random distribution of atoms around the two centers.

6.3 Concentration Quenching

Concentration quenching is often referred to the decrease in the PL signal as a result of the rare-earth trivalent ions concentration in the material. It is a very general attribute of rare-earth luminescence and is caused by an increase of cross-relaxation rate between two nearby ions because of a decrease in the average ion-ion distance, as stated by the Förster-Dexter mechanism.

This effect is expected in every rare earth doped material and appears for both sets of samples studied in this work. Nevertheless, the effect was verified with more details in our set of samples grown by ECR PECVD. It was verified that the Tb concentration for maximum sub gap excited photoluminescence was 2.7 at.% or $(2.1 \pm 0.1)\times10^{21}$ at/cm^3, which corresponds, on average, according to a modified Chandrasekhar model [60], [159] for random distribution of ions to an interatomic Tb-Tb distance of 0.49 ± 0.04 nm - Figure 55.

Furthermore, as discussed by Benz *et al.* [161], the interaction between rare-earth ions follows from Förster-Dexter mechanism which is eventually dominated by Dexter electron exchange mechanism in the high concentration regime in which there is an exponential dependence with Tb-Tb distances according to the equation:

$$I = \frac{NA}{1 + Bexp(-r/r_0)} \qquad (22)$$

where N is the number of radiative centers and r_0 is an effective Bohr radius; A and B are experimental constants related to the probabilities of cross-relaxation and radiative emission.

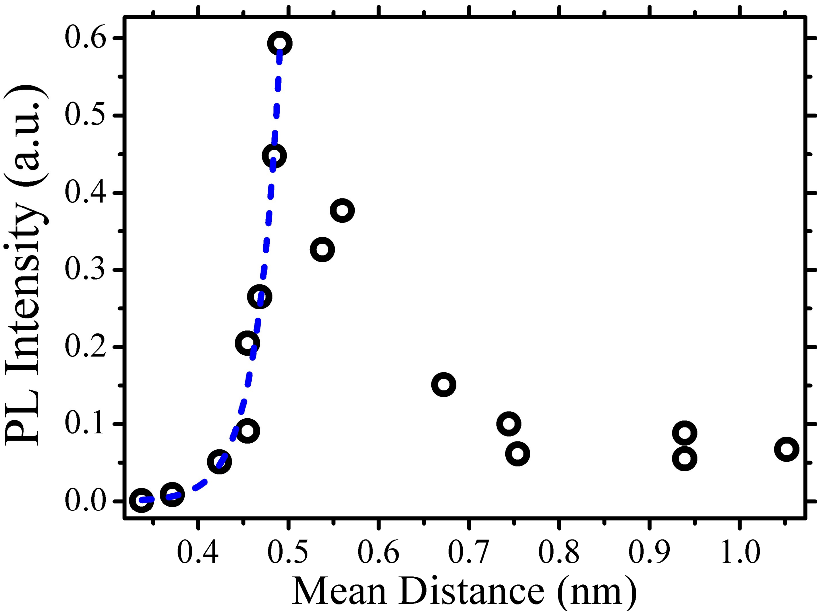

Figure 55: PL intensity of the samples annealed at 400ºC as a function of the average interatomic distance of Tb^{3+} ions as described by Benz et al. The blue curve shown has as parameters: NA = 13700, B = 23.8 and r_0 = 0.027 nm.

Even though Benz *et al.* [161] suggests that for the low concentration region there is a R^{-3} dependency, this is not sufficient to describe the data in the full extent shown in Figure 55. We believe, as it will be more evident in the subsequent sections, that this region is characteristic of an increasing number of optically active Tb ions available coupled with the defects. So, strongly dependent on defect density, or, indirectly, dependent on the conditions of deposition and annealing treatments employed for film growth.

6.4 FTIR analysis and Tb^{3+} excitation through Si-dbs

One possible way to directly explore the influence of the Si-dbs in the excitation of Tb^{3+} ions is through the analysis of the Si-H bonds. The Si-H bond density is changed with different annealing treatments. The direct correspondence between Si-H bonds breaking to the creation of Si-dbs in nitrogen rich a-SiN_x:H is well known [125].

Figure 56 shows three samples grown by ECR PECVD with stoichiometries at 1.5, E_{04} bandgap at 4.7 eV, but with different Tb concentrations, each represented by one column. A table of graphs is represented in each row of the table where it is shown the [Si–H] bond concentration as well as the total room temperature PL Tb^{3+} ions, and the emission from a-SiN_x:H as a function annealing temperature. Row A) shows RTPL. Row B) shows the total host emission. Row C) shows the [Si–H] bond density.

For the three samples shown, the number of Si–H bonds increases by a factor of at least 2 with annealing temperature, from 300ºC to 600ºC. The annealing temperature that optimizes the RTPL is around 300ºC. At higher temperatures, the annealing procedures only decreases the Tb^{3+} RTPL intensity coinciding with a rise in the [Si–H] bond density. At the same region, as shown in row B), the total PL coming from the silicon nitride matrix increases with annealing temperature. According to the Defect Related Auger Excitation model (DRAE), Figure 57, originally proposed for Er in a-Si:H [72], the lanthanide ions are excited resonantly from the matrix through an Auger process that involves the recombination of an electron with a hole in a neutral silicon dangling bond defect. So, a decrease in the Si-dbs density, indirectly observed through the increase of [Si–H], would excite fewer Tb^{3+} ions. In contrast, once there is less Si-dbs to compete with the radiative band tail recombination, this process is favored resulting in an increase in the silicon nitride emission with annealing temperature – as shown in row B.

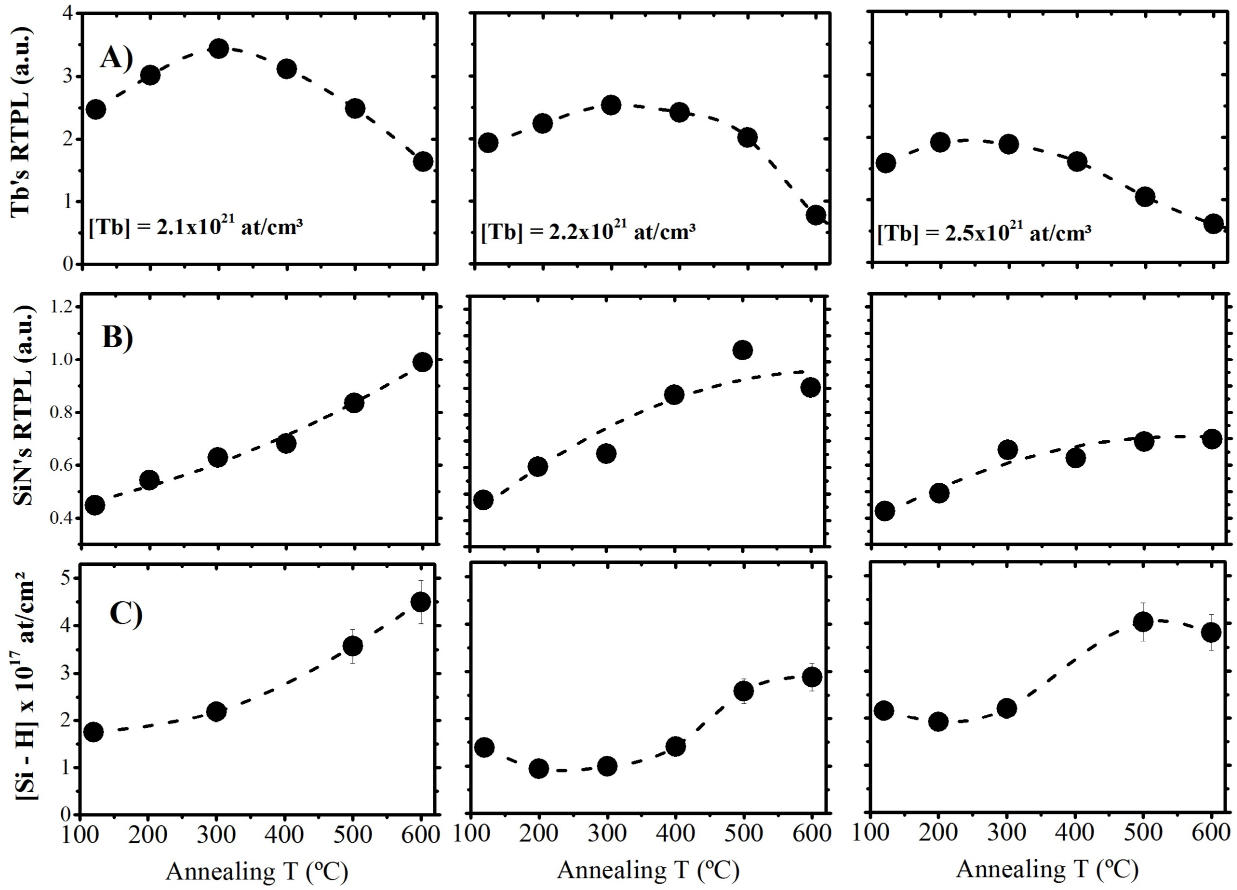

Figure 56: [Si - H] bond density, Tb and a-$SiN_{1.5}$:H room temperature PL (RTPL) as a function of annealing temperature for three different concentrations of Tb^{3+}. Each sample, contain respectively 2.1, 2.2 and 2.5×10^{21} at/cm^3 and are identified by one column of graphs. Each row gives one of the investigated aspect of the film. Row A) gives Tb room temperature sub gap excited PL; row B) the a-$SiN_{1.5}$:H photoluminescence and; row C) the [Si – H] bond density as a function of annealing temperature from as deposited, identified by the points near 100º C, the surface temperature during deposition, up to 600º C. As the [Si – H] bond density increases with annealing temperature at 500 and 600 ºC, Tb photoluminescence decreases substantially while the emission coming from recombination between the band tails increases. This result supports the DRAE model, where recombination at the Si-dbs, the trap centers, transfer energy to the Tb^{3+} ions, and competes with the radiative recombination between carriers at the band tails.

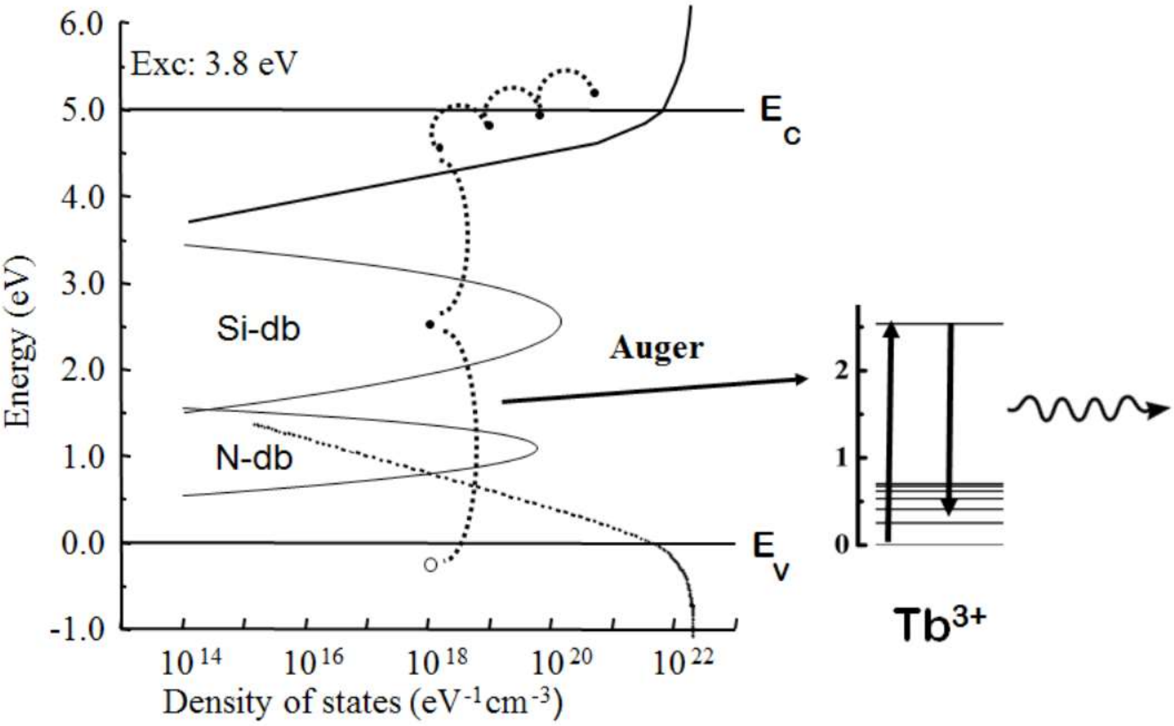

Figure 57: Schematic representation of the DRAE Energy transfer mechanism adapted to the nitrogen rich a-$SiN_{1.5}$:H<Tb> films grown by ECR PECVD. An excited electron relaxes down to the bandtails where it occasionally is trapped by a Si-db. Once in this energy position, the electron can recombine with a hole situated at the valence extended band transferring near-resonantly its energy to promote the excitation of a nearby Tb^{3+} through an Auger process.

6.5 Deposition Method Comparison

Because PECVD methods of growth typically operate in energy scales smaller than Sputtering methods [78], it is expected differences in the structure of the two sets of films. In terms of concentration of Si-dbs, which was cited in last section, films prepared by ECR PECVD are expected to have less defects than films prepared by more energetic methods such as reactive RF-Sputtering.

For a comparison of the Tb RTPL (excited at 325 nm) between two sets of samples be made it was necessary to isolate the other variables that may influence Tb emission, such as: film thickness and PL signal modulation by interference fringes [162], Tb concentration, and optical bandgap. Therefore, samples grown by ECR PECVD and by RF-Sputtering, were chosen in the low Tb concentration region (each containing, $4.7\times 10^{20}\ at/cm^3$ and $10\times 10^{20}\ at/cm^3$for PECVD; $5.9\times 10^{20}\ at/cm^3$and $9.0\times 10^{20}\ at/cm^3$ for Sputtering) with the same optical bandgap (E_{04} = 4.9 eV). Their thicknesses are in Figure 58. They were both deposited over crystalline Si substrates but, due to the high transparency, no interference fringes were observed. For such Tb concentrations, concentration quenching is not important. Tb PL can be considered to depend linearly with Tb concentration. A linear relationship between thickness and light emission can be also assumed because the films are very transparent (at 325 nm, the wavelength where the PL of the films were excited, the penetration depth, $1/\alpha_{\lambda=325\,nm}$, are of about 10^4 nm – much longer than film thicknesses). So, PL spectra divided by both thickness and Tb concentration for the two films could be used to compare the Tb PL for each deposition method.

A comparison of PL spectra of samples with similar compositions and properties, each grown by one deposition technique, and corrected by Tb concentration and film thickness is shown in Figure 58. Both sets of samples presented strong Tb^{3+} related emission lines which, in shape (given by position and linewidth) are roughly the same except for their intensity. They are over an emission related to the host silicon nitride which are very similar for both. The Tb PL in the shown RF-Sputtering grown samples are significantly higher than for samples grown by ECR PECVD. Given the results of last section, about the correlation between Si-dbs density and Tb PL, we believe that Tb PL intensity reflects the Si-dbs density present for each. In fact, a higher density of defects benefits Tb light emission because it can excite more Tb^{3+} ions that can decay radiatively.

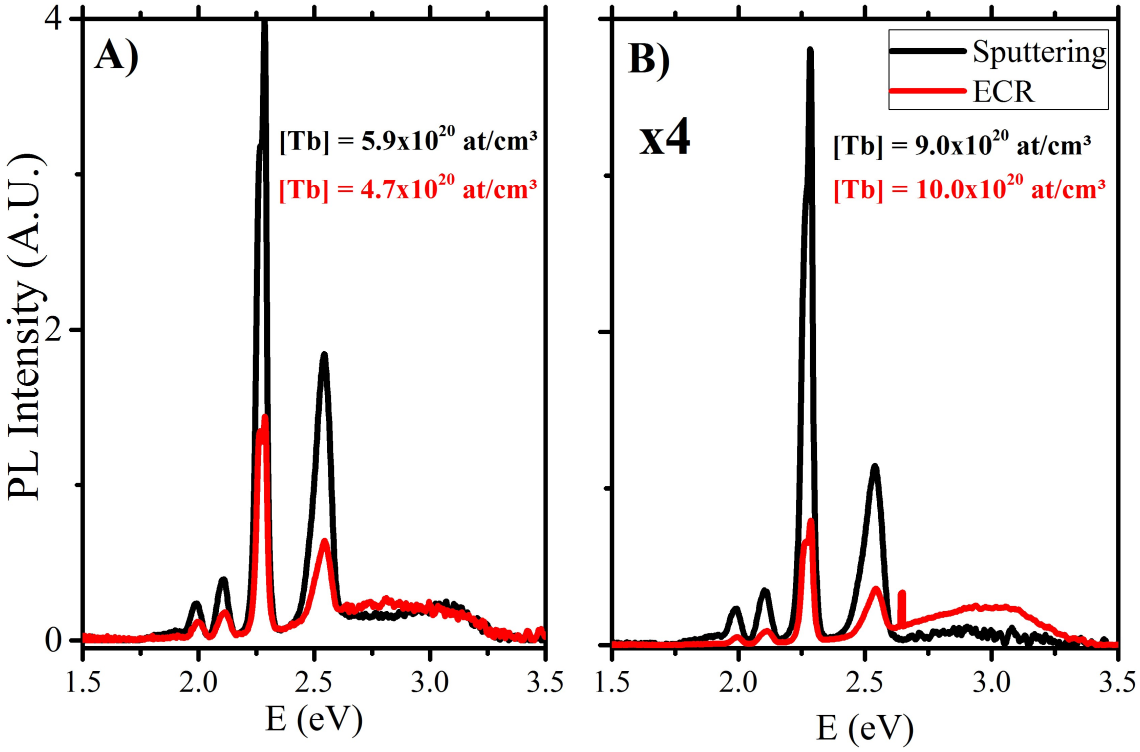

Figure 58: PL spectra of samples with similar compositions grown by ECR PECVD, in red, and Sputtering, in black, (all have E_{04} = 4.9 eV). The PL spectra were measured using a 325 nm HeCd laser source. The PL spectra were divided by Tb density and thickness. For RF-Sputtering grown samples (Appendix I) the Tb concentrations and thickness were: **A)** sample 17, $5.9\times 10^{20}\ at/cm^3$ and 509 nm; **B)** sample 27, $9.0\times 10^{20}\ at/cm^3$ and 614 nm. For ECR PECVD grown samples (Appendix II): **A)** sample 8, $4.7\times 10^{20}\ at/cm^3$ and 95 nm; **B)** sample 53, $10\times 10^{20}\ at/cm^3$ and 76 nm.

7 Conclusions and Perspectives

This study was aimed at pushing further the debate regarding the excitation mechanisms of Tb ions within amorphous Si-based materials. Moreover, this study had as objective the provision of information on rare-earth doped Si-based thin films produced by two independent deposition methods, reactive RF-Sputtering and ECR PECVD, and how they compare to each other.

The films were prepared varying widely the deposition parameters – which can be seen in Appendices I and II. Samples had stoichiometry, deposition rate, refractive index, extinction coefficient, incorporation of terbium, terbium chemical neighborhood, sensity of Si-H and N-H bonds and sub gap excited room temperature photoluminescence measured.

In sputtering-grown films, terbium incorporation is controlled by target configuration and depends very weakly on the composition of the forming plasma. Tb concentrations of about 1.8 at.% (or, roughly, $1.4{\times}10^{21}\ at/cm^3$) were achieved when the Si target had about 17% of its area covered by Tb_4O_7 powder pellets. The E_{04} bandgap of the films increases somewhat linearly with the partial pressure of N_2 from 1.8 eV - for depositions using almost no N_2 (a-Si:H like films) - and saturates at the stoichiometric value of 4.7 eV - when the partial pressure of N_2 in the chamber is raised to $2.0{\times}10^{-3}$ mbar. Further increase of N_2 partial pressure in the forming gas result in films with the same stoichiometric value of E_{04} bandgap but the deposition rate and Tb concentration decreased.

In ECR PECVD grown films, the incorporation of Tb can be easily adjusted varying the SiH_4 flow used for growth while maintaining film the precursor flow constant. The film stoichiometry corresponds to a-Si_3N_4:H. Consequently, the Tb incorporation is roughly inversely proportional to the deposition rate. Tb concentrations of about 14.0 at.% (or $1.0{\times}10^{22}\ at/cm^3$) were achieved, using SiH_4 gas flow rate as low as 0.6 sccm. The films, however, were all stoichiometric within the deposition parameter region explored – which included wide variations in N_2 and Ar gas flow rates. No clear relationship appears between Tb incorporation and N_2 and Ar gas flow configurations used in each deposition. The side effect of the increase in SiH_4 gas flow, however, is the increase in Si-N bond density while decreasing Si-H concentration. For the conditions used in this work, N-H bonds density increases very rapidly when the SiH_4 gas flow reaches 2 sccm. It decreases only after 8.0

sccm is used.

Changes in the photoluminescence of the samples caused by post-deposition annealing were also investigated. Annealing had no effect on the PL spectrum shape and the position of Tb^{3+} transition lines, but it strongly affected the intensity of Tb^{3+} PL lines. The annealing temperatures for the brightest PL of Tb^{3+} ranged between 200 and 400ºC in ECR PECVD grown samples while it was a little bit higher (around 400 ºC) in RF-sputtering grown samples. This can be related to the different substrate temperatures in each deposition system.

A definitive evidence of the stability of the chemical neighborhood around Tb ions (in films produced by RF-sputtering only) was obtained by EXAFS spectroscopy. Independently of the Tb concentration in the region between 0.8 and 2 at.% and the annealing temperatures used, the Tb atoms were surrounded by a shell of first neighbors composed of 4 O atoms whose distances are very close to the Tb-O bond length in Tb_2O_3 (deviations of only 0.05 Å). Despite not being directly measured, a similar result can be expected for the Tb ions in ECR PECVD grown films because in the metalorganic precursors used for Tb it is in an octahedral oxygen cage.

This thesis work also provide the first direct measurement of the random distribution of Tb in a-$SiN_{1.5}$:H films even after post-deposition annealing at temperatures as high as 1100 ºC. The Tb spatial distribution was obtained through 3D atomic reconstruction obtained from atom probe tomography results.

We also provide evidence for one probable way for Tb^{3+} excitation through Si-dbs. We found an inverse correlation between the density of Si-H bonds and the Tb emission. The results are consistent with the DRAE model [72]. In near stoichiometric samples, electrons trapped in these defects can recombine with holes from extended or shallow localized states providing energies near to 2.5 eV which excite a Tb^{3+} ion through the $^5D_4$ – $^7F_6$ transition by an Auger process.

Knowing that the Si-dbs are the main path for Tb^{3+} optical excitation, it seems clear that the main difference in Tb PL between films grown by PECVD and by RF-sputtering is of density Si-dbs present in each film. Therefore, as shown by the comparison of the PL of samples with similar characteristics and Tb concentrations - but each grown by one method -, RF-sputtering grown samples presented higher Tb^{3+} PL than ECR-PECVD grown samples. Both samples have the same intensity of luminescence from the silicon nitride matrix.

Future work should investigate quantitatively the concentration of Tb and Si-dbs which maximize Tb light emission, or, even better, in terms of the external quantum efficiency.

With this work, we expect to have pushed further the knowledge about the mechanisms of Tb^{3+} emission in a-SiN_x:H<Tb> films. We hope the information provided in this thesis will be useful for possible future developments of Si-based light sources, particularly for visible light applications.

8 Bibliography

[1] T. K. Liang, H. K. Tsang, I. E. Day, J. Drake, A. P. Knights, and M. Asghari, “Silicon waveguide two-photon absorption detector at 1.5 µm wavelength for autocorrelation measurements,” *Appl. Phys. Lett.*, vol. 81, no. 7, p. 1323, 2002.

[2] A. Liu, L. Liao, D. Rubin, H. Nguyen, B. Ciftcioglu, Y. Chetrit, N. Izhaky, and M. Paniccia, “High-speed optical modulation based on carrier depletion in a silicon waveguide,” *Opt. Express*, vol. 15, no. 2, p. 660, Jan. 2007.

[3] A. Politi, M. J. Cryan, J. G. Rarity, S. Yu, and J. L. O’Brien, “Silica-on-Silicon Waveguide Quantum Circuits,” *Science (80-.).*, vol. 320, no. 5876, 2008.

[4] F. Xia, L. Sekaric, and Y. Vlasov, “Ultracompact optical buffers on a silicon chip,” *Nat. Photonics*, vol. 1, no. 1, pp. 65–71, Jan. 2007.

[5] G. Lammel, S. Schweizer, and P. Renaud, “Microspectrometer based on a tunable optical filter of porous silicon,” *Sensors Actuators A Phys.*, vol. 92, no. 1, pp. 52–59, 2001.

[6] S.-S. Yun and J.-H. Lee, “A micromachined in-plane tunable optical filter using the thermo-optic effect of crystalline silicon,” *J. Micromechanics Microengineering*, vol. 13, no. 5, pp. 721–725, Sep. 2003.

[7] T. Dai, A. Shen, G. Wang, Y. Wang, Y. Li, X. Jiang, and J. Yang, “Bandwidth and wavelength tunable optical passband filter based on silicon multiple microring resonators,” *Opt. Lett.*, vol. 41, no. 20, p. 4807, Oct. 2016.

[8] Yue Wang, D. Stellinga, A. B. Klemm, C. P. Reardon, and T. F. Krauss, “Tunable Optical Filters Based on Silicon Nitride High Contrast Gratings,” *IEEE J. Sel. Top. Quantum Electron.*, vol. 21, no. 4, pp. 108–113, Jul. 2015.

[9] X. Chen, Y. Shi, F. Lou, Y. Chen, M. Yan, L. Wosinski, and M. Qiu, “Photothermally tunable silicon-microring-based optical add-drop filter through integrated light absorber,” *Opt. Express*, vol. 22, no. 21, p. 25233, Oct. 2014.

[10] T. Tanabe, K. Nishiguchi, A. Shinya, E. Kuramochi, H. Inokawa, M. Notomi, K. Yamada, T. Tsuchizawa, T. Watanabe, H. Fukuda, H. Shinojima, and S. Itabashi, “Fast all-optical switching using ion-implanted silicon photonic crystal nanocavities,” *Appl. Phys. Lett.*, vol. 90, no. 3, p. 31115, Jan. 2007.

[11] R. L. Espinola, M. C. Tsai, J. T. Yardley, and R. M. Osgood, “Fast and low-power thermooptic switch on thin silicon-on-insulator,” *IEEE Photonics Technol. Lett.*, vol. 15, no. 10, pp. 1366–1368, Oct. 2003.

[12] V. R. Almeida, C. A. Barrios, R. R. Panepucci, and M. Lipson, “All-optical control of light on a silicon chip,” *Nature*, vol. 431, no. 7012, pp. 1081–1084, Oct. 2004.

[13] T. Tanabe, M. Notomi, S. Mitsugi, A. Shinya, and E. Kuramochi, “Fast bistable all-optical switch and memory on a silicon photonic crystal on-chip,” *Opt. Lett.*, vol. 30, no. 19, p. 2575, Oct. 2005.

[14] D. Marris-Morini, L. Vivien, G. Rasigade, J.-M. Fedeli, E. Cassan, X. Le Roux, P. Crozat, S. Maine, A. Lupu, P. Lyan, P. Rivallin, M. Halbwax, and S. Laval, “Recent Progress in High-Speed Silicon-Based Optical Modulators,” *Proc. IEEE*, vol. 97, no. 7, pp. 1199–1215, Jul. 2009.

[15] G. T. Reed and C. E. Jason Png, “Silicon optical modulators,” *Mater. Today*, vol. 8, no. 1, pp. 40–50, 2005.

[16] G. T. Reed, G. Mashanovich, F. Y. Gardes, and D. J. Thomson, “Silicon optical modulators,” *Nat. Photonics*, vol. 4, no. 8, pp. 518–526, Aug. 2010.

[17] T. Yin, R. Cohen, M. M. Morse, G. Sarid, Y. Chetrit, D. Rubin, and M. J. Paniccia, “31 GHz Ge n-i-p waveguide photodetectors on Silicon-on-Insulator substrate,” *Opt. Express*, vol. 15, no. 21, p. 13965, 2007.

[18] M. Casalino, G. Coppola, M. Iodice, I. Rendina, and L. Sirleto, “Near-Infrared Sub-Bandgap All-Silicon Photodetectors: State of the Art and Perspectives,” *Sensors*, vol. 10, no. 12, pp. 10571–10600, Nov. 2010.

[19] X. Wang, Z. Cheng, K. Xu, K. Tsang, and J.-B. Xu, “High-responsivity graphene/silicon-heterostructure waveguide photodetectors,” 2013.

[20] C. Gunn, “CMOS Photonics for High-Speed Interconnects,” *IEEE Micro*, vol. 26, no. 2, pp. 58–66, Mar. 2006.

[21] A. J. Kenyon, “Erbium in silicon,” *Semicond. Sci. Technol.*, vol. 20, no. 12, pp. R65–R84, Dec. 2005.

[22] Z. Fang, Q. Y. Chen, and C. Z. Zhao, “A review of recent progress in lasers on silicon,” *Opt. Laser Technol.*, vol. 46, pp. 103–110, Mar. 2013.

[23] G. T. Reed and A. P. Knights, *Silicon photonics: an introduction*. John Wiley, 2004.

[24] M. A. Green, J. Zhao, A. Wang, P. J. Reece, and M. Gal, “Efficient silicon light-emitting diodes,” *Nature*, vol. 412, no. 23, pp. 805–808, 2001.

[25] V. S.-Y. Lin, K. Motesharei, K.-P. S. Dancil, M. J. Sailor, and M. R. Ghadiri, “A Porous Silicon-Based Optical Interferometric Biosensor,” *Science (80-.).*, vol. 278, no. 5339, 1997.

[26] F. A. Harraz, “Porous silicon chemical sensors and biosensors: A review,” *Sensors Actuators B Chem.*, vol. 202, pp. 897–912, 2014.

[27] C. Pacholski and Claudia, “Photonic Crystal Sensors Based on Porous Silicon,” *Sensors*, vol. 13, no. 4, pp. 4694–4713, Apr. 2013.

[28] Y. Zhao, G. Gaur, S. T. Retterer, P. E. Laibinis, and S. M. Weiss, “Flow-Through Porous Silicon Membranes for Real-Time Label-Free Biosensing,” *Anal. Chem.*, vol. 88, no. 22, pp. 10940–10948, Nov. 2016.

[29] J.-H. Park, L. Gu, G. von Maltzahn, E. Ruoslahti, S. N. Bhatia, and M. J. Sailor, “Biodegradable luminescent porous silicon nanoparticles for in vivo applications,” *Nat. Mater.*, vol. 8, no. 4, pp. 331–336, Apr. 2009.

[30] T. J. Kempa, S.-K. Kim, R. W. Day, H.-G. Park, D. G. Nocera, and C. M. Lieber, “Facet-Selective Growth on Nanowires Yields Multi-Component Nanostructures and Photonic Devices,” *J. Am. Chem. Soc.*, vol. 135, no. 49, pp. 18354–18357, Dec. 2013.

[31] R. Van Laer, B. Kuyken, D. Van Thourhout, and R. Baets, “Interaction between light and highly confined hypersound in a silicon photonic nanowire,” *Nat. Photonics*, vol. 9, no. 3, pp. 199–203, Feb. 2015.

[32] F. Priolo, T. Gregorkiewicz, M. Galli, and T. F. Krauss, “Silicon nanostructures for photonics and photovoltaics,” *Nat. Nanotechnol.*, vol. 9, no. 1, pp. 19–32, Jan. 2014.

[33] K.-Q. Peng, X. Wang, L. Li, Y. Hu, and S.-T. Lee, "Silicon nanowires for advanced energy conversion and storage," *Nano Today*, vol. 8, no. 1, pp. 75–97, 2013.

[34] M. Heiss, Y. Fontana, A. Gustafsson, G. Wüst, C. Magen, D. D. O'Regan, J. W. Luo, B. Ketterer, S. Conesa-Boj, A. V. Kuhlmann, J. Houel, E. Russo-Averchi, J. R. Morante, M. Cantoni, N. Marzari, J. Arbiol, A. Zunger, R. J. Warburton, and A. Fontcuberta i Morral, "Self-assembled quantum dots in a nanowire system for quantum photonics," *Nat. Mater.*, vol. 12, no. 5, pp. 439–444, Feb. 2013.

[35] K. Dohnalová, T. Gregorkiewicz, and K. Kůsová, "Silicon quantum dots: surface matters," *J. Phys. Condens. Matter*, vol. 26, no. 17, p. 173201, Apr. 2014.

[36] A. Y. Liu, C. Zhang, J. Norman, A. Snyder, D. Lubyshev, J. M. Fastenau, A. W. K. Liu, A. C. Gossard, and J. E. Bowers, "High performance continuous wave 1.3 µm quantum dot lasers on silicon," *Appl. Phys. Lett.*, vol. 104, no. 4, p. 41104, Jan. 2014.

[37] Z. H. Zhang, R. Lockwood, J. G. C. Veinot, and A. Meldrum, "Detection of ethanol and water vapor with silicon quantum dots coupled to an optical fiber," *Sensors Actuators B Chem.*, vol. 181, pp. 523–528, 2013.

[38] L. R. Tessler and D. Biggemann, "Optical gain in a-SiNx:H<Nd>," *Opt. Mater. (Amst).*, vol. 27, no. 5, pp. 769–772, 2005.

[39] C. T. M. Ribeiro, M. Siu Li, and a. R. Zanatta, "Spectroscopic study of Nd-doped amorphous SiN films," *J. Appl. Phys.*, vol. 96, no. 2, p. 1068, 2004.

[40] D. Biggemann and L. R. Tessler, "Near infra-red photoluminescence of Nd3+ in hydrogenated amorphous silicon sub-nitrides a-SiNx:H<Nd>," *Mater. Sci. Eng. B*, vol. 105, no. 1–3, pp. 188–191, Dec. 2003.

[41] I. N. Yassievich, M. S. Bresler, O. B. Gusev, P. E. Pak, K. D. Tsendin, and E. I. Terukov, "Mechanism of electroluminescence in the amorphous silicon-based erbium-doped structures," *Mater. Sci. Eng. B*, vol. 81, no. 1–3, pp. 182–184, Apr. 2001.

[42] J. García, M. . Mondragón, O. Maya, and a Campero, "Divalent europium in silica gels," *J. Alloys Compd.*, vol. 275–277, pp. 273–275, Jul. 1998.

[43] D. Li, X. Zhang, L. Jin, and D. Yang, "Structure and luminescence evolution of annealed Europium-doped silicon oxides films.," *Opt. Express*, vol. 18, no. 26, pp. 27191–6, Dec. 2010.

[44] A. M. Dorofeev, N. V. Gaponenko, V. P. Bondarenko, E. E. Bachilo, N. M. Kazuchits, A. A. Leshok, G. N. Troyanova, N. N. Vorosov, V. E. Borisenko, H. Gnaser, W. Bock, P. Becker, and H. Oechsner, "Erbium luminescence in porous silicon doped from spin-on films," *J. Appl. Phys.*, vol. 77, no. 6, p. 2679, 1995.

[45] N. V Gaponenko, V. M. Parkun, O. S. Katernoga, V. E. Borisenko, A. V Mudryi, E. A. Stepanova, A. I. Rat 'ko, M. Cavanagh, B. O 'kelly, and J. F. Mcgilp, "Erbium and terbium photoluminescence in silica sol–gel films on porous alumina," *Thin Solid Films*, vol. 297, pp. 202–206, 1997.

[46] H. A. Lopez and P. M. Fauchet, "Room-temperature electroluminescence from erbium-doped porous silicon," *Appl. Phys. Lett.*, 1999.

[47] H. A. Lopez and P. M. Fauchet, "Erbium emission from porous silicon one-dimensional photonic band gap structures," *http://dx.doi.org/10.1063/1.1331082*, 2000.

[48] J. H. Shin, G. N. van den Hoven, and A. Polman, "Origin of the 1.54 µm luminescence of erbium-implanted porous silicon," *Appl. Phys. Lett.*, vol. 66, no. 18, p. 2379, 1995.

[49] D. Moutonnet, H. L'Haridon, P. N. Favennec, M. Salvi, M. Gauneau, F. Arnaud D'Avitaya, and J. Chroboczek, "1.54 μm photoluminescence of erbium-implanted silicon," *Mater. Sci. Eng. B*, vol. 4, no. 1, pp. 75–77, 1989.

[50] R. A. Babunts, V. A. Vetrov, I. V. Il'in, E. N. Mokhov, N. G. Romanov, V. A. Khramtsov, and P. G. Baranov, "Properties of erbium luminescence in bulk crystals of silicon carbide," *Phys. Solid State*, vol. 42, no. 5, pp. 829–835, May 2000.

[51] M. Markmann, E. Neufeld, A. Sticht, K. Brunner, G. Abstreiter, and C. Buchal, "Enhancement of erbium photoluminescence by substitutional C alloying of Si," *Appl. Phys. Lett.*, 1999.

[52] A. J. Kenyon, P. F. Trwoga, M. Federighi, and C. W. Pitt, "Optical properties of PECVD erbium-doped silicon-rich silica: evidence for energy transfer between silicon microclusters and erbium ions," *J. Phys. Condens. Matter*, vol. 6, no. 21, pp. L319–L324, May 1994.

[53] Y. Gong, M. Makarova, S. Yerci, R. Li, M. Stevens, B. Baek, S. W. Nam, L. Dal Negro, and J. Vuckovic, "Observation of Transparency of Erbium-doped Silicon nitride in photonic crystal nanobeam cavities," *Opt. Express*, vol. 18, no. 13, p. 13863, Jun. 2010.

[54] S. Yerci, R. Li, and L. Dal Negro, "Electroluminescence from Er-doped Si-rich silicon nitride light emitting diodes," *Appl. Phys. Lett.*, vol. 97, no. 8, p. 81109, Aug. 2010.

[55] H.-S. Han, S.-Y. Seo, J. H. Shin, and N. Park, "Coefficient determination related to optical gain in erbium-doped silicon-rich silicon oxide waveguide amplifier," *Appl. Phys. Lett.*, vol. 81, no. 20, pp. 3720–3722, 2002.

[56] H.-S. Han, S.-Y. Seo, and J. H. Shin, "Optical gain at 1.54 μm in erbium-doped silicon nanocluster sensitized waveguide," *Appl. Phys. Lett.*, vol. 79, no. 27, pp. 4568–4570, Dec. 2001.

[57] L. R. Tessler and A. C. Iñiguez, "Optimization of the as-deposited 1.54 μm photoluminescence intensity in a-SiOx:H〈Er〉," *J. Non. Cryst. Solids*, vol. 266, pp. 603–607, 2000.

[58] H. Amekura, A. Eckau, R. Carius, and C. Buchal, "Room-temperature photoluminescence from Tb ions implanted in SiO2 on Si," *J. Appl. Phys.*, vol. 84, no. 7, p. 3867, 1998.

[59] S. Libertino, S. Coffa, R. Mosca, and E. Gombia, "The electrical properties of terbium ions in crystalline Si," *J. Appl. Phys.*, vol. 85, no. 4, p. 2093, 1999.

[60] B. Kaleli, M. Kulakci, and R. Turan, "Mechanisms of light emission from terbium ions (Tb3+) embedded in a Si rich silicon oxide matrix," *Opt. Mater. (Amst).*, vol. 34, no. 11, pp. 1935–1939, Sep. 2012.

[61] H. Jeong, S. Y. Seo, and J. H. Shin, "Excitation mechanism of visible, Tb3+ photoluminescence from Tb-doped silicon oxynitride," *Appl. Phys. Lett.*, vol. 88, no. 16, pp. 19–22, 2006.

[62] A. Podhorodecki, G. Zatryb, J. Misiewicz, J. Wojcik, P. R. J. Wilson, and P. Mascher, "Green light emission from terbium doped silicon rich silicon oxide films obtained by plasma enhanced chemical vapor deposition.," *Nanotechnology*, vol. 23, no. 47, p. 475707, Nov. 2012.

[63] M. M. Klak, G. Zatryb, J. Wojcik, J. Misiewicz, P. Mascher, and A. Podhorodecki,

"Mechanism of enhanced photoluminescence of Tb ions in hydrogenated silicon-rich silicon oxide films," *Thin Solid Films*, vol. 611, pp. 62–67, 2016.

[64] B. Swatowska and T. Stapinski, "Amorphous hydrogenated silicon-nitride films for applications in solar cells," *Vacuum*, vol. 82, no. 10, pp. 942–946, Jun. 2008.

[65] S. V. Deshpande, E. Gulari, S. W. Brown, and S. C. Rand, "Optical properties of silicon nitride films deposited by hot filament chemical vapor deposition," *J. Appl. Phys.*, vol. 77, no. 12, pp. 6534–6541, 1995.

[66] F. Demichelis, G. Crovini, F. Giorgis, C. F. Pirri, and E. Tresso, "Hydrogenated amorphous silicon-nitrogen alloys, a-SiNx:Hy: a wide band gap material for optoelectronic devices," *J. Appl. Phys.*, vol. 79, no. 3, p. 1730, 1996.

[67] K.-H. Han, M.-B. Park, and N.-H. Cho, "Effect of Tb-doping on the nano-structural and optical features of nano-crystalline Si thin films," *Surf. Sci.*, vol. 514, no. 1–3, pp. 117–122, Aug. 2002.

[68] S.-Y. Seo and J. H. Shin, "Enhancement of the green, visible Tb[sup 3+] luminescence from Tb-doped silicon-rich silicon oxide by C co-doping," *Appl. Phys. Lett.*, vol. 84, no. 22, p. 4379, 2004.

[69] M.-B. Park, K.-H. Han, J.-H. Shim, C. Namgung, and N.-H. Cho, "Effect of rare earth ions-doping on the chemical and optical features of nano-crystalline (Er, Tb:) Si thin films," *Appl. Surf. Sci.*, vol. 234, no. 1–4, pp. 78–81, Jul. 2004.

[70] J. M. Sun, W. Skorupa, T. Dekorsy, and M. Helm, "Bright green electroluminescence from Tb3+ in silicon metal-oxide-semiconductor devices," *J. Appl. Phys.*, vol. 97, p. 123513, 2005.

[71] A. Podhorodecki, L. W. Golacki, G. Zatryb, J. Misiewicz, J. Wang, W. Jadwisienczak, K. Fedus, J. Wojcik, P. R. J. Wilson, and P. Mascher, "Excitation mechanism and thermal emission quenching of Tb ions in silicon rich silicon oxide thin films grown by plasma-enhanced chemical vapour deposition—Do we need silicon nanoclusters?," *J. Appl. Phys.*, vol. 115, no. 14, p. 143510, Apr. 2014.

[72] W. Fuhs, "Excitation and temperature quenching of Er-induced luminescence in a-Si:H(Er)," *Phys. Rev. B*, vol. 56, no. 15, pp. 9545–9551, 1997.

[73] Z. Z. Yuan, D. S. Li, M. H. Wang, P. L. Chen, D. Gong, L. Wang, and D. Yang, "Photoluminescence of Tb3+ doped SiNx films grown by plasma-enhanced chemical vapor deposition," *J. Appl. Phys.*, vol. 100, p. 83106, 2006.

[74] J. Robertson, "Electronic structure of silicon nitride," *Philos. Mag. B*, vol. 63, no. 1, pp. 47–77, 1990.

[75] J. M. Sun, W. Skorupa, T. Dekorsy, M. Helm, L. Rebohle, and T. Gebel, "Bright green electroluminescence from Tb[sup 3+] in silicon metal-oxide-semiconductor devices," *J. Appl. Phys.*, vol. 97, no. 12, p. 123513, 2005.

[76] L. R. Tessler and D. Biggemann, "Temperature independent Er3+ photoluminescence lifetime in a-Si:H<Er> and a-SiOx:H<Er>," *Mater. Sci. Eng. B*, vol. 105, no. 1–3, pp. 165–168, Dec. 2003.

[77] D. Biggemann, D. Mustafa, and L. R. Tessler, "Photoluminescence of Er-doped silicon nanoparticles from sputtered SiO x thin films," *Opt. Mater. (Amst).*, vol. 28, pp. 842–845, 2006.

[78] D. L. Smith, *Thin-film deposition: principles and practice*, Internatio. Singapore:

McGraw-Hill, 1997.

[79] J. C. G. Bünzli and S. V. Eliseeva, “Basics of Lanthanide Photophysics,” in *Lanthanide Luminescence: Photophysical, Analytical and Biological Aspects*, P. Hänninen and H. Härmä, Eds. Springer, 2011, pp. 1–46.

[80] G. H. Dieke, *Spectra and Energy Levels of Rare Earth Ions in Crystals*, Crosswhite. John Wiley & Sons, 1968.

[81] D. J. Newman and B. Ng, *Crystal Field Handbook*, 1st ed. New York: Cambridge University Press, 2007.

[82] G. Liu, “Electronic Energy Level Structure,” in *Spectroscopic Properties of Rare Earths in Optical Materials*, G. Liu and B. Jacquier, Eds. New York: Springer, 1999, pp. 1–94.

[83] R. Eisberg and R. Resnick, *Quantum Physics of Atoms, Molecules, Solids, Nuclei, and Particles*, 2 edition. Wiley, 1985.

[84] J. C. Slater, *Quantum Theory of Atomic Structure*. New York: McGraw-Hill, 1960.

[85] O. Madelung, *Introduction to solid-state theory*. Springer Series in Solid-State Sciences, 1978.

[86] P. A. Tanner, “Lanthanide Luminescence in Solids,” in *Lanthanide Luminescence: Photophysical, Analytical and Biological Aspects*, P. Hänninen and H. Härmä, Eds. Berlin Heidelberg: Springer-Verlag, 2010, pp. 183–233.

[87] G. H. Dieke, “Spectra and Energy Levels of Rare Earth Ions in Crystals,” *Am. J. Phys.*, vol. 38, no. 3, p. 399, 1970.

[88] L. G. DeShazer and G. H. Dieke, “Spectra and Energy Levels of Eu3+ in LaCl3,” *J. Chem. Phys.*, vol. 38, no. 9, pp. 2190–2199, Nov. 1963.

[89] K. A. Görller-Walrand and K. Binnemans, “Rationalization of Crystal-Field Parametrization,” in *Handbook of Physical Chemistry of Rare Earths, Vol. 23*, K. A. Gschneidner and L. Eyring, Eds. Amsterdam: Elsevier, 1996.

[90] O. L. Malta and L. D. Carlos, “Intensities of 4f-4f transitions in glass materials,” *Quim. Nova*, vol. 26, no. 6, pp. 889–895, 2003.

[91] J. J. Sakurai, *Modern Quantum Mechanics*, Revised. Addison-Wesley Publishing Company, 1994.

[92] G. S. Ofelt, “Structure of the f6 Configuration with Application to Rare-Earth Ions,” *J. Chem. Phys.*, vol. 38, no. 9, p. 2171, 1963.

[93] B. R. Judd, “Optical Absorption Intensities of Rare-Earths Ions,” *Phys. Rev.*, vol. 127, no. 3, pp. 750–761, 1962.

[94] L. Smentek, “Judd—Ofelt theory: past, present and future,” *Mol. Phys.*, vol. 101, pp. 893–897, 2003.

[95] P. Goldner, “Accuracy of the Judd-Ofelt Theory,” *Mol. Phys.*, vol. 101, no. July 2012, pp. 903–908, 2003.

[96] M. F. Reid, “Matrix Elements of Tensor Operators,” in *Spectroscopic Properties of Rare Earths in Optical Materials*, Springer, 1999, pp. 537–540.

[97] P. F. Moulton, “Spectroscopic and laser characteristics of Ti:Al2O3,” *J. Opt. Soc. Am. B*, vol. 3, no. 1, p. 125, Jan. 1986.

[98] M. E. Weeks, “The discovery of the elements. XVI. The rare earth elements,” *J. Chem. Educ.*, vol. 9, no. 10, p. 1751, Oct. 1932.

[99] A. M. Srivastava and C. R. Ronda, “Phosphors,” *Electrochem. Soc. Interface*, pp. 48–51, 2003.

[100] H. Ronda, C. R., Jüstel, T, Nikol, “Rare earth phosphors: fundamentals and applications,” *J. Alloys Compd.*, vol. 275–277, pp. 669–676, 1998.

[101] C. Cohen-Tannoudji and B. Diu, *Quantum Mechanics*. Paris: John Wiley & Sons, 1977.

[102] W. Kutzelnigg and J. D. Morgan III, “Hund’s rules,” *Zeitschrift für Phys. D Atoms, Mol. Clust.*, vol. 36, no. 3–4, pp. 197–214, 1996.

[103] D. C. De Mello, A. Meijerink, and G. Blasse, “Non-radiative Relaxation Processes of the Pr3+ Ion in Solids,” *J. Phys. Chem. Solids*, vol. 56, pp. 673–685, 1995.

[104] B. Henderson and G. F. Imbusch, *Optical Spectroscopy of Inorganic Solids*. Oxford: Clarendon Press, 1989.

[105] P. R. J. Wilson, “Study of Luminescent Silicon-Rich Silicon Nitride and Cerium and Terbium Doped Silicon Oxide Thin Films,” McMaster University, 2013.

[106] S. Chandrasekhar, “Stochastic problems in physics and astronomy,” *Reviews of Modern Physics*, vol. 15, no. 1. pp. 1–89, 1943.

[107] F. Benz, J. A. Guerra, Y. Weng, a. R. Zanatta, R. Weingärtner, and H. P. Strunk, “Concentration quenching of the green photoluminescence from terbium ions embedded in AlN and SiC matrices,” *J. Lumin.*, vol. 137, pp. 73–76, May 2013.

[108] R. A. Street, “Growth and structure of amorphous silicon,” in *Hydrogenated Amorphous Silicon*, 1991, pp. 18–61.

[109] R. A. Street, *Hydrogenated Amorphous Silicon*, 1st ed. New York: Cambridge University Press, 1991.

[110] J. Singh and K. Shimakawa, *Advances in amorphous semiconductors*. Taylor & Francis, 2003.

[111] K. Morigaki, *Physics of amorphous Semiconductors*. London: World Scientific Pub Co Inc, 1999.

[112] M. F. Thorpe and D. Weaire, “Electronic Properties of an Amorphous Solid. II. Further Aspects of the Theory,” *Phys. Rev. B*, vol. 4, no. 10, pp. 3518–3527, 1971.

[113] N. F. Mott and E. A. Davis, *Electronic Processes in Non-Crystalline Materials*, 2nd ed. New York: Oxford University Press, 1979.

[114] W. L. Warren, J. Robertson, and J. Kanicki, “Si and N dangling bond creation in silicon nitride thin films,” *Appl. Phys. Lett.*, vol. 63, no. 19, pp. 2685–2687, 1993.

[115] F. Urbach, “The Long-Wavelength Edge of Photographic Sensitivity and of the Electronic Absorption of Solids,” *Phys. Rev.*, vol. 92, p. 1324, 1953.

[116] L. R. Tessler and I. Solomon, “Photoluminescence of tetrahedrally coordinated a-Si(1-x)C(x):H,” *Phys. Rev. B*, vol. 52, no. 15, pp. 962–971, 1995.

[117] R. A. Street, “Phonon interactions in the luminescence of amorphous silicon,” *Philos. Mag. Part B*, vol. 37, no. 1, pp. 35–42, Jan. 1978.

[118] J. Shah, A. Pinczuk, F. B. Alexander, B. G. Bagiey, and A. G. Chynoweth, “Excitation

wavelength dependence of luminescence spectra of a-Si:H," *Solid State Commun.*, vol. 42, no. 10, pp. 717–720, 1982.

[119] R. A. Street, "Luminescence and recombination in hydrogenated amorphous silicon," *Adv. Phys.*, vol. 30, no. 5, pp. 593–676, Oct. 1981.

[120] F. Boulitrop and D. J. Dunstan, "Phonon interactions in the tail states," *Phys. Rev. B*, vol. 28, no. 10, pp. 5923–5929, 1983.

[121] D. J. Dunstan and F. Boulitrop, "Photoluminescence in hydrogenated amorphous silicon," *Phys. Rev. B*, vol. 30, no. 10, pp. 5945–5957, 1984.

[122] T. M. Searle and W. A. Jackson, "Static versus electron-phonon disorder in amorphous Si:H and its alloys," *Philos. Mag. B*, vol. 60, no. 2, pp. 237–255, 1989.

[123] W. L. Warren, J. Kanicki, J. Robertson, and P. M. Lenahan, "Energy level of the nitrogen dangling bond in amorphous silicon nitride," *Appl. Phys. Lett.*, vol. 59, no. 14, pp. 1699–1701, 1991.

[124] J. Robertson and M. J. Powell, "Gap states in silicon nitride," *Appl. Phys. Lett.*, vol. 44, no. 4, pp. 415–417, 1984.

[125] J. Robertson, "Defects and hydrogen in amorphous silicon nitride," *Philosophical Magazine Part B*, vol. 69, no. 2. pp. 307–326, 1994.

[126] K. Jarolimek, R. A. De Groot, G. A. De Wijs, and M. Zeman, "Atomistic models of hydrogenated amorphous silicon nitride from first principles," *Phys. Rev. B - Condens. Matter Mater. Phys.*, vol. 82, no. 20, pp. 1–9, 2010.

[127] F. Giorgis, C. F. Pirri, and E. Tresso, "Structural properties of a-Si1- xNx : H films grown by plasma enhanced chemical vapour deposition by SiH4 + NH 3 + H 2 gas mixtures," *Thin Solid Films*, vol. 307, pp. 298–305, 1997.

[128] J. Kistner, X. Chen, Y. Weng, H. P. Strunk, M. B. Schubert, and J. H. Werner, "Photoluminescence from silicon nitride-no quantum effect," *J. Appl. Phys.*, vol. 110, no. 2, 2011.

[129] K. Oura, M. Katayama, A. V. Zotov, V. G. Lifshits, and A. A. Saranin, *Surface Science*. Berlin, Heidelberg: Springer Berlin Heidelberg, 2003.

[130] W. K. Chu, J. W. Mayer, and M. A. Nicolet, *Backscattering Spectrometry*. New York: Academic Press, 1978.

[131] M. Mayer, "Rutherford Backscattering Spectrometry (RBS)," *Lectures given at the Workshop on Nuclear Data for Science and Technology: Materials Analysis Trieste, 19-30 May 2003*, no. May. Trieste, 2003.

[132] M. H. Tabacniks, "Análise de filmes finos por PIXE e RBS." São Paulo.

[133] M. Mayer, "SIMNRA User's Guide," Garching, Germany, 6.05, 1997.

[134] B. Gault, M. P. Moddy, J. M. Cairney, and S. P. Ringer, *Atom Probe Microscopy*. Springer, 2012.

[135] P. Bas, A. Bostel, B. Deconihout, and D. Blavette, "P.," *Appl. Surf. Sci.*, vol. 87–88, pp. 298–304, 1995.

[136] Grant Bunker, *Introduction to XAFS: A Practical Guide to X-ray Absorption Fine Structure Spectroscopy*. Cambridge University Press, 2010.

[137] B. K. Teo, "Extended X-ray Absorption Fine Structure (EXAFS) Spectroscopy," in

EXAFS: Basic Principles and Data Analysis, Springer Berlin Heidelberg, 1986, pp. 21–33.

[138] V. L. Aksenov, A. Y. Kuzmin, J. Purans, and S. I. Tyutyunnikov, “V. L. Aksenov, A. Yu. Kuzmin, J. Purans, S. I. Tyutyunnikov, Physics of Particles and Nuclei 32, 1-33 (2001),” *Phys. Part. Nucl.*, vol. 32, pp. 1–33, 2001.

[139] D. C. Koningsberger and R. Prins, Eds., “Xray Absorption: Principles, Applications, Techniques of EXAFS, SEXAFS, and XANES,” in *Chemical Analysis 92*, John Wiley & Sons, 1988.

[140] M. Newville, “Fundamentals of XAFS.” 2004.

[141] W. a. Lanford and M. J. Rand, “The hydrogen content of plasma-deposited silicon nitride,” *J. Appl. Phys.*, vol. 49, no. 4, pp. 2473–2477, 1978.

[142] M. Fox, *Optical Properties of Solids*. Oxford: Oxford University Press, 2001.

[143] R. A. Street, *Hydrogenated Amorphous Silicon*. New York: Cambridge University Press, 1991.

[144] D. L. Smith, “Energy Beams,” in *Thin-film deposition: principles and practice*, Internatio., Singapore: McGraw-Hill, 1997, pp. 371–452.

[145] D. C. B. Tejero, “Neodímio em Sub-Nitretos de Silício Amorfo Hidrogenado (a-SiNx:H),” University of Campinas, 2005.

[146] W. A. P. Claassen, “Characterization of Plasma Silicon Nitride Layers,” *J. Electrochem. Soc.*, vol. 130, no. 12, p. 2419, 1983.

[147] G. Xu, P. Jin, M. Tazawa, and K. Yoshimura, “Optical investigation of silicon nitride thin films deposited by r.f. magnetron sputtering,” *Thin Solid Films*, vol. 425, no. 1–2, pp. 196–202, Feb. 2003.

[148] M. A. Signore, A. Sytchkova, D. Dimaio, A. Cappello, and A. Rizzo, “Deposition of silicon nitride thin films by RF magnetron sputtering: a material and growth process study,” *Opt. Mater. (Amst).*, vol. 34, no. 4, pp. 632–638, 2012.

[149] R. Dabkowski, “Installation of a new electron cyclotron plasma enhanced chemical vapour deposition (ECR-PECVD) reactor and a preliminary study of thin film depositions,” McMaster University, 2012.

[150] J. Li, O. H. Y. Zalloum, T. Roschuk, C. L. Heng, J. Wojcik, and P. Mascher, “Light emission from rare-earth doped silicon nanostructures,” *Adv. Opt. Technol.*, pp. 1–10, 2008.

[151] M. Boudreau, M. Boumerzoug, R. V. Kruzelecky, P. Mascher, P. E. Jessop, and D. A. Thompson, “Electron-cyclotron-resonance CVD of silicon oxynitride for optoelectronic applications,” in *Materials Research Society Proceeding*, 1993, pp. 183–188.

[152] S. E. Alexandrov, M. L. Hitchman, and A. Y. Kovalgin, “Remote Plasma-enhanced CVD of Silicon Nitride Films : Effects of Diluting Nitrogen with Argon . Part I : Effect on Nitrogen Plasma Parameters Studied by Emission Spectroscopy,” *Adv. Mater. Opt. Electron.*, vol. 8, no. September 1997, pp. 23–29, 1998.

[153] G. Bambakidis and R. C. Bowman, Eds., *Hydrogen in Disordered and Amorphous Solids*, 1986th ed., vol. 136. Boston, MA: Springer US, 1986.

[154] C. Piamonteze, A. C. Iñiguez, L. R. Tessler, M. C. Martins Alves, and H. Tolentino,

"Environment of Erbium in a−Si:H and a−SiOx:H," *Phys. Rev. Lett.*, vol. 81, no. 21, pp. 4652–4655, Nov. 1998.

[155] L. J. Terminello and C. . Symposium on Applications of Synchrotron Radiation Techniques to Materials Science (1996 : San Francisco, *Applications of synchrotron radiation techniques to materials science III : symposium held April 8-12, 1996, San Francisco, California, U.S.A.* Materials Research Society, 1996.

[156] L. R. Tessler, C. Piamonteze, M. C. Martins Alves, and H. Tolentino, "Evolution of the Er environment in a-Si:H under annealing: ion implantation versus co-deposition," *J. Non. Cryst. Solids*, vol. 266, pp. 598–602, 2000.

[157] G. F. Bosco and L. R. Tessler, "Tb3+ Luminescence in a-SiNx:H," *ECS Trans.*, vol. 61, no. 5, pp. 141–146, Mar. 2014.

[158] T. Roschuk, P. R. J. Wilson, J. Li, J. Wojcik, and P. Mascher, "X-ray spectroscopy studies of luminescent Si-based materials," in *2008 5th IEEE International Conference on Group IV Photonics*, 2008, pp. 288–290.

[159] P. R. Wilson, T. Roschuk, K. Dunn, E. N. Normand, E. Chelomentsev, O. H. Zalloum, J. Wojcik, and P. Mascher, "Effect of thermal treatment on the growth, structure and luminescence of nitride-passivated silicon nanoclusters.," *Nanoscale Res. Lett.*, vol. 6, no. 1, p. 168, Jan. 2011.

[160] J. Li, O. Zalloum, T. Roschuk, C. Heng, J. Wojcik, and P. Mascher, "The formation of light emitting cerium silicates in cerium-doped silicon oxides," *Appl. Phys. Lett.*, vol. 94, no. 1, p. 11112, 2009.

[161] J. Wang, H. Song, X. Kong, W. Xu, and H. Xia, "Temperature dependence of the fluorescence of Eu[sup 3+]-ion doped in various silicate glasses," *J. Appl. Phys.*, vol. 91, no. 12, p. 9466, 2002.

[162] a. Rodriguez-Gómez, a. García-Valenzuela, E. Haro-Poniatowski, and J. C. Alonso-Huitrón, "Effect of thickness on the photoluminescence of silicon quantum dots embedded in silicon nitride films," *J. Appl. Phys.*, vol. 113, no. 23, p. 233102, 2013.

Appendix I – Deposition conditions used for reactive RF-Sputtering grown samples

Table V: Parameters kept constant for all depositions of this work.

Base Pressure [mTorr]	$< 2.2\mathrm{x}10^{-3}$
Total Pressure [mTorr]	6.0
Stage T [ºC]	250
Bias [V]	-1000
Dep. Time [min]	120

Table VI: Deposition conditions of all the films produced by Sputtering. Rel. Area refers to the percentage of the Si target area covered by Tb_4O_7 powder pellets.

Sample ID	**Rel. Area**	**P_{N2}**	**H_2**	**Sample ID**	**Rel. Area**	**P_{N2}**	**H_2**
	%	**mtorr**	**sccm**		**%**	**mtorr**	**sccm**
1	1.8	1.50	2.3	**18**	6.4	4.50	2.3
2	1.8	1.50	8.0	**19**	6.4	1.50	4.0
3	1.8	0.60	2.3	**20**	6.4	1.50	0.0
4	1.8	0.60	8.0	**21**	6.4	1.50	8.0
5	1.8	0.75	2.3	**22**	6.4	1.50	3.0
6	1.8	0.75	8.0	**23**	6.4	1.50	6.0
7	6.7	1.50	2.3	**24**	7.0	0.68	2.3
8	6.7	1.50	8.0	**25**	7.0	2.25	2.3
9	6.7	0.60	2.3	**26**	7.0	0.75	2.3
10	6.7	0.60	8.0	**27**	7.0	1.50	2.3
11	6.7	0.75	2.3	**28**	7.0	6.00	2.3
12	6.7	0.75	8.0	**29**	7.0	2.85	2.3
13	1.1	0.75	2.3	**30**	17.5	1.50	6.0
14	1.1	0.75	8.0	**31**	11.0	1.50	6.0
15	1.1	1.50	2.3	**32**	5.0	1.50	6.0
16	1.1	1.50	8.0	**33**	5.5	1.50	6.0
17	6.4	3.38	2.3	**34**	3.5	1.50	6.0

Appendix II ─ Deposition conditions used for ECR PECVD grown samples

Table VII: Deposition parameters kept constant for the first set of ECR PECVD grown films. The Ar flux in the Tb row refers to the Ar line that carries the sublimated Tb precursor from the heater cells.

Base Pressure [mtorr]		< 4.0 x 10^{-4}
Stage T [ºC]		350
Plasma Power [W]	**Power**	500-510
	Reflected	0-10
SiH_4 flux	**[sccm]**	2.5
	[mtorr]	0.3
Tb Cell	**[sccm]**	5.0
	[mtorr]	0.6

Table VIII: Deposition conditions used for the first series of ECR PECVD grown samples. The first runs refer to calibration samples where there is no terbium incorporation. The subsequent depositions were planned to vary the samples' optical gap through variation in N_2.

Sample ID	**N_2**		**N_2/Ar (10%)**		**Ar**		**Tb**	**Total Pressure**
	sccm	**mtorr**	**sccm**	**mtorr**	**sccm**	**mtorr**	**ºC**	**mtorr**
1	15	1.5	**0.0**	0.0	**20**	3.6	0	3.7
2	20	2.0	**0.0**	0.0	**15**	3.6	0	3.7
3	25	2.4	**0.0**	0.0	**10**	3.6	0	3.7
4	10	1.0	**0.0**	0.0	**25**	3.6	0	3.7
5	10	1.0	**0.0**	0.0	**25**	3.6	190	4.3
6	20	2.2	**0.0**	0.0	**15**	3.7	190	4.4
7	20	2.1	**0.0**	0.0	**15**	3.6	190	4.3
8	5	0.5	**0.0**	0.0	**30**	3.7	190	3.8
9	5	0.5	**0.0**	0.0	**30**	3.7	0	3.8
10	20	2.1	**0.0**	0.0	**15**	3.6	170	4.3
11	20	2.1	**0.0**	0.0	**15**	3.6	150	4.3
12	15	1.5	**0.0**	0.0	**20**	3.6	0	3.7
13	10	1.1	**0.0**	0.0	**25**	3.7	190	4.3
14	20	2.0	**0.0**	0.0	**15**	3.6	210	4.3
15	0.0	0.0	**20.0**	2.1	**14**	3.6	190	4.1
16	20	2.1	**0.0**	0.0	**15**	3.7	220	4.3
17	15	1.6	**0.0**	0.0	**20**	3.7	190	4.3
18	25	2.5	**0.0**	0.0	**10**	3.6	190	4.2
19	20	2.1	**0.0**	0.0	**15**	3.7	190	4.3
20	30	2.9	**0.0**	0.0	**5**	3.7	190	4.1
21	27	2.6	**0.0**	0.0	**8**	3.5	190	4.1
22	23	2.4	**0.0**	0.0	**12**	3.7	190	4.2
24	25	2.5	**0.0**	0.0	**10**	3.6	190	4.2

Table IX: Deposition parameters kept constant of the second set of ECR PECVD grown films. The Tb heater cell temperature was kept constant at 190ºC.

Base Pressure [mtorr]		$< 4.0 \times 10^{-4}$
Stage T [ºC]		350
Plasma Power [W]	**Power**	500-510
	Reflected	0-10
SiH_4 flux	**[sccm]**	2.5
	[mtorr]	0.3
Tb Cell	**[ºC]**	190
	[sccm]	5.0
	[mtorr[	0.6

Table X: Deposition conditions used of the second series of ECR PECVD grown samples. The goal was to explore the relationship of Tb incorporation and lower the bandgap with SiH_4 flow.

Sample ID	**N_2**		**N_2/Ar (10%)**		**SiH_4**		**Ar**		**Total Pressure**
	sccm	**mtorr**	**sccm**	**mtorr**	**sccm**	**mtorr**	**sccm**	**mtorr**	**mtorr**
39	8.0	0.9	0.0	0.0	1.0	2.0	5.0	1.5	2.0
40	8.0	0.9	0.0	0.0	1.0	1.4	0.0	0.0	1.4
41	8.0	0.9	0.0	0.0	2.0	1.5	0.0	0.0	1.5
42	8.0	0.9	0.0	0.0	3.0	1.6	0.0	0.0	1.6
43	8.0	0.9	0.0	0.0	4.0	1.6	0.0	0.0	1.6
44	8.0	0.9	0.0	0.0	0.6	1.4	0.0	0.0	1.4
45	8.0	0.9	0.0	0.0	5.0	1.7	0.0	0.0	1.7
46	8.0	0.9	0.0	0.0	4.0	1.6	0.0	0.0	1.6
47	5.0	0.6	0.0	0.0	3.0	1.2	0.0	0.0	1.2
48	0.0	0.0	40	4.1	3.0	4.5	0.0	0.0	4.5
49	0.0	0.0	20	2.1	3.0	2.7	0.0	0.0	2.7
50	0.0	0.0	50	5	3.0	5.45	0.0	0.0	5.5
51	15	1.5	0.0	0.0	3.0	2.2	0.0	0.0	2.2
52	8.0	0.9	0.0	0.0	7.0	1.8	0.0	0.0	1.8
53	0.0	0.0	40	4.1	5.0	4.7	0.0	0.0	4.7
54	0.0	0.0	40	4.1	7.0	4.8	0.0	0.0	4.8
55	15	1.6	0.0	0.0	7.0	2.4	0.0	0.0	2.4
56	0.0	0.0	40	4.1	4.0	4.6	0.0	0.0	4.6
57	5.0	0.6	0.0	0.0	4.0	1.3	0.0	0.0	1.3
58	15	1.5	0.0	0.0	4.0	2.2	0.0	0.0	2.2
59	0.0	0.0	20	2.1	4.0	2.7	0.0	0.0	2.7
60	8.0	0.9	0.0	0.0	8.0	1.9	0.0	0.0	1.9
61	8.0	0.9	0.0	0.0	10	2.0	0.0	0.0	2.0
62	8.0	0.9	0.0	0.0	14	2.3	0.0	0.0	2.3
63	8.0	0.9	0.0	0.0	7.0	1.8	0.0	0.0	1.8
69	20	2.1	0.0	0.0	7.0	2.9	0.0	0.0	2.9
70	8.0	0.9	0.0	0.0	7.0	1.8	0.0	0.0	1.8
74	4.0	0.4	0.0	0.0	7.0	1.8	4.0	1.0	1.8
75	8.0	0.9	0.0	0.0	6.0	1.7	0.0	0.0	1.7
76	6.0	0.4	0.0	0.0	7.0	2.5	10	1.7	2.5